EFFECTS OF GAS DIFFUSION LAYER COMPRESSION ON ELECTROMECHANICAL PROPERTIES AND POLYMER ELECTROLYTE FUEL CELL PERFORMANCE

Thesis
Submitted in partial fulfilment of the requirement for the degree of

DOCTOR OF PHILOSOPHY

by

UMESH SHINDE

(Reg. No. 187026ME016)

DEPARTMENT OF MECHANICAL ENGINEERING

NATIONAL INSTITUTE OF TECHNOLOGY KARNATAKA

SURATHKAL, MANGALORE – 575025

APRIL, 2023

EFFECTS OF GAS DIFFUSION LAYER COMPRESSION ON ELECTROMECHANICAL PROPERTIES AND POLYMER ELECTROLYTE FUEL CELL PERFORMANCE

Thesis
Submitted in partial fulfilment of the requirement for the degree of

DOCTOR OF PHILOSOPHY

by

UMESH SHINDE

(Reg. No. 187026ME016)

Under the guidance of

Dr. POORNESH KUMAR KOORATA

Assistant Professor

DEPARTMENT OF MECHANICAL ENGINEERING

NATIONAL INSTITUTE OF TECHNOLOGY KARNATAKA

SURATHKAL, MANGALORE – 575025

APRIL, 2023

DECLARATION

I hereby declare that the Research Thesis entitled **"EFFECTS OF GAS DIFFUSION LAYER COMPRESSION ON ELECTROMECHANICAL PROPERTIES AND POLYMER ELECTROLYTE FUEL CELL PERFORMANCE"** which is being submitted to the **National Institute of Technology Karnataka, Surathkal** in partial fulfillment of the requirements for the award of the degree of **Doctor of Philosophy in Mechanical Engineering** is a *bonafide report of the research work carried out by me*. The material contained in this Research Theis has not been submitted to any University or Institution for the award of any degree.

Register Number: **187026ME016**
Name of the Research Scholar: **UMESH SHINDE**
Signature of the Research Scholar:

Department of Mechanical Engineering

Place: NITK, Surathkal

Date: 21/04/2023

CERTIFICATE

This is to certify that the Research Thesis entitled **"EFFECTS OF GAS DIFFUSION LAYER COMPRESSION ON ELECTROMECHANICAL PROPERTIES AND POLYMER ELECTROLYTE FUEL CELL PERFORMANCE"** submitted by **Mr. UMESH SHINDE (Register Number: 187026ME016)** as the record of the research work carried out by him, *is accepted as the Research Thesis submission* in partial fulfilment of the requirements for the award of the degree of **Doctor of Philosophy**.

Research Guide

Dr. Poornesh Kumar Koorata
Assistant Professor
Department of Mechanical Engineering

Chairman-DRPC 25.4 2023
Department of Mechanical Engineering
National Institute of Technology Karnataka
Surathkal, Mangalore - 575025

ACKNOWLEDGEMENT

It brings me great pleasure to thank everyone who has assisted, motivated, and supported me throughout my Ph.D journey at NITK Surathkal. First and foremost, I would like to express my heartfelt gratitude to my mentor, **Dr. Poornesh Kumar Koorata**, Assistant Professor, Mechanical Engineering Department, National Institute of Technology Karnataka, Surathkal, Mangalore, for his support and advice that have motivated and guided me in the right path.

I am immensely grateful to our director, **Prof. Prasad Krishna**, for instilling in students a desire to conduct research. I like to thank **Prof. Ravikiran Kadoli**, Professor and Head of the Department, Department of Mechanical Engineering, National Institute of Technology Karnataka, Surathkal, Mangalore, for his cooperation in providing the necessary facilities. I would also like to thank RPAC members **Dr. Subhaschandra Kattimani**, Associate Professor, Department of Mechanical Engineering and **Dr. Hari Prasad Dasari**, Associate Professor, Department of Chemical Engineering, as well as DRPC secretary, **Dr. Vasudeva Madav,** Assistant Professor, Department of Mechanical Engineering, National Institute of Technology, Karnataka, Surathkal for their insightful comments and extending support in completing this work.

I would like to express my deepest gratitude to my parents, **Ramappa Shinde** and **Anusuya Shinde**, who always supported me in my endeavours. Their confidence in my ability to succeed was the impetus I needed to move forward and confront obstacles. I am grateful to my younger brother **Mahesh Shinde** for taking care of parents during my stay at NITK.

Throughout my Ph.D studies, I am indebted to **Vaishakh R, Vikas Kumar, Sachin Kumar V,** and **Pranav P,** my research group members of Electrochemical Energy System Design Laboratory and Applied Solid Mechanics Laboratory, for their continuous support.

Without friends, life would not have been as exciting and intriguing. I want to thank my dearest friends **Vinayak K**, **Vishwanath B**, **Arun Kumar DS**, and **Suhas A**, who were always there for me during my Ph.D work.

I thank God for showering me with blessings and gifting me with such lovely family and friends.

UMESH SHINDE

ABSTRACT

The Gas diffusion layer (GDL) is an essential functional component of the Polymer electrolyte fuel cells (PEFC) as it enables the efficient transport of reactants and offers mechanical stability. The influence of compressive loads on the performance of GDL has been the subject of extensive research. In this thesis, a numerical method is explored to investigate interface properties in the bipolar plate (BPP)|GDL and GDL|Polymer electrolyte membrane (PEM) under material and geometrical heterogeneities. Observations indicate that the results are sensitive to GDL material models and endplate designs. This implies that endplates designed to improve the electrical contact resistance and contact pressure at the BPP|GDL interface may not necessarily guarantee an improvement in bulk properties due to a localised, nonintuitive relationship between the electrical interface contact resistance (ICR) and bulk properties. The combined influence of non-uniform ICR and inlet relative humidity (RH), on a single flow channel, along with the heterogeneous flow properties of the GDL, is considered for the PEFC performance evaluation. The results indicate that heterogeneous GDL with non-uniform ICR distribution leads to a ~4.4% decrease in current density at 0.3V compared to homogeneous GDL under full humidification. However, the current density increases by ~19% under fully humidified anode and a partially humidified cathode. Furthermore, the GDL heterogeneity caused by the two clamping designs is simulated to predict the transport characteristics and performance of a 25cm^2 active area PEFC. Compared to the conventional endplate design, the proposed endplate configuration offers increased cell performance, which may result from the uniform GDL properties. In addition, the experimental cyclic response of commercially available GDLs with/without MPL (microporous layer) is envisioned for mechanical response at various temperatures and hotpress conditions. The GDL with MPL has a substantial strain response with low force resistance, but GDL w/o MPL has a higher stress-to-strain ratio. The significance of pre- and post-hotpress conditions demonstrated that mechanical response increased by more than 120% in post-hotpress conditions. The thesis concludes with a newly developed phenomenological material model to predict cyclic electrical conductivity in GDLs.

Keywords: *Polymer electrolyte fuel cell, Gas diffusion layer, Mechanical properties, electrical properties, Relative humidity, Cell performance*

TABLE OF CONTENTS

LIST OF FIGURES v

LIST OF TABLES ix

NOMENCLATURE xi

1 INTRODUCTION 1

- 1.1 Background 1
- 1.2 PEM Fuel Cell 3
  - 1.2.1 Components of PEM Fuel Cells 3
  - 1.2.2 Working of PEM Fuel cell 4
- 1.3 Gas Diffusion Layer 6
- 1.4 Motivation 7
- 1.5 Outline of the thesis 8
- 1.6 Closure 9

2 LITERATURE REVIEW 11

- 2.1 Clamping Mechanism 11
- 2.2 GDL Compression on mechanical properties 15
- 2.3 GDL Compression on electrical properties 17
- 2.4 GDL cyclic compression 19
- 2.5 GDL electrical/flow heterogeneity on PEFC performance 22
- 2.6 Relative humidity effects on PEFC performance 25
- 2.7 GDL Material Models 26
- 2.8 Conclusions from Literature Review 26
- 2.9 Research Objectives 27
- 2.10 Closure 28

3 INVESTIGATION OF ENDPLATE DESIGN CONFIGURATIONS AND GDL MATERIAL MODELS 29

3.1 Introduction 29

3.2 Methodology 29

3.2.1 Description of the design 30

3.2.2 Single-Cell Model 35

3.3 Results and Discussion 36

3.3.1 Interfacial contact pressure and contact resistance distribution 36

3.3.2 Equivalent stress distribution 43

3.3.3 Hydrostatic pressure distribution 46

3.3.4 Through-plane deformation 48

3.3.5 Bulk resistance and permeability distribution 49

3.4 Summary 50

3.5 Closure 51

4 EFFECTS OF GDL ELECTRICAL AND FLOW HETEROGENEITY ON PEFC PERFORMANCE 53

4.1 Introduction 53

4.2 Model Description 53

4.2.1 Numerical Model and Assumptions 53

4.2.2 Governing Equations 57

4.2.3 Boundary Conditions 63

4.3 Results and discussion 64

4.3.1 Cell performance 64

4.3.2 Hydrogen mass fraction distribution 65

4.3.3 Oxygen mass fraction distribution 67

4.3.4 Water content distributuion 69

    - 4.3.5 Local current density distribution 71
    - 4.3.6 Temperature distribution 72
    - 4.3.7 Water mass fraction distribution 73
    - 4.3.8 Cathodic overpotential distribution 75
  - 4.4 Summary 76
  - 4.5 Closure 78
- **5 COMPUTATIONAL ANALYSIS OF 25cm^2 ACTIVE AREA PEFC WITH HETEROGENEOUS GAS DIFFUSION LAYER 79**
  - 5.1 Introduction 79
  - 5.2 Computational model description 79
  - 5.3 Results and Discussion 81
    - 5.3.1 Cell Performance 81
    - 5.3.2 Hydrogen mass fraction distribution 82
    - 5.3.3 Oxygen mass fraction distribution 83
    - 5.3.4 Local current density distribution 84
    - 5.3.5 Water content distribution 85
    - 5.3.6 Temperature distribution 86
    - 5.3.7 Water mass fraction distribution 87
  - 5.4 Summary 88
  - 5.5 Closure 89
- **6 INVESTIGATION OF CYCLIC MECHANICAL RESPONSE OF GDL 91**
  - 6.1 Introduction 91
  - 6.2 Experimental Details 91
  - 6.3 Models and Analysis 93
    - 6.3.1 Linear Regression Analysis 93
  - 6.4 Results and Discussion 94

6.4.1 Mechanical response at various temperature..94

6.4.2 Effects of pre- and post-hotpress condition...95

6.4.3 Compressive strength 96

6.4.4 Elastic resilience..97

6.5 Summary 98

6.6 Closure 99

7 DEVELOPMENT OF PHENOMENOLOGICAL CONSTITUTIVE MODEL TO PREDICT CYCLIC BULK ELECTRICAL CONDUCTIVITY OF GDL . 101

7.1 Introduction...101

7.2 Methodology 102

7.2.1 Model Development 102

7.3 Results and Discussion...106

7.3.1 Model Response and Validation..106

7.3.2 Electrical cyclic conductivity response 108

7.3.3 Parametric Evaluation..111

7.3.4 Break stress behaviour...113

7.4 Summary 115

7.5 Closure 116

8 CONCLUSIONS AND FUTURE WORK 117

8.1 Conclusions...117

8.2 Scope for future work..118

REFERENCES 119

PUBLICATIONS...137

BIODATA..139

LIST OF FIGURES

Figure 1.1 Schematic of PEM fuel cell components..3

Figure 1.2 Single cell PEMFC configuration (O’Hayre et al. 2016)............................4

Figure 1.3 Microstructure SEM images of (a) Carbon Paper; (b) Carbon Cloth; (c) Carbon Felt (Qiu et al. 2018)..7

Figure 3.1 Schematic illustration of (a) Clamping-1; (b) Clamping-2........................30

Figure 3.2 Shows (a) bolt loading conditions; (b) boundary conditions; and (c) meshed model..35

Figure 3.3 The contact pressure distribution contours at the interface of BPP|GDL for (a) GDL as Isotropic; (b) GDL as incompressible hyperelastic; and (c) GDL as compressible hyperelastic model...37

Figure 3.4 The line plots of contact pressure distribution and interfacial contact resistance at the interface of BPP|GDL for (a) GDL as Isotropic; (b) GDL as incompressible hyperelastic; and (c) GDL as a compressible hyperelastic model......38

Figure 3.5 The contact pressure distribution contours at the interface of GDL|PEM for (a) GDL as Isotropic; (b) GDL as incompressible hyperelastic; and (c) GDL as compressible hyperelastic model...40

Figure 3.6 The line plots of contact pressure distribution at the interface of GDL|PEM for (a) GDL as Isotropic; (b) GDL as incompressible hyperelastic; and (c) GDL as compressible hyperelastic model...42

Figure 3.7 The equivalent stress distribution contours for GDL with (a) GDL as Isotropic; (b) GDL as incompressible hyperelastic; and (c) GDL as compressible hyperelastic model..43

Figure 3.8 The equivalent stress distribution contours for PEM with (a) GDL as Isotropic; (b) GDL as incompressible hyperelastic; and (c) GDL as compressible hyperelastic model..45

Figure 3.9 The Hydrostatic pressure distribution contours for PEM with (a) GDL as Isotropic; (b) GDL as incompressible hyperelastic; and (c) GDL as compressible hyperelastic model..47

Figure 3.10 The cross-sections showing differences in through-plane deformation (U3) in GDLs with (a) linear elastic isotropic; (b) incompressible hyperelastic; and (c) compressible hyperelastic GDL material models for (1) C-1; and (2) C-2 48

Figure 3.11 The line plots of bulk resistance and permeability distribution of GDL considering (a) GDL as Isotropic; (b) GDL as incompressible hyperelastic; and (c) GDL as compressible hyperelastic model 49

Figure 4.1 Schematic of single channel PEMFC with (a) Homogeneous GDL; (b) Heterogeneous GDL 54

Figure 4.2 Cell performance under (a) full humidification conditions, (b) different humidification conditions 64

Figure 4.3 Hydrogen mass fraction distribution in midsection of anode GDL at: (a) 0.6 V with full humidification, (b) 0.3 V with full humidification, (c) 0.6 V with different humifications, (d) 0.3 V with different humifications 65

Figure 4.4 Hydrogen mass fraction distribution in midsection of anode catalyst at: (a) 0.6 V with full humidification, (b) 0.3 V with full humidification, (c) 0.6 V with different humifications, (d) 0.3 V with different humifications 67

Figure 4.5 Oxygen mass fraction distribution in midsection of cathode GDL at: (a) 0.6 V with full humidification, (b) 0.3 V with full humidification, (c) 0.6 V with different humifications, (d) 0.3 V with different humifications 68

Figure 4.6 Oxygen mass fraction distribution in midsection of cathode catalyst at: (a) 0.6 V with full humidification, (b) 0.3 V with full humidification, (c) 0.6 V with different humifications, (d) 0.3 V with different humifications 69

Figure 4.7 Water content distribution in midsection of membrane at: (a) 0.6 V with full humidification, (b) 0.3 V with full humidification, (c) 0.6 V with different humifications, (d) 0.3 V with different humifications 70

Figure 4.8 Local current distribution in midsection of membrane at: (a) 0.6 V with full humidification, (b) 0.3 V with full humidification, (c) 0.6 V with different humifications, (d) 0.3 V with different humifications 71

Figure 4.9 Temperature distribution in midsection of membrane at: (a) 0.6 V with full humidification, (b) 0.3 V with full humidification, (c) 0.6 V with different humifications, (d) 0.3 V with different humifications 72

Figure 4.10 Water mass fraction distribution in midsection of cathode catalyst at: (a) 0.6 V with full humidification, (b) 0.3 V with full humidification, (c) 0.6 V with different humifications, (d) 0.3 V with different humifications 74
Figure 4.11 Cathodic overpotential in midsection of cathode catalyst at: (a) 0.6 V with full humidification, (b) 0.3 V with full humidification, (c) 0.6 V with different humification, (d) 0.3 V with different humifications..75
Figure 5.1 Schematic illustration of multichannel PEMFC with an active area of 80
Figure 5.2 Computational mesh model of PEMFC 81
Figure 5.3 Performance of the PEMFC for C-1 and C-2 design 82
Figure 5.4 Hydrogen mass fraction distribution in mid-section of anode GDL at 0.3V for (a) C-1 design; (b) C-2 design..82
Figure 5.5 Oxygen mass fraction distribution in mid-section of cathode GDL at 0.3V for (a) C-1 design; (b) C-2 design..84
Figure 5.6 Local current density distribution in mid-section of membrane at 0.3V for (a) C-1 design; (b) C-2 design 85
Figure 5.7 Water content distribution in mid-section of membrane at 0.3V for (a) C-1 design; (b) C-2 design..86
Figure 5.8 Temperature distribution in mid-section of membrane at 0.3V for (a) C-1 design; (b) C-2 design..86
Figure 5.9 Water mass fraction distribution in mid-section of cathode catalyst at 0.3V for (a) C-1 design; (b) C-2 design..87
Figure 6.1 Experimental setup at (a) room temperature; (b) different temperature; (c) pre hot- press condition; (d) post hot-press condition 92
Figure 6.2 Linear regression analysis using Qualitative analysis 93
Figure 6.3 Mechanical Response at different temperature for (a) GDL with MPL, (b) GDL without MPL...94
Figure 6.4 Effects of pre and post hot press for (a) GDL with MPL, (b) GDL without MPL 95
Figure 6.5 Effects of GDL response for (a) Pre-Hotpress condition; (b) Post-Hotpress condition 96
Figure 6.6 Compressive strength of GDL materials under pre- and post-hotpress conditions...97

Figure 6.7 Elastic resilience of GDL materials under pre- and post-hotpress conditions 98
Figure 7.1 Variation of porosity parameter with compressive stress........ 104
Figure 7.2 Schematic representation of expected variation in electrical conductivity of GDL with cyclic compressive stress........ 105
Figure 7.3 Simulated response of electrical conductivity as a function of compressive stress. The response is validated against experimental data. The values of model variables are noted in the figure........ 106
Figure 7.4 Simulated cyclic response with example maximum compressive stress limit of σ = 2.5MPa. The response is validated against experimental data. The values of model variables are noted in the figure. 107
Figure 7.5 Simulated cyclic response with example maximum compressive stress limits of σ = 2 MPa, 3 MPa, and 4 MPa. 108
Figure 7.6 Simulated repetitive cyclic response with example maximum compressive stress limits of σ = 2 MPa, 3 MPa, and 4 MPa........ 109
Figure 7.7 Variation of residual electrical conductivity for repetitive stress cycles.. 110
Figure 7.8 Parametric evaluation for parameters: (a) porosity parameter 'C1'; (b) fiber contact density parameter 'C2'; and (c) saturation limit parameter 'd' 111
Figure 7.9 Model response curves (a): for applied compressive load is less than the threshold limit; (b): for applied compressive load is same as threshold limit and its influence on subsequent cycle of same stress limit with break stress factor enabled; (c) with break stress and without break stress factor for stress load beyond threshold limit; (d) with break stress and without break stress factor for repetitive stress cycles. 113

LIST OF TABLES

Table 1.1 Functions and types of different PEMFC components.................................4

Table 2.1 Effects of clamping mechanism..15

Table 2.2 Effects of GDL compression on mechanical properties 17

Table 2.3 Effects of GDL compression on electrical properties.................................19

Table 2.4 Effects of GDL cyclic compression...22

Table 2.5 Effects of GDL electrical/flow heterogeneity on PEFC performance.........24

Table 2.6 Effects of relative humidity effects on PEFC performance.........................25

Table 3.1 Geometrical dimensions and material properties of PEFC components 31

Table 3.2 Incompressible hyperelastic material constants for GDL model.................32

Table 3.3 Compressible hyperelastic material constants for GDL model 32

Table 3.4 Comparison of this study with literature...51

Table 4.1 Geometrical parameters and operating conditions......................................55

Table 4.2 Parameters considered in the numerical model 56

Table 4.3 Parameters of heterogeneous GDL porosity, permeability and ICR at interface of GDL|CC..57

Table 4.4 List of source terms considered in governing equations.............................59

Table 4.5 Comparison of this study with literature...77

Table 5.1 Comparison of the present study with literature..89

Table 6.1 Comparison of the current study with literature 99

Table 7.1 Comparison of the current study with literature 116

x

NOMENCLATURE

Symbols

a	effective surface area, 1/m
A	active area, m^2
C	mole concentration, mol/m^3
C_{io}	material parameter for shear modulus, MPa
C_1	function of porosity parameter
C_2	function of contact density between carbon fibers parameter
c_p	specific heat, J/Kg·K
D	effective diffusivity, m^2/ s
D_i	material parameter for bulk modulus, 1/MPa
d	local GDL thickness before compression, mm
d_0	local GDL thickness after compression, mm
EW	equivalent weight
e	Local deformation of GDL, mm
F	Faradays constant, 96,485 C/mol
i	exchange current density, A/m^2
I	current density, A/m^2
j	volumetric current density, A/m^3
k	thermal conductivity, W/m.K
K	permeability, m^2
M	molecular weight, kg/mol
P	pressure, Pa
Q	mass flow rate, kg/s
R	universal gas constant, 8.314 J/mol.K
R_b	bulk resistance, $m\Omega.cm^2$
ρ_f	resistivity of carbon fibre, Ωm
S	source term
T	temperature, K
$\vec{u}$	velocity vector, m/s

U	inlet velocity, m/s
V	voltage, V
X	mole fraction
Y	mass fraction

Greek Letters

α	transfer coefficient
ε	porosity
η	over-potential, V
μ	dynamic viscosity, Pa s
ξ	stoichiometric ratio
ρ	density, kg/m^3
σ	electron/proton conductivity, S/m
ϕ	potential, V
θ	contact angle
γ	mass exchange rate constants
λ	water content

Superscripts and subscripts

a	anode
c	cathode
cl	catalyst layer
eq	equilibrium
eff	effective
f	fluid
g	gas
gdl	gas diffusion layer
H_2	hydrogen
H_2O	water
O_2	oxygen

i	i^{th} species
m	membrane/mixture
mass	mass equation
mom	momentum equation
ref	reference
s	solid
sat	saturation
wv	water vapour

Abbreviations

BPP	Bipolar Plate
CC	Current Collector
CL	Catalyst Layer
GDL	Gas Diffusion Layer
HOR	Hydrogen Oxidation Reaction
ICR	Interfacial Contact Resistance
MEA	Membrane Electrode Assembly
MPL	Micro Porous Layer
ORR	Oxygen Reduction Reaction
PEFC	Polymer Electrolyte Fuel Cell
PEM	Polymer Electrolyte Membrane
PEMFC	Polymer Electrolyte Membrane Fuel Cell
PTFE	Poly Tetra Fluoro Ethylene
RH	Relative Humidity

CHAPTER 1

INTRODUCTION

Transportation is a fundamental requirement of modern life. As the population has grown, the need for motorised vehicles has increased. Over the years, the demand for motor vehicles has expanded dramatically. The rising number of automobiles on the road has severely impacted the environment, generating air pollution and greenhouse gas emissions, which is a serious issue. In addition, the depletion of fossil fuels and their environmental repercussions have made it vital to switch to other methods of generating power for transportation. Fuel cells are a promising alternative to conventional power generation. Not only does it assist in reducing greenhouse gas emissions, but it also helps reduce the world's dependence on fossil fuels. Most fuel cells utilise hydrogen produced from renewable sources such as biomass, wind, and solar energy.

1.1 Background

Fuel cells are electrochemical systems that efficiently convert the chemical energy of reactants into electricity. Fuel cells require fuel as input and generate electricity as output. A fuel cell will continue to create products (electricity) as long as raw materials (fuel) are supplied. Unlike a battery, the reactants in a fuel cell are supplied from an external source, and the products are removed from the reaction site. Consequently, fuel cells are recognised as a direct and efficient energy conversion of chemical energy of fuel and oxidant into electrical energy that is now prepared to compete for clean power generation in a variety of fields.

Fuel cells are more efficient and reliable than combustion engines due to their direct energy conversion. In addition, direct energy conversion eliminates noise and vibration from the fuel cell. A fuel cell typically consists of three active components: an anode electrode, a cathode electrode, and an electrolyte between the two electrodes. Fuel cells are categorised based on criteria such as their electrolyte type, operating temperature, and the type of ion transported by the electrolytes.

The most prevalent fuel cell types are:

1. Proton exchange membrane fuel cell (PEMFC or PEFC)
2. Solid oxide fuel cell (SOFC)
3. Alkaline fuel cell (AFC)
4. Phosphoric acid fuel cells (PAFC)
5. Molten carbonate fuel cell (MCFC)

Proton exchange membrane or Polymer electrolyte membrane (PEM) fuel cells are the best suitable for mobile applications out of all the numerous types of fuel cells. PEM fuel cells have significant benefits, including high efficiency even at partial loads, low operating temperature (below 85^{o}C), high power density, and zero emissions (Gandiglio et al. 2014), (Shimpalee et al. 2011), (Wang et al. 2011). However, the presence of a solid polymer electrolyte is what distinguishes a PEM fuel cell from others. With all the advantages of solid electrolytes, PEM fuel cells are the optimal choice for mobile applications. However, technological obstacles and limitations such as cost, durability, and performance have impeded their commercialization. Even though research and development have made significant strides toward overcoming these obstacles, additional effort is necessary before this technology can be broadly adopted.

1.2 PEM Fuel Cell

1.2.1 Components of PEM Fuel Cells

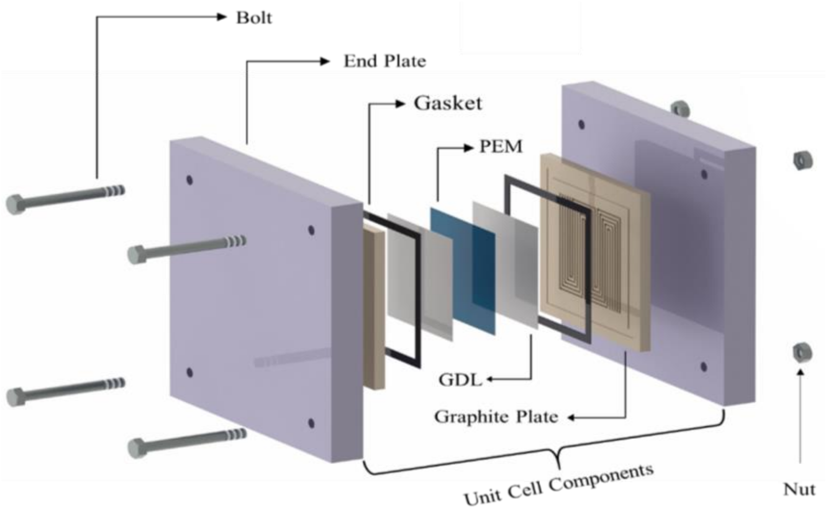

Figure 1.1 Schematic of PEM fuel cell components

A PEM fuel cell has a multi-layered architecture and is typically composed of anode and cathode flow field plates and a membrane electrode assembly (MEA), as depicted schematically in Figure 1.1 (B. Liu, L.F. Liu, M.Y. Wei 2016).

Table 1.1 describes the functions of each component of a PEFC. The flow field plates are primarily responsible for the distribution of hydrogen and oxygen via flow channels across the different MEA surfaces. The fuel cell system's key component is the MEA, which comprises anode and cathode sides separated by a proton-conducting membrane. The membrane is mainly responsible for proton transport from the anode to the cathode and acting as a barrier to prevent additional reactants, by-products, and electron species from reaching the cathode.

The catalyst layer consists of electrochemically active platinum nanoparticles scattered atop carbon or graphite particles that are relatively larger (Tsushima and Hirai 2011). All of these particles are surrounded by an ionomer, such that the catalyst layer serves as a platform for the transit of reactants, products, and charged species, such as electrons and protons (Shahgaldi et al. 2018b; Zhao et al. 2018). To effectively transport protons, both the ionomer and the membrane must be hydrated.

Table 1.1 Functions and types of different PEMFC components

Component	Description	Common Types
Proton exchange membrane	Allows protons to flow from the anode to the cathode.	Perfluoro sulfonic acid membrane (Nafion 112, 115, 117)
Catalyst layers	Breaks down the fuel into protons and electrons. The proton reacts with the oxidant at the fuel cell cathode to generate water. The electrons travel to the load.	Platinum/Carbon catalyst
Gas diffusion layers	Allows fuel/oxidant to pass through the porous layer while simultaneously collecting electrons.	Carbon cloth or Carbon paper or Carbon felt
Flow field plates	Distributes the fuel and oxygen to the gas diffusion layer	Graphite, Stainless steel
Gaskets	It prevents fuel leakage and aids in facilitating uniform pressure distribution	Silicon, Teflon
End plates	Supports stacked layers	Stainless steel, graphite, polyethylene, PVC

1.2.2 Working of PEM Fuel cell

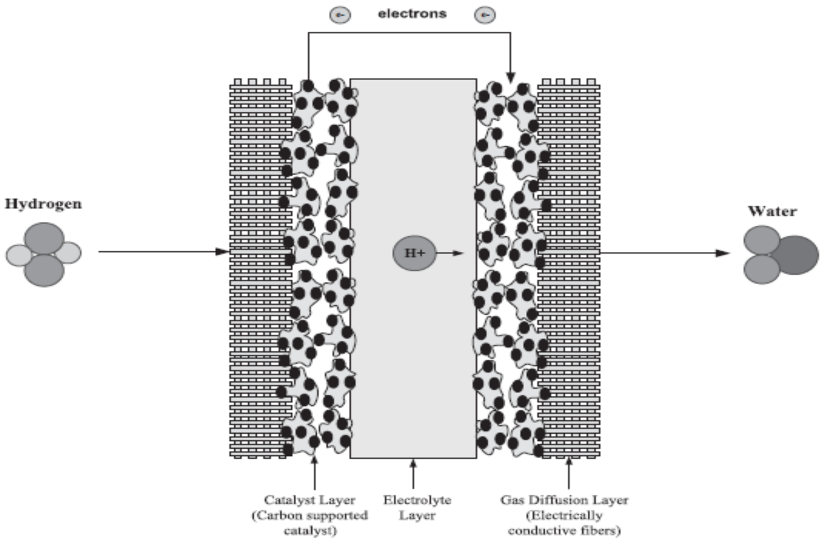
e-
electrons
e-
Hydrogen
H+
Water
Catalyst Layer (Carbon supported catalyst)
Electrolyte Layer
Gas Diffusion Layer (Electrically conductive fibers)

Figure 1.2 Single cell PEMFC configuration (O’Hayre et al. 2016)

The main fuel is hydrogen, delivered via the anode side's flow channel. The catalyst composed of platinum converts hydrogen into positively charged hydrogen ions and negatively charged electrons. As depicted in Figure 1.2, the electrolyte membrane only permits positively charged ions to pass through, forcing the electrons to go through an external circuit to the cathode, thereby generating an electrical current.

The anode-side reaction is shown below,

$$H_2 \rightarrow 2H^+ + 2e^- \tag{1.1}$$

As the oxidant on the cathode side, oxygen from the air is provided via the flow channel. Through the gas diffusion layer, oxygen reaches the catalyst layer of the cathode. At the membrane interface, oxygen molecules combine with the anode-transferred electrons and protons (H^+) to produce water.

The cathode-side reaction is shown below,

$$\frac{1}{2}O_2 + 2H^+ + 2e^- \rightarrow H_2O \tag{1.2}$$

Since the chemical energy contained in hydrogen and oxygen cannot be completely transformed into electrical energy, waste heat is a byproduct of this chemical reaction.

Thus, by combining the above two reactions at each electrode, the entire cell reaction is given below

$$\frac{1}{2}O_2 + 2H_2 \rightarrow H_2O + Electrical\ Energy + Waste\ Heat \tag{1.3}$$

The heat produced can have a negative impact on cell performance by raising the average cell temperature and establishing a temperature gradient throughout the cell. Water produced can impair cell function by obstructing the flow of reactants to reaction sites. Thus, the products must be removed for the cell to function efficiently.

1.3 Gas Diffusion Layer

Gas diffusion layer (GDL) is one of the primary components of PEM fuel cells. GDL materials are highly porous, ranging from 70-80% porosity and 100µm to 300µm in thickness. GDL generally serves multiple roles in cell functioning by controlling mass, heat, and electron transport. GDL is located between the catalyst layer and the flow channel plate and serves the following purposes (Ge et al. 2006; Millichamp et al. 2015; Ozden et al. 2019; Wang et al. 2011):

- Removing heat and by-products from the reaction site.
- Achieving a uniform distribution of reactants across all reaction sites.
- Conducting electrons with low resistance
- Offering structural support to the membrane.

Carbon fiber-based products are the most promising materials used in commercial GDLs because of high porosity and excellent electric conductivity. GDLs are of various types, carbon paper, carbon felt, and carbon cloth their respective microstructures are shown in Figure 1.3. The carbon fibres are distributed in a matrix form in the case of carbon paper, woven form in the case of carbon cloth and structure hydro-entangled form in carbon felt. Escribano et al. (2006) demonstrated how variations in microstructure impact the characteristics of GDLs. Figure 1.3 depicts the microstructures of three GDLs recorded by a scanning electron microscope. Carbon paper is composed of multilayered fibres randomly dispersed parallel to the material's surface, i.e. in the in-plane direction, and a binder to bond the adjacent stacked fibres. The fibres congregate around the graphitized binder to form an integral component. Instead of being held together by a binder, the woven pattern structure created by the roll-to-roll process provides the mechanical integrity of the fibres, as shown in Figure 1.3(b), and as shown in Figure 1.3(c), the fibres with tortuosity are oriented in the in-plane and through-plane direction to preserve their integrity after the hydro-entanglement process. GDL is commonly treated with polytetrafluoroethylene (PTFE) covering to prevent water from flooding its pores (Qiu et al. 2017).

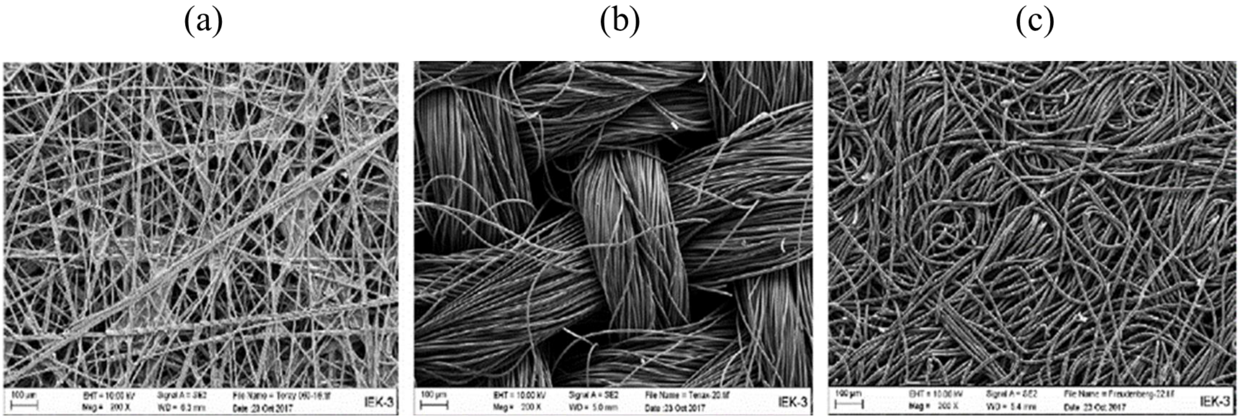

Figure 1.3 Microstructure SEM images of (a) Carbon Paper; (b) Carbon Cloth; (c) Carbon Felt (Qiu et al. 2018)

Due to the significant role of GDL, its volumetric properties, including gas permeability, porosity, electrical and thermal conductivity, and gas diffusivity, can directly impact the operation of the PEM fuel cell (Zhou and Wu 2007). Components of PEMFCs are known to degrade much faster than is required for the commercial success of this technology. To increase the operating lifetime of the PEMFC stacks, servicing procedures such as identifying and replacing underperforming components will likely be required. Due to the opening and rebuilding of the fuel cell stack, fuel cell components undergo cyclic compression and expansion during service operations. As the working conditions of the PEMFC cell create cyclic effects, it is very desired to investigate the local cyclic response of the aforementioned properties in order to comprehend the performance limiting factors of PEFCs. In addition, relative humidity and temperature variations cause hygro-thermal stresses in GDL and membrane to fluctuate, resulting in a cyclical effect. This cyclic compression may further deteriorate PEMFC components. Therefore, this study focuses on the impact of GDL compression on the electrical and mechanical properties of PEM fuel cells and their performance.

1.4 Motivation

The performance and durability of PEM fuel cells must be improved significantly. Understanding the GDL's mechanical, thermal, and electrical properties is crucial for enhancing the performance of PEM fuel cells. The compression of the GDL significantly impacts these properties due to clamping forces and hygro-thermal stresses. The GDL's electrical characteristics are enhanced as the compressive stresses increase. By reducing pore volume, compression can simultaneously have a detrimental effect on other physical properties, including permeability, porosity, and gas diffusivity. To achieve a uniform pressure distribution and a lower interfacial contact resistance on the GDL, a substantial amount of effort must be expended. Stresses that are excessive can alter the GDL's microstructure and result in mechanical degradation. In order to further develop PEM fuel cell technology, it is necessary to comprehend the compressive behaviour of GDL under monotonic as well as cyclic loadings.

1.5 Outline of the thesis

The thesis contains eight chapters, and a brief description of the contents of each chapter is given below:

Chapter 1 briefly describes the background, various fuel cell types, and operation of general PEM fuel cells. This study investigates one of the primary components of PEM fuel cells, the GDL, which is briefly discussed in this chapter.

Chapter 2 presents a compressive literature review on GDL behaviour based on the clamping mechanism and its effects on electrical and mechanical properties. The review also involves studies on the cyclic electrical and mechanical behaviour of GDL. The research gaps identified from the literature helped in framing the objectives of the present work.

Chapter 3 describes the numerical investigation carried on two clamping endplate configurations and their related impact on different components of PEM fuel cells. Various mechanical and electrical properties are evaluated and analysed.

Chapter 4 examines the electrical/flow heterogeneity of the GDL on single-channel PEFC under varying inlet humidity conditions. The chapter details on the transport characteristics and performance evaluation of single-channel PEFC.

Chapter 5 investigates the two endplate configurations in evaluating the transport behaviour and PEFC cell performance. This study reports for multi-flow channel PEFC having an active area of 25cm^2.

Chapter 6 reports on the experimental investigation in evaluating the cyclic mechanical response of GDL. The behaviour of GDL with and without MPL under different temperatures and pre- and post-hotpress conditions are discussed.

Chapter 7 presents the developed phenomenological constitutive model in predicting the cyclic bulk electrical conductivity response of GDL under different stress limits. The behaviour of GDL under a threshold limit known as break stress is also reported.

Chapter 8 summarizes the present work with concluding remarks and addresses the scope for future research.

1.6 Closure

This chapter introduced the background of fuel cells, the different types of fuel cells, and the fundamental operating principle of PEMFC. The chapter also includes an introduction to GDL, which is the primary focus of this study. The outline of the thesis is also presented. The following chapter is devoted to an extensive literature review of this research work.

CHAPTER 2

LITERATURE REVIEW

The GDL's porous structure provides mechanical support and protection for the membrane and catalyst layer during the assembly and operation of the cell. The GDL is developed explicitly as a porous material, leading to changes in its physical properties when subjected to compressive force. Mechanical contact between the field flow plate (also called graphite plates) and the gas distribution layer (GDL) directly correlates with stack performance. Standard compression is achieved with tie rods that run along the length of the stack and clamp the end plates, providing structural stability, preventing the movement of individual cells, plates, or MEAs, and, most importantly, compressing components to ensure good electrical contact and that the stack is sealed (Millichamp et al. 2015). The work focuses primarily on the effect of GDL compression on its electromechanical properties and cell performance.

2.1 Clamping Mechanism

An efficient PEFC clamping mechanism offers mechanical support and ensures the cells integrity. Thus, in a way, it aids in reducing the contact and bulk resistance of the fuel cell components. The clamping system with an unequal contact pressure distribution over the MEA, where compression pressure is much lower in the centre than at the edges, causes non-uniform current density and heat generation.(Asghari et al. 2010; Millichamp et al. 2015). High clamping pressure on the PEFC reduces the contact resistance at the BPP|GDL interface (Atyabi et al. 2019; Yan et al. 2020). Also, very high pressure may reduce GDL’s porosity (Bates et al. 2013; Fu et al. 2007; García-Salaberri et al. 2019; Jha et al. 2020; Montanini et al. 2009; Patermarakis and Papandreadis 1993). In certain end plate configuration, the resistance at the BPP|GDL interface has contributed to a 59% reduction in overall power loss (Thompson 1997; Zhang et al. 2006; Zhou et al. 2011).

To this end, Wen et al. (2009) investigated the effects of clamping force and various bolt configurations of clamping mechanism on unit cells and a ten-cell stack. They showed that the uniform contact pressure distribution significantly reduced ohmic resistance and mass transport losses in the PEFCs. Wang et al. (2008) proposed an alternative clamping mechanism designed to have an inbuilt hydraulically pressurized pocket in the endplate. They demonstrated that pressurised hydraulic fluid passing through an in-built pocket can considerably contribute to more uniform pressure distribution and improve fuel cell performance. Chung et al. (2016) proposed an effective clamping method and demonstrated to control structural bending and deformation resistance of the endplates. An intelligent approach is adopted by Qui et al. (2020) to enhance the contact pressure uniformity between BPP and GDL by optimizing the clamping forces and endplate positions. They proved that the neural network optimization framework achieves greater computing efficiency in fuel cell deformation prediction. Chien et al. (2016) investigated the effects of bolts preloading on cell performance. They reported that the compression ratio of GDL increased with increasing preloading and suggested a 15% threshold for a positive impact on cell efficiency. Atifi et al. (2019) investigated a two-dimensional finite element model with varying contact pressure to obtain the displacement on the GDL. The analysis accounted in relative humidity and operating temperature while considering GDL to be an orthotropic material.

Mikkola et al. (2009) designed a three-dimensional finite element model to predict the compression pressure and deformation of components in fuel cell stacks. Besides, they explained that the model could be used to optimise any fuel cell structure at different temperatures. Ouaidat et al. (2020) explored the effects of physical properties on fuel cell components using the design of experiment (DOE) approach. The results exhibit that the maximum contact pressure is established at the GDL detaching point from the bipolar plate resulting in intense pressure. They investigated contact resistance analytically using a mechanical model and reported that low porosity permits identification of optimal parameters for GDL thickness, pore diameters, and BPP bending radius. Irmscher et al. (2019) reported that the optimal range for contact pressure on the active surface relies on the type of GDL material utilized. Among the different materials SGL 29BCE, Freudenberg H2315C2, and Toray TGP H060, the team revealed that the Freudenberg H2315C2 material type had a wide range of contact pressure that could withstand higher pressures. Zhou et al. (2020) considered BPP and MEA combined into a single component. They observed that the high stiffness of the endplate and the increase in the number of cells contribute to uniform contact pressure distribution. Carrel and Mele (2014) developed a FEM model to study the behaviour of MEA with a variable number of cells (2-16 cells) in PEMFC stacks. With a greater number of cells, they demonstrated numerically and experimentally that compression of MEA in the centre of the stack could be more uniform. Dey et al. (2019) addressed the influence of cell geometry, bolt configuration, and gasket thickness to achieve uniform contact pressure. The authors discovered that extruded hexagonal endplates produced a more uniform contact pressure distribution. Hu et al. (2018) performed a numerical analysis to investigate the stress and deformations of the two different cell assemblies, one for a single-cell PEFC and the other for ten-cell stacks at various loads, to provide an efficient connection with the real stack assembly.

A parametric study by Lee and Yang (2020) revealed an interrelationship between the GDL and membrane for GDL deformation. They concluded that the GDL's through-plane stiffness plays a vital role in its deformation. Xiao et al. (2019) performed simulations to analyze stress and strain distribution using the reconstructed GDL. Simulation outcomes predict that the GDL’s fiber displacement in the through-plane direction is substantially higher than in-plane. Millichamp et al. (2015) review states that compression in PEFCs poses a significant technical challenge to ensure durability and stable performance. In addition, a complete investigation was undertaken on the effects of mechanical compression and dimensional change on PEFCs components utilising various alternate compression techniques to accomplish the needed stack compression. Strap devices that function by wrapping the fuel cell stack with many bands of different materials create an equal distribution of force. In addition, a comprehensive investigation was undertaken on the effects of mechanical compression and dimensional change on PEFCs components utilising various alternate compression techniques to accomplish the needed stack compression. Strap devices that function by wrapping the fuel cell stack with many bands of different materials create an equal distribution of force. This type of strap device induces a much larger area being compressed against the endplate, almost leading to even force distribution (Barton 2013; Murphy et al. 2000; Ozgur 2009; Wozniczka et al. 1999). Due to the greater number of compression points, the various available clamping methods, such as the Crimp system mechanism model and the strap design model, result in a more uniform compression across the cell. However, the forces applied to the fuel cells are still higher due to clamping forces on the outer edges (Barton and Voss 1997; Hebling et al. 2005). Alizadeh et al. (2017) proposed a pneumatically exerted clamping mechanism on the PEMFC assembly for the uniform contact pressure distribution using the finite element method. According to their findings, the new clamping mechanism offers a more stable contact pressure distribution than the standard clamping mechanism. To achieve uniform contact pressure distribution at the interface, Barzegari et al. (2020) optimized a pneumatic clamping system by varying geometric parameters. The findings revealed the weight and reliability of the optimized pneumatic system lead to better results than the conventional endplate configuration. In light of this discussion, it is thus clear that the type of clamping mechanism plays a crucial role in achieving uniform distribution of various properties in PEM fuel cell components.

From the above discussion and from Table 2.1 it is clear that although numerous experimental techniques of endplate designs provide a suitable answer to the problem of nonuniform contact pressure, these techniques are time-consuming and not cost-effective. The design requirements for an efficient clamping mechanism (a device that provides uniform pressure distribution over the active region of the cell) rise as the active area of the stack increases. Random design selection may degrade system performance and increase maintenance expenses. Therefore, to obtain greater stability with enhanced performance, it is vital to have a stack clamping design that is effective.

Table 2.1 Effects of clamping mechanism

Author	Outcome/Inferences
Wang et al. (2008)	An alternative clamping mechanism is designed to have an inbuilt hydraulically pressurized pocket in the endplate to obtain more uniform pressure distribution and improve fuel cell performance.
Carrel and Mele (2014)	With greater number of cells (2-16) it is demonstrated numerically and experimentally that compression of MEA in the centre of the stack could be more uniform.
Dey et al. (2019)	The influence of cell geometry, bolt configuration, and gasket thickness to achieve uniform contact pressure is studied. The authors also discovered that extruded hexagonal endplates produced a more uniform contact pressure distribution.
Alizadeh et al. (2017)	Developed a pneumatically exerted clamping mechanism on the PEMFC assembly for the uniform contact pressure distribution using the finite element method.
Barzegari et al. (2020)	Optimized a pneumatic clamping system by varying geometric parameters. The findings revealed the weight and reliability of the optimized pneumatic system lead to better results than the conventional endplate configuration.

2.2 GDL Compression on mechanical properties

The impact of GDL deformation on PEFC performance is a well-researched topic. This is due to variations in physical properties such as permeability, porosity, thermal and electrical contact resistance, and bulk resistance caused during highly porous GDL compression deformation (Atyabi et al. 2019; Movahedi et al. 2018; Mukherjee et al. 2020; Omrani and Shabani 2019; Ouaidat et al. 2020; Qiu et al. 2017; Sow et al. 2015)

Several researches have been conducted on the influence of compression on the mechanical properties of the GDL. Efforts have been made to link GDL deformation to the ohmic response. Mason et al. (2012) demonstrated that the GDL under compression pressure leads to a nonlinear decline in resistance. They arrived at the conclusion that an analytical technique based on simultaneous displacement and resistance measurement in GDLs is necessary. Norouzifard and Bahrami (2014a) developed an analytical model for a unit cell that considers various microstructural parameters and porous medium properties such as carbon fibre diameter, elastic modulus, pore size, and porosity. They found that the model may be used to simulate GDL deformations and investigate GDL structural characteristics. Espinoza et al. (2015) carried 2D analysis to evaluate the porosity, gas-phase tortuosity, and through-plane permeability in GDL. Xiao et al. (2020) developed an advanced analytical model to interpret realistic GDL deformations under compression.

Zhang et al. (2020) revealed that contact pairs and pore space play an essential role in deciding the nonlinearity of the compressive curve. They also showed that average porosity decreases with increasing pressure in GDL, resulting in a non-uniform distribution of porosity in the through-plane direction. Ouaidat et al. (2020) reported that higher clamping pressure decreases pore diameter and thickness, leading to nonlinear deformation of the GDL material. Several studies on the compression effects on various properties and morphology of GDL carbon fibres have been conducted (Atifi et al. 2019; Fly et al. 2019; Lee and Yang 2020; Norouzifard and Bahrami 2014b; Uzundurukan et al. 2020; Wang et al. 2016, 2017b).

However, understanding the localized variation of these physical properties is not reported. This can be a complex process experimentally, and currently, no models can relate these changes to the cyclic response of GDLs. As a result, extensive work needs to be carried out suggesting a model to handle this issue. Table 2.2 discusses brief outcomes of the literature of GDL compression on mechanical properties.

Table 2.2 Effects of GDL compression on mechanical properties

Author	Outcome/Inferences
Mason et al. (2012)	The GDL under compressive pressure leads to a nonlinear decline in resistance. Authors arrived at the conclusion that an analytical technique based on simultaneous displacement and resistance measurement in GDLs is necessary.
Norouzifard and Bahrami (2014a)	An analytical model is developed that considers various microstructural parameters and porous medium properties such as carbon fibre diameter, elastic modulus, pore size, and porosity. It is found that the model may be used to simulate GDL deformations and investigate GDL structural characteristics.
Ouaidat et al. (2020)	The higher clamping pressure decreases pore diameter and thickness, leading to nonlinear deformation of the GDL material.
Zhang et al. (2020)	The contact pairs and pore space play an essential role in deciding the nonlinearity of the compressive curve is revealed. It is showed the average porosity decreases with increasing pressure in GDL, resulting in a non-uniform distribution of porosity in the through-plane direction.

2.3 GDL Compression on electrical properties

The electrical properties of porous GDL are a critical aspect of PEMFC research and have been found to be highly sensitive to compressive pressure, impacting cell performance. To this end, Qui et al. (2017) developed an analytical model capable of assessing electrical contact resistance (ECR) between a solid material and porous material, which is used to indicate the power loss between GDL and BPP in the fuel cell. Chien et al. (2016) numerically assessed the effects of different bolt pre-loadings on the performance of the GDL. They noticed a decrease in total contact resistance and porosity as a result of compression and stated that reasonable cell performance is attained at 4 MPa. Ye et al. (2014) reported that carbon paper has lower bulk and contact resistance than carbon cloth due to a higher uniform surface topography. Chang et al. (2007) examined the clamping pressure effects on the performance of PEMFC and proved that the lower clamping pressure results in high interfacial resistance between BPP|GDL. They also revealed that increased clamping pressure reduces the diffusion path for mass transfer from gas channels to catalyst layers. Sow et al. (2015) reported a novel technique using an experimental setup to evaluate interfacial and bulk properties separately of GDLs. Their findings revealed that contact resistance is more prominent than total resistance, with through-plane bulk resistivity accounting for around 10% of total resistivity. An experimental investigation by Hamour et al. (2015) for GDL and BPP demonstrated that electrical conductivity largely relies on the applied mechanical compression during operation. Zamel et al. (2012) analyzed the 3D reconstruction of GDL's carbon paper material with fibres of different orientations used to achieve numerically in-plane and through-plane electrical conductivity. They proved that the through-plane electrical conductivity is lower than the in-plane. El Oualid et al. (2017) reported the nonlinear behavior of electrical contact resistance for different GDL types under static compressive loads. They demonstrated that the constant values of electrical contact resistance are obtained at 5MPa compressive pressure, which is due to the reordering of GDL carbon fibres reaching a physical compaction limit

The assessment of interfacial contact resistance (ICR) at the interface of BPP|GDL, bulk resistance, and permeability in GDL using various analytical models has been reported in several literatures (Gaiselmann et al. 2014; Ge et al. 2006; Kandlikar et al. 2009; Mukherjee et al. 2020; Omrani and Shabani 2019; Radhakrishnan and Haridoss 2011; Su et al. 2008; Wang and Chen 2011).

The outcomes and inference on electrical properties with GDL compression is briefly summarised in Table 2.3. It is that the electrical properties of GDL, namely bulk resistance, contact resistance, and total ohmic contributions, have been comprehensively linked to compression but under non-localized and non-cyclic conditions.

Table 2.3 Effects of GDL compression on electrical properties

Author	Outcome/Inferences
Qui et al. (2017)	An analytical model is developed capable of assessing electrical contact resistance (ECR) between a solid material and porous material, used to indicate the power loss between GDL and BPP in the fuel cell.
Chien et al. (2016)	A decrease in total contact resistance and porosity as a result of compression is revealed and stated that reasonable cell performance is attained at 4 MPa.
Chang et al. (2007)	The effects of clamping load on the performance of PEMFC lead to lower clamping pressure resulting in high interfacial resistance between BPP|GDL. It is revealed that increased clamping pressure reduces the diffusion path for mass transfer from gas channels to catalyst layers.
Sow et al. (2015)	Reported a novel technique using an experimental setup to evaluate interfacial and bulk properties separately of GDLs. Findings revealed the contact resistance is more prominent than total resistance, with through-plane bulk resistivity accounting for around 10% of total resistivity.
El Oualid et al. (2017)	The constant values of electrical contact resistance are obtained at 5MPa compressive pressure, which is due to the reordering of GDL carbon fibres reaching a physical compaction limit

2.4 GDL cyclic compression

As the operating conditions of PEFC cells create cyclic effects, it is essential to investigate the local cyclic response of the electromechanical properties in order to understand the performance limiting factors of PEFCs. In practice, changes in relative humidity and temperature cause variation in hygro-thermal stresses in GDL and membrane, thus resulting in a cyclic effect (Kusoglu et al. 2006; Lu et al. 2011;

Silberstein and Boyce 2011; Solasi et al. 2007). To this end, Radhakrishnan and Haridoss (2010) outlined the impact of cyclic compression on GDL, resulting in irreversible changes in pore size and electrical resistance. Nevertheless, the article fails to explain the reversible behaviour of GDL in terms of electrical resistance. Sadeghi et al. (2010) experimented on GDL's Toray carbon paper to reveal that the values of geometric, mechanical, and thermal parameters reach a steady state after five loading-unloading cycles leading to no further changes. Gigos et al. (2015) too revealed that under high cyclic loads, the behavior of GDL approaches a steady state after 5-6 cycles. In addition, they developed an analytical model whose behaviour mimics that of the real GDL, which forecasts the model's validation. Koorata and Bhat (2020, 2021) proposed a phenomenological model to predict the cyclic response of the gas diffusion media. Taking into account GDL as a constituent of porous matrix and reinforced fibre phases, they developed a model predicting the residual strain, hysteresis, and damage quotient involved in stress softening. Bouziane et al. (2020) investigated the effects of different GDL structures on electrical contact resistance. They revealed that the SGL type yielded the highest contact resistance, and the felt type exhibited lower deviation rates between compression cycles. Todd et al. (2016) reported the through-plane resistivity decreases with cyclic compression while in-plane resistivity increases. The behaviour of carbon nanotubes (CNT) films used in stretchable electronics such as wearable and biomedical technologies seems to have a reasonable impact under cyclic loading, as described by Jin et al. (2018). They discovered that the electrical resistance of CNT thin films under cyclic loading is strain-dependent in a hysteretic manner. It is shown through numerical simulations, theoretical models, and experiments that a microstructural parameter monitors the evolution of hysterical resistance. Slobodian et al. (Slobodian et al. 2011) illustrate that bucky-paper carbon nanotube shows 100% electrical conductivity with maximum applied compressive load and explores its cyclic effects. Even though there are few experimental results on the cyclic response of GDLs, the literature lacks a constitutive model which can be used to predict the in-situ local response under cyclic operating conditions.

A typical diffuser consists of GDL and a thin micro-porous layer (MPL) coated on one of its sides. The GDL is a non-woven composite with randomly distributed carbon fibers reinforced into a highly porous resin matrix (Feser et al. 2006; Gaiselmann et al. 2014; Göbel et al. 2017; Sinha et al. 2007; Slobodian et al. 2013). The MPL constitutes of carbon particles mildly coated with hydrophobic polytetrafluoroethylene (PTFE) (Cindrella et al. 2009; El-Kharouf et al. 2012; Khetabi et al. 2019; Majlan et al. 2018; Zamel et al. 2011). The average thickness of GDL and MPL is around 250µm and 50µm, respectively. Studies have suggested that there is no distinguishable interface between these layers that the MPL non-uniformly intrudes over GDL, especially in the case of SIGRACET SGL GDL (Chen et al. 2022; Hendricks et al. 2020; Zhang et al. 2022a; b). The purpose of having MPL is to improve effective water management in PEM fuel cells (Bosomoiu et al. 2015; Cooper et al. 2017; Fazeli et al. 2016; Patel et al. 2019). The electrical and mass transport properties of GDL as a single entity or GDL and MPL as separate components have been thoroughly understood. However, the mechanical response of these layers for cell operating conditions or fabrication effects are yet to be explored. The compressive cyclic mechanical response of GDLs under standard room conditions is recently reported (Bouziane et al. 2020; Radhakrishnan and Haridoss 2010). Sadeghi et al. (2010) revealed various parameters such as geometric, mechanical, and thermal on GDL's Toray carbon paper. They demonstrated no further changes in the GDL structure after five loading-unloading cycles. Unlike the monotonic response, the cyclic response gives greater insight into the material's characteristics in residual strain, stress softening, and hysteresis evolution. However, the influence of temperature or other effects is not reported in the literature.

The important outcomes of the literature on GDL cyclic compression are briefed as in Table 2.4. Typically, GDLs are not directly placed to fuel cell units. Prior to cell integration, the GDL is subjected to a pre-assembly fabrication process known as hot-press to build an assembly with PEM. The impact of hot-press condition on fuel cell performance and electromechanical stability using the variables involved in hot-press procedure such as temperature (~ 135°C), pressure (~2MPa), and time (in ~ few minutes) is carried as in literature (Bayrakçeken et al. 2008; Hung et al. 2012; Mauger et al. 2021; Shahgaldi et al. 2018a). Although most of the pre-assembly features of GDLs are well-documented, the post-fabrication behaviour has not been thoroughly investigated.

Table 2.4 Effects of GDL cyclic compression

Author	**Outcome/Inferences**
Radhakrishnan and Haridoss (2010)	The impact of cyclic compression on GDL results in irreversible changes in pore size and electrical resistance. Nevertheless, the article fails to explain the reversible behaviour of GDL in terms of electrical resistance.
Sadeghi et al. (2010)	Different values of GDL's Toray carbon paper such as geometric, mechanical, and thermal parameters reach a steady state after five loading-unloading cycles leading to no further changes.
Gigos et al. (2015)	Revealed that under high number of cyclic loads, the behavior of GDL approaches a steady state after 5-6 cycles.
Todd et al. (2016)	The through-plane resistivity decreases with cyclic compression while in-plane resistivity increases.
Jin et al. (2018)	The electrical resistance of CNT thin films under cyclic loading experiences a hysteretic reliance on the strain. It is demonstrated that the evolution of hysterical resistance is monitored by a microstructural parameter.

2.5 GDL electrical/flow heterogeneity on PEFC performance

Several researches have been conducted to explore the performance of PEFC with GDL as a homogeneous and heterogeneous material. To comprehend the impacts of GDL heterogeneity and its impact on neighbouring components, structural integrity and durability studies are carried out (such as membrane and catalyst layers) in PEFC (Peng et al. 2016; Poornesh et al. 2010a; b; c). Wang et al. (2016) showed that heterogeneous compression has an adverse effect on the concentration of reactants and cell performance. However, they illustrated that better performance can be achieved by applying optimum clamping force. Chen et al. (2021) performed a 2D numerical study considering heterogeneous GDL. Their findings indicated that adjusting a number of factors, including porosity, effective electrical conductivity, and effective gas diffusion coefficient, can result in improved cell performance. Hottinen et al. (2007) compared the effects of both homogeneous and heterogeneous GDL on mass and charge transfer in PEFC. Their findings demonstrated that heterogeneous GDL greatly impacts the local current density due to changing interfacial contact resistance, affecting the cell's performance. Yan et al. (2020) evaluated heterogeneous compression of GDL helps in thermal management. Thus, decreasing the average temperature at the cathode catalyst layer and lowering the maximum temperature to avoid local hotspots. Padavu et al. (2021) illustrated the effects of heterogeneous GDL in depth-dependent flow channels. Their results indicated that heterogeneous GDL has a little lower performance than homogeneous GDL, which may be attributable to a more efficient hydrogen oxidation reaction and a decreased oxygen reduction reaction. Nitta et al. (Nitta et al. 2007) too revealed that heterogeneous compression of GDL results in a significant local variation of mass and charge transport.

It is essential to evaluate the effects of ICR on transport phenomena, as it affects the operational voltage of the fuel cell. To this end, Wang et al. (2017a) showed that in order to obtain an optimized cell performance, lower ICR is to be considered since higher ICR results in blocking the electron transfer. Vikram et al. (2016) studied the impact of ICR under heterogeneous GDL conditions. Nearly two-thirds of the ohmic losses in fuel cells exhibited a nonlinear distribution when considering the ICR at the GDL|BPP interface, as evidenced by their findings. Shinde and Koorata (2021) investigated non-uniform ICR based on different clamping configurations. The results suggested that improved clamping designs aid in obtaining uniform electrical properties, which aids in improving fuel cell performance. Akiki et al. (2012) showed that local varying fields of GDL porosity and permeability result in varying ICR deducing the polarization curves. Zhou et al. (2006) illustrated that uniform contact pressure distribution leads to minimum ICR, which is necessary to optimize the fuel cell unit.

Table 2.5 Effects of GDL electrical/flow heterogeneity on PEFC performance

Author	**Outcome/Inferences**
Wang et al. (2016)	Heterogeneous compression has an adverse effect on the concentration of reactants and cell performance. However, it is illustrated that better performance can be achieved by applying optimum clamping force.
Hottinen et al. (2007)	The effects of both homogeneous and heterogeneous GDL on mass and charge transfer in PEFC. Findings demonstrated that heterogeneous GDL greatly impacts the local current density due to changing interfacial contact resistance, affecting the cell's performance.
Yan et al. (2020)	The heterogeneous compression of GDL helps in thermal management. It thus decreases the average temperature at the cathode catalyst layer and lowering the maximum temperature to avoid local hotspots.
Padavu et al. (2021)	Studied the effects of heterogeneous GDL in depth-dependent flow channels. Results indicates the heterogeneous GDL has a little lower performance than homogeneous GDL, which may be attributable to a more efficient hydrogen oxidation reaction and a decreased oxygen reduction reaction.
Wang et al. (2017a)	To obtain an optimized cell performance, lower ICR is to be considered since higher ICR results in blocking the electron transfer.
Akiki et al. (2012)	The local varying fields of GDL porosity and permeability result in varying ICR deducing the polarization curves.
Zhou et al. (2006)	Uniform contact pressure distribution leads to minimum ICR, which is necessary to optimize the fuel cell unit.

From the above brief review and also from Table 2.5, it is clear that it is more practical to visualise GDL as heterogeneous material (electrical and flow properties) in the numerical domain.

2.6 Relative humidity effects on PEFC performance

Relative humidity (RH) plays a major role in PEFC performance, whose direct impact can be seen on membrane conductivity (Zhang et al. 2008). A good number of studies have been carried out on relative humidity, considering various combinations of RH both at the anode and cathode of the PEM fuel cell (Emmanuel et al. 2018; Xia et al. 2022; Xing et al. 2016). Few studies, such as Emmanuel et al. (2018), revealed that higher RH at the anode helps increase the performance of fuel cells, whereas, at higher current density, lower RH at the cathode is recommended to enhance the PEMFC performance. A numerical study on the effects of RH by Xing et al. (2016) showed that fully humidified anode gas is necessary to attain membrane hydration. In contrast, optimal cathode humidity depends on anode RH, channel length and current density. Zhou et al. (2009) studied the influence of higher temperature and relative humidity on PEMFC, resulting in non-uniform GDL compression and reduction in contact resistance. Zhou and Wu (2007) demonstrated numerically that effects of heterogeneous compression is higher at higher RH leading to lower performance.

Table 2.6 Effects of relative humidity effects on PEFC performance

Author	**Outcome/Inferences**
Emmanuel et al. (2018)	The higher RH at the anode helps increase the performance of fuel cells, whereas, at higher current density, lower RH at the cathode is recommended to enhance the PEMFC performance.
Xing et al. (2016)	Fully humidified anode gas is necessary to attain membrane hydration.
Zhou et al. (2009)	The influence of higher temperature and relative humidity on PEMFC results in non-uniform GDL compression and reduction in contact resistance.
Zhou and Wu (2007)	Numerically assessed that effects of heterogeneous compression is higher at higher RH leading to lower performance.

From the preceding discussion on electrical/flow heterogeneities and variation in relative humidity from Table 2.5 & 2.6, it is evident that numerical studies on the combined influence of electrical/flow heterogeneities and inlet RH on the performance of PEFCs are limited.

2.7 GDL Material Models

GDL comprises highly porous carbon fibre-based materials, including carbon paper, carbon cloth, and carbon felt (Qiu et al. 2018; Rofaiel et al. 2012). GDL is commonly regarded as an isotropic linearly elastic material for structural simulations of PEFC models (Alizadeh et al. 2016, 2017; Chien et al. 2016). In practice, however, GDL is a highly compressible material. Thus, typical linear elastic models may not accurately describe the actual response; consequently, it is reasonable to view its response as nonlinear material (Gigos et al. 2015; Mishra et al. 2004; Norouzifard and Bahrami 2014a). Thus, GDL material should be modeled as a compressible form of the hyperelastic model. The GDLs can be modeled as a compressible hyperelastic material for numerical analysis using various strain energy forms, where the material characteristics are derived from experimental data on uniaxial compression (Fly et al. 2018, 2019; Ismail et al. 2012; Suvorov et al. 2008). Hence to depict the actual GDL behaviour in carrying structural analysis, it becomes necessary to consider it a compressible hyperelastic material.

2.8 Conclusions from Literature Review

To enhance the performance of the PEM fuel cell, it is essential to understand the mechanical and electrical properties of the GDL. Compression of the GDL due to clamping forces significantly impacts these properties.

Although numerous experimental techniques of endplate designs provide a suitable answer to the problem of non-uniform contact pressure, these techniques are time-consuming and not cost-effective. Using an inaccurate numerical approach, material models do not mimic the practical response of the relevant components. In order to emphasise these limitations, work with respect to the sensitivity of several endplate designs and GDL material models to quantify interface contact pressure, interface contact resistance, and bulk transport parameters, as well as their uniformity, needs to be carried out. Moreover, it is evident that numerical studies on the combined influence of GDL electrical/flow heterogeneities and variation in inlet relative humidity to gain insight into the performance characteristics are limited. The performance of PEM fuel cells with a larger active area and GDL heterogeneity needs to be further investigated with the considered different endplate configurations. GDLs undergo pre-assembly hot press pressure and in-situ micro-cyclic loadings induced by cell operating conditions (start-up/shutdown or hygrothermal cycle). As the durability of this layer is directly related to its structural resilience, it is highly desirable to investigate the structural response under situations comparable to cell operation. An accurate description of pre-assembly fabrication effect is unknown due to limitations on experimental data. Consequently, it is necessary to study experimental schemes for analysing the response of GDL (with and without MPL) at different temperatures, as well as the pre-assembly hot-press effect. Even though there are few experimental data on the cyclic response of GDLs, the literature lacks a constitutive model that can be utilised to predict the in-situ local reaction under cyclic operation conditions. The constitutive model that can predict the cyclic ohmic response of GDLs under repetitive compressive loading is currently unavailable and must be developed.

The following list of research objectives is compiled based on the initial review of the available literature and consequent research gaps.

2.9 Research Objectives

The main objectives of the present research work are:

1. To investigate the material heterogeneity of the GDL on the flow and transport properties under different endplate design configurations.
2. To study the impact of electrical and flow inhomogeneity of GDL on PEFC performance under varying inlet humidity conditions.
3. Computational analysis of 25cm^2 active area PEFC with heterogeneous GDL.
4. Cyclic mechanical response of GDLs under pre and post hot-press conditions.
5. To develop a phenomenologically motivated constitutive model to predict cyclic bulk electrical conductivity response of GDL under stress limit.

2.10 Closure

In this chapter, the objectives of the present work are framed based on the research gaps observed from the comprehensive literature survey. The next chapter involves the numerical investigation of two endplate configurations of a single PEFC with different GDL material models in evaluating the mechanical and electrical properties of GDL.

CHAPTER 3

INVESTIGATION OF ENDPLATE DESIGN CONFIGURATIONS AND GDL MATERIAL MODELS

3.1 Introduction

Polymer electrolyte fuel cells (PEFCs) are a promising alternative energy source of the future. A PEFC stack consists of unit cells connected in series. These cells are kept intact with the help of external clamping. As the active area of the stack increases, the design requirements for an efficient clamping mechanism (a mechanism that allows uniform distribution of pressure over the cell's active area) also grow. Random design selection may result in reduced system efficiency amid high maintenance costs. Thus to achieve higher stability with improved performance, it is necessary to have an effective clamping design for the stack (Karvonen et al. 2008; Lin et al. 2011; Qiu et al. 2015; Taymaz and Benli 2010; Wang et al. 2008; Yu et al. 2010).

Although several experimental techniques of endplate designs provide a suitable solution to reduce nonuniformity in contact pressure, these techniques are time intensive and inefficient. An incorrect numerical technique is one in which material models do not replicate the findings established by the relevant components. In order to emphasise these constraints, this work examines the sensitivity of two endplate designs and GDL material models to quantify interface contact pressure, interface contact resistance, and bulk transport properties, as well as their uniformity in the aforementioned interfaces.

3.2 Methodology

A single-cell PEFC is simulated using ABAQUS CAE tool for the structural response. The model and simulation details are given in the following sections.

3.2.1 Description of the design

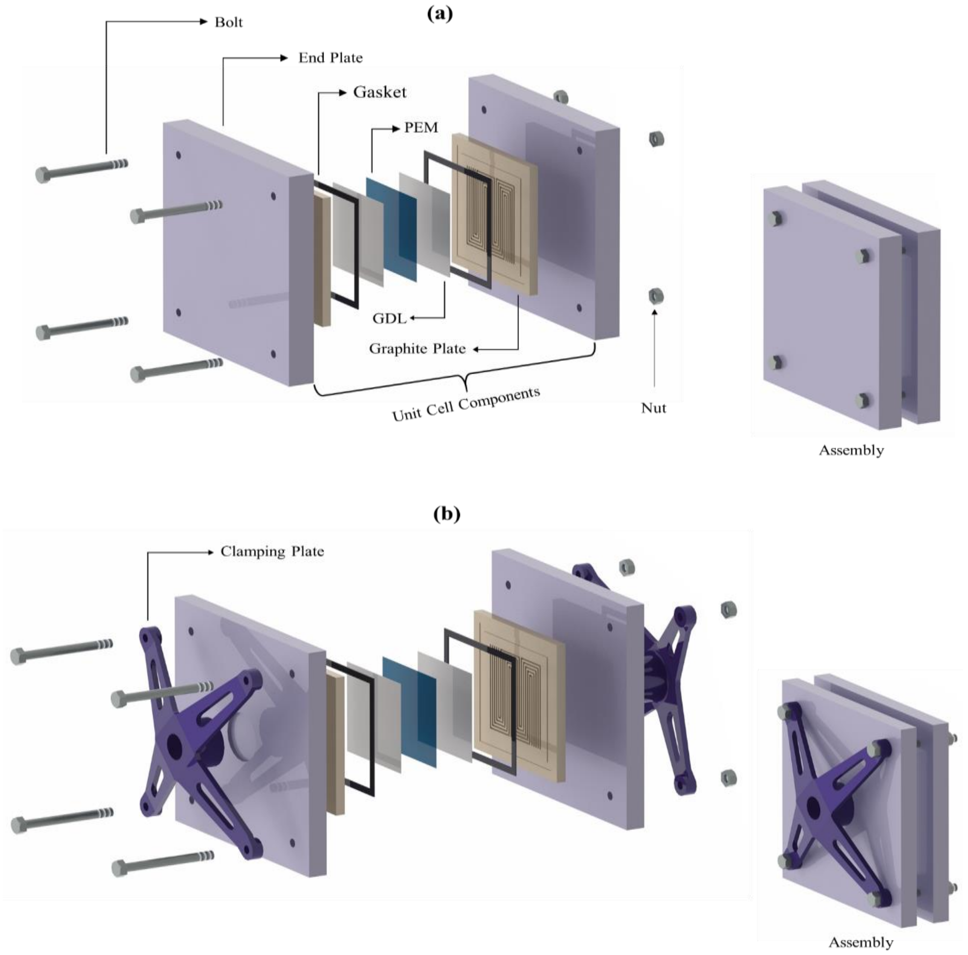
(a)
Bolt
End Plate
Gasket
PEM
GDL
Graphite Plate
Unit Cell Components
Nut
Assembly
(b)
Clamping Plate
Assembly

Figure 3.1 Schematic illustration of (a) Clamping-1; (b) Clamping-2

Figure 3.1(a) shows the C-1 type clamping with a three-dimensional design of a single cell PEFC having a 50 mm x 50 mm active area, and Figure 3.1(b) shows the cell with C-2 type clamping. It can be said that the C-1 design is conventional, and C-2 design is a contemporary improvement over the C-1. The single-cell PEFC CAD model for C-1 and C-2 design is modeled and clamped with four bolts (note that the influence of bolt configuration is already well studied and hence not included in this work). The cell comprises six components, the PEM, GDLs, gaskets, graphite/flow field plates, bolts, and body plate/endplates. However, in the Clamping-2 design, a clamping plate is assembled, as shown in Figure 3.1(b). The flow field plate consists of graphite material having a parallel serpentine flow field.

The geometrical parameters of the PEFC unit cell model are listed in Table 3.1. The material properties of PEFC components considered for numerical simulation are also listed in Table 3.1, which are largely taken from the reference article (Chien et al. 2016). Table 3.1 specifies the Clamping-1 linear elastic constants for GDL. It is noted from the literature that the GDL exhibits large deformation behaviour.

Table 3.1 Geometrical dimensions and material properties of PEFC components

Components	**Materials**	**Young's Modulus, MPa**	**Poisson's Ratio**	**Dimensions, mm**
Bolts	Stainless Steel	200000	0.3	5 mm in Diameter
End Plates	Aluminium	71000	0.33	130 x 130 x 10
Graphite Plate	Graphite	10000	0.25	80 x 80 x 5
Gas Diffusion Layer	Carbon Paper	10	0.25	50 x 50 x 0.28
PEM	Nafion	249	0.25	50 x 50 x 0.05
Gasket	Rubber	16	0.48	68.8 x 68.8 x 0.55, Rib of 3.8 mm width

Hence, it is suitable to choose a hyperelastic strain energy function that can replicate the nonlinearity under large deformation. Here, Yeoh hyperelastic model is chosen since it has higher-order terms that can replicate the nonlinear response without complexity. In general, however, the hyperelastic models are, by default, suitable for incompressible materials. Table 3.2 lists the material constants suitable to model the incompressible (no volume change) form of GDL material. The material constants are obtained using ABAQUS curve-fitting of the literature experimental data stated in the reference article (Norouzifard and Bahrami 2014b). Nevertheless, the GDL materials are highly porous and hence highly compressible. For this reason, the same hyperelastic model is treated as in the compressible form by not neglecting the volumetric term in the strain energy equation. The strain energy function for Yeoh hyperelastic model is given below:

$$W=\sum_{i=1}^{3}C_{i0}\left(\bar{I}_{i}-3\right)^{i}+\sum_{i=1}^{3}\frac{1}{D_{i}}\ J_{el}-1^{\ 2i} \qquad 3.1$$

where C_{i0} and D_i are material parameters related to the shear modulus and bulk modulus, respectively. The C_{i0} material parameter is employed to control the shear behaviour, which can be ascertained from uniaxial, biaxial and planar tests. The D_i material parameter is used to control the bulk compressibility, which is set to zero for incompressible material and non-zero for compressible material.

Table 3.2 Incompressible hyperelastic material constants for GDL model

Material Constants	**Value**	**Unit**	**Source**
C_{10}	0.05447	MPa	The constants are obtained using model-fit for the experimental data disclosed in the ref (Norouzifard and Bahrami 2014b)
C_{20}	2.087	MPa	
C_{30}	6.8945	MPa	

The material constants for a compressible form of the model are listed in Table 3. The material constants are readily determined using ABAQUS curve-fitting of the literature experimental data stated in the reference article (Norouzifard and Bahrami 2014b).

Table 3.3 Compressible hyperelastic material constants for GDL model

Material Constants	**Value**	**Unit**	**Source**
C_{10}	0.05447	MPa	The constants are obtained using model-fit for the experimental data disclosed in the ref (Norouzifard and Bahrami 2014b)
C_{20}	2.087	MPa	
C_{30}	6.8945	MPa	
D_1	0.18358	(1/MPa)	
D_2	0.00479	(1/MPa)	
D_3	0.0007252	(1/MPa)	

Figure 3.1(b) also depicts the clamping plate design where a characteristic central mass is added to exert pressure at the centre. This nearly matches the pressure exerted by the bolts at the edges. In the Clamping-2 design, the endplate has 10 mm thickness, whereas in the Clamping-1 design, it is assumed as 15 mm. The circular masses at the corners of the clamping plate in which the bolts are assembled are 6 mm in height, 12 mm outer diameter, and 5 mm inner diameter. The rib connecting between corner masses and the centre mass is of 3 mm thickness. The centre spacing between each bolt is 98 mm. The flow field's configuration plays a vital role in the design of the flow field as it affects the distribution of reactants. The flow field plate has a serpentine flow field and is considered to be of graphite material (Su et al. 2005; Wilkinson and Vanderleeden 2010). Its dimensions are 1 mm in width, 1 mm in channel depth, and 1 mm in land width.

Several studies report on the relationship between contact resistance and bulk resistance of GDL in the literature (Liang et al. 2018; Qiu et al. 2017; Tanaka et al. 2016; Vikram et al. 2016; Ye et al. 2014). As the compression pressure rises, there is indeed a change in contact resistance at BPP|GDL interface and GDL’s bulk resistance. However, one should note that the observations made in these studies are limited to globalized or overall variation in the properties and hence do not comprehensively understand the localized variation. Nevertheless, investigating interfacial contact resistance is vital as it results in loss of operational voltage, which, in turn, reduces the performance of PEM fuel cells. In the present study, a numerical simulation is adopted to obtain contact pressure at the interface of BPP|GDL and GDL|PEM. The contact pressure obtained can be used to extract interfacial contact resistance at BPP|GDL. This is achieved using the nonlinear relationship response given by (Zhou et al. 2006):

$$ICR = A\left(\frac{B}{p}\right)^{C} \qquad 3.2$$

where ICR is the interfacial contact resistance, p is contact pressure obtained at the interface of BPP|GDL, and A, B, and C are parameters obtained using curve fitting with experimental results (Mishra et al. 2004; Vikram et al. 2016). These parameters (A, B, and *C)* are related to the tip's roughness of BPP, which comes in contact with the GDL component.

Further bulk resistance in the GDL component is accessed by extracting local deformation of the GDL component along the through-plane direction. It is reported that the thickness and porosity of the GDL sample decrease with the applied compression load (Mishra et al. 2004). The relationship to achieve bulk resistance under compression is defined by the equation (García-Salaberri et al. 2011; Mishra et al. 2004)

$$R_b = \frac{\rho_f d^2}{d_o \; 1 - \phi_o} \qquad 3.3$$

where R_b is the bulk resistance of the GDL, ρ_f is the resistivity of carbon fibre, i.e., 4.05 x 10^{-5} Ωm (Ozden et al. 2019), ϕ_o is the initial porosity of GDL (80%), d_o and d are the local thickness of GDL before and after compression, respectively.

GDL compression decreases gas permeability, resulting in a loss of ohmic overpotential and an increase in mass transport resistance (Yim et al. 2010). GDL permeability and diffusion of reactant gas have been shown to be impaired by clamping force due to GDL deformation and porosity (Wen et al. 2009). The through-plane deformation of the GDL component can be utilized to acquire local permeability variation where deformation is obtained using the relationship (Akiki et al. 2012)

$$e = \frac{d}{d_o} \qquad 3.4$$

where e is the local deformation of the GDL. Thus porosity is given by (Akiki et al. 2012; Cindrella et al. 2009):

$$\phi = \frac{\phi_o + e}{1 + e} \qquad 3.5$$

where ϕ is the GDL porosity after compression

Using the GDL porosity, where porosity varies along the surface of the GDL component, permeability K can be estimated by the Blake-Kozeny equation as described below (Wang and Chen 2011)

$$K = \frac{D_p^2}{150} \frac{\phi^3}{{1-\phi}^{2}} \qquad 3.6$$

where D_p is the pore dimension with average pore size ranging from 10-30µm; it is presumed as 10 µm in the present case.

3.2.2 Single-Cell Model

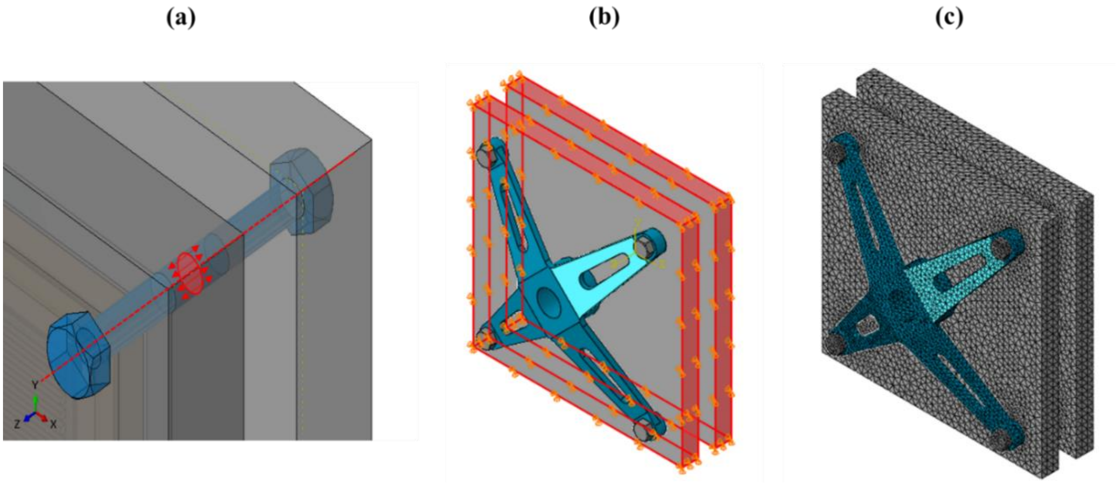

Figure 3.2 Shows (a) bolt loading conditions; (b) boundary conditions; and (c) meshed model

Figure 3.2(a) shows the bolt loads assigned along the line of action. Each bolt is applied with 500 N. Both designs are assigned the same boundary conditions, as shown in Figure 3.2(b), where the selected surfaces are constrained in the x and y directions. All the components interface is assigned with a low coefficient of friction. The meshed model is, as shown in Figure 3.2(c).

3.3 Results and Discussion

3.3.1 Interfacial contact pressure and contact resistance distribution

Figure 3.3 shows the contact pressure distribution contours on the GDL for a Clamping-1 (C-1) and Clamping-2 (C-2) design. In Figure 3.3(a), the GDL is taken as a linear elastic material. It is observed that the contact pressure distribution is significantly lower in the central region for the C-1 design, and the magnitude increases towards the edge/perimeter of the component. The contact pressure is more at the edges because of bolts clamping is on the edges. In contrast, the model has no force or clamping available in the central zone. The magnitude of difference in contact pressure distribution is 1.373 MPa, which results in non-uniformity in the C-1 design. However, C-2 design exhibits better uniformity and contact pressure distribution.

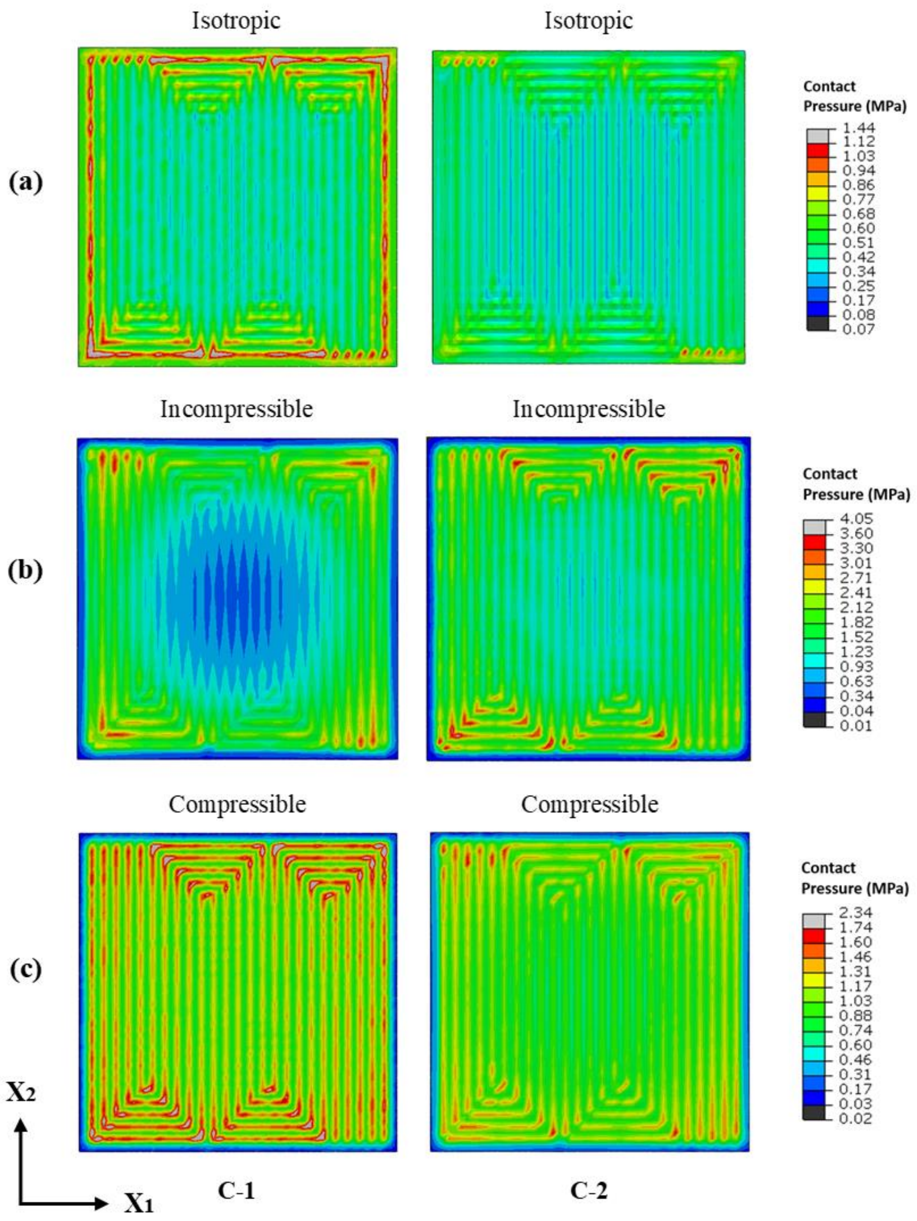

Figure 3.3 The contact pressure distribution contours at the interface of BPP|GDL for (a) GDL as Isotropic; (b) GDL as incompressible hyperelastic; and (c) GDL as compressible hyperelastic model

The magnitude of the difference in contact pressure is 0.873 MPa. This is due to the influence of a clamping plate, which exerts compressive pressure at the central zone of the PEFCs components. Figure 3.3(b) shows the contact pressure contours for BPP|GDL modeled as an incompressible (a model where volume change is neglected) hyperelastic material. It is observed for the C-1 design that contact pressure is almost non-existent near the central zone, and it steadily increases from the center to the edge of the GDL.

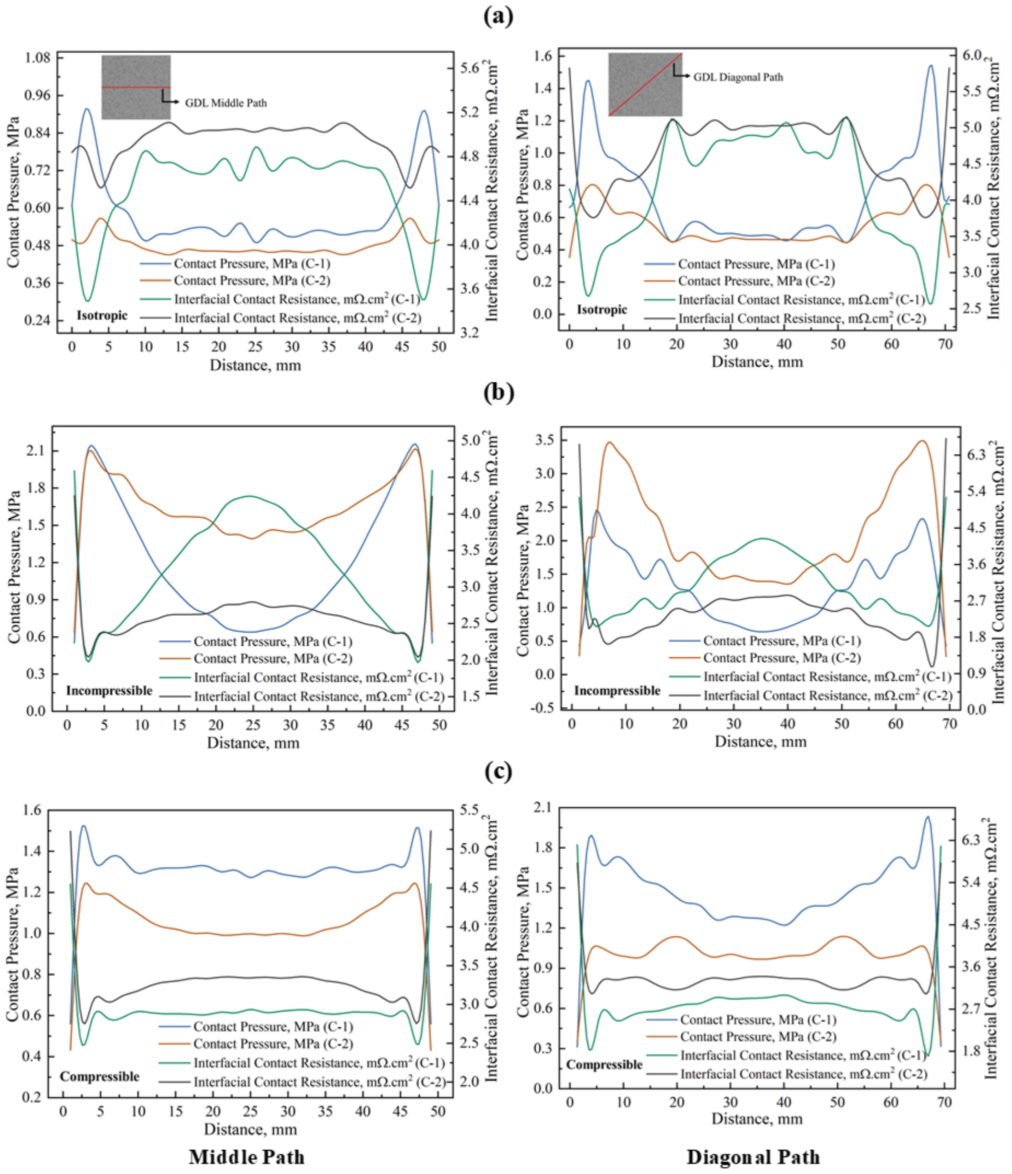

Figure 3.4 The line plots of contact pressure distribution and interfacial contact resistance at the interface of BPP|GDL for (a) GDL as Isotropic; (b) GDL as incompressible hyperelastic; and (c) GDL as a compressible hyperelastic model.

Therefore, it expresses non-uniformity and poor contact pressure distribution with the magnitude of difference in contact pressure 3.261 MPa. However, in this case, C-2 design has non-zero contact pressure in the central zone. Nevertheless, it is observed to exhibit non-uniformity with contact pressure distribution values exceeding the C-1 design. It has a magnitude of difference in contact pressure of 4.044 MPa.

When the GDL material is modeled as a more realistic compressible hyperelastic material, contact pressure distribution contours are shown in Figure 3.3(c). The magnitude of difference in contact pressure distribution is 2.321 MPa for the C-1 design. For the C-2 design, the magnitude of the difference in contact pressure is 1.622 MPa and is near uniform. It is broadly understood from the contours in Figure 3.3 that the C-2 design attributes to better pressure distribution uniformity. Simultaneously, the material model also plays a role in accurately quantifying the difference in magnitudes.

A relationship between contact pressure and interface contact resistance is plotted in Figure 3.4. Figure 3.4 shows the line distribution of contact pressure distribution and interface contact resistance along the middle and the diagonal path of the BPP|GDL interface. Figure 3.4(a) depicts a non-uniformity in contact pressure distribution for C-1 design, whereas an improved uniformity in contact pressure for the C-2 design. Figure 3.4(a) clearly illustrates that the contact pressure in C-2 is lower yet more uniform, implying uniform interfacial contact resistance compared to the C-1 case. For GDL as an incompressible model, Figure 3.4(b) shows highly non-uniform distribution of pressure in both the C-2 and C-1 cases. This trend is also observed when the data is extracted in the diagonal path, as noted from Figure 3.4(b). The GDL material model may have led to these discrepancies. Figure 3.4(c) reflects the C-2 design's effectiveness in achieving better uniformity and proper contact pressure distribution than the C-1 design. The slope change of curves for the C-2 design is almost equal to zero. The compressible hyperelastic material model is believed to be a realistic representation of the undergoing deformation in GDLs and displays a more practical contact pressure distribution.

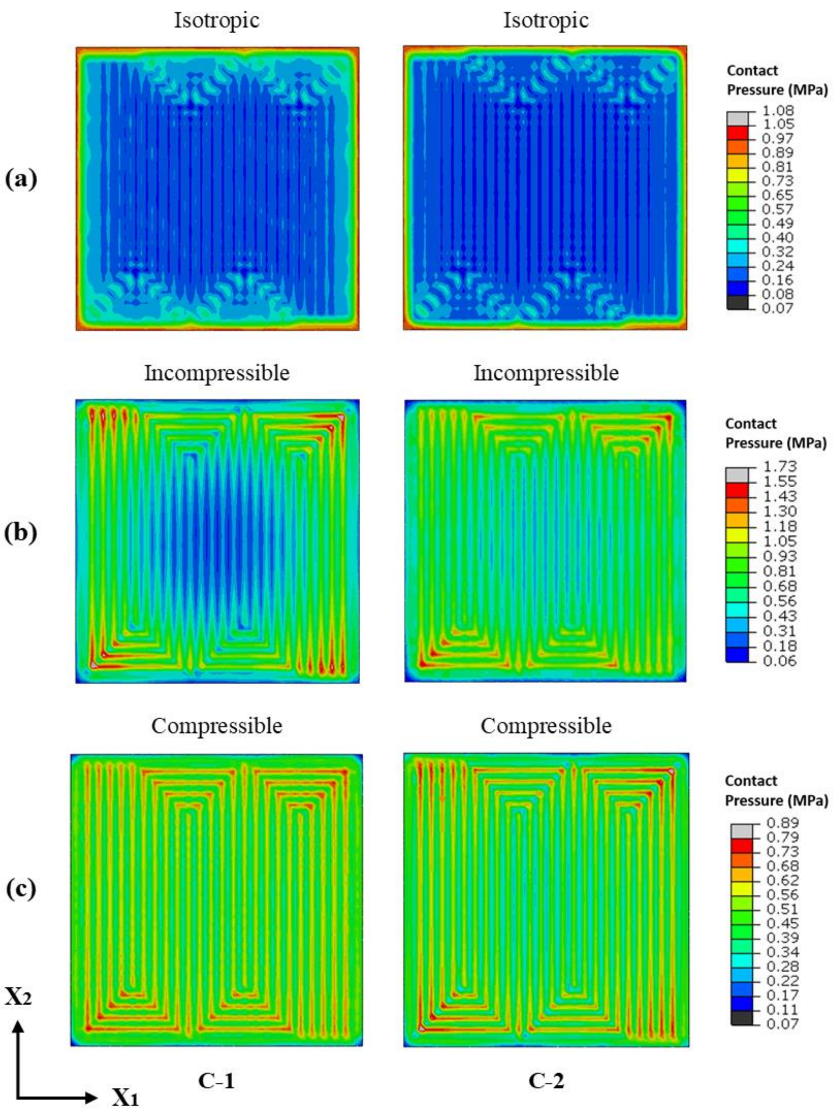

Figure 3.5 The contact pressure distribution contours at the interface of GDL|PEM for (a) GDL as Isotropic; (b) GDL as incompressible hyperelastic; and (c) GDL as compressible hyperelastic model

Figure 3.5 shows the contact pressure distribution in the GDL|PEM interface for C-1 and C-2 designs. Here, the contact pressure on PEM in the C-2 design is more uniform than the C-1 design. With GDL as a linear elastic material, Figure 3.5(a) presents the contact pressure distribution contours in GDL|PEM interface. The difference in contact pressure is around 1 MPa with the C-1 design and 0.8 MPa with the C-2 design. Figure 3.5(b) shows the contact pressure contours in the GDL|PEM interface when GDL is regarded as incompressible hyperelastic material. For the C-1 design, the contact pressure contours near the central zone are almost absent. They are steadily increasing from the center to the edge of the PEM. With the magnitude of difference 1.67 MPa, it thus reflects non-uniformity and unevenness in contact pressure distribution. However, in the case of the C-2 design, it is seen that the magnitude of the difference in contact pressure distribution is 1.24 MPa. It has non-zero contact pressure at the central zone. Nevertheless, it is noticed that the chosen material model results in non-uniform contact pressure distribution. Modeling GDL material as a more practical, compressible hyperelastic material, the contact pressure distribution contours at the interface of GDL|PEM are shown in Figure 3.5(c). It is noticed that the magnitude of the difference in contact pressure distribution is 0.817 MPa, which results in non-uniformity. Whereas, in the case of the C-2 design, it exhibits an improvement in uniformity with the magnitude of difference in contact pressure at 0.559 MPa.

For a more comprehensive view, line measurements are performed to interpret the contact pressure distribution. Figure 3.6 provides the graphical distribution of contact pressure distribution along both the middle and diagonal paths of the GDL|PEM interface. GDL, when treated as a linear elastic material, the line plot is as shown in Figure 3.6(a). It presents the nonuniform behaviour at GDL|PEM interface in a C-1 design. At the same time, it shows better uniformity and consistent contact pressure in the C-2 design. The line plot in Figure 3.6(b) demonstrates that the incompressible GDL hyperelastic case provides a highly nonuniform pressure distribution at the GDL|PEM interface. Therefore, it is assumed that the incompressible model is not optimal for understanding the distribution of contact pressure at the interfaces. Further, when the GDL is modeled as compressible hyperelastic material (model where the volume changes), the line plot is described in Figure 3.6(c). It signifies that the C-2 design results in better uniformity and proper contact pressure distribution than the C-1 design. The contour plots and line plots outlined above make it quite clear that the C-2 clamping design results in improved uniformity and evenness at both BPP|GDL, and GDL|PEM interfaces. The line plots offer a concise overview of which interface region is under intense pressure. The abrupt jumps in line plots near both interfaces are primarily due to the bolt assembly. Since GDL is a highly porous material evaluating it as linear elastic material in PEFC is not highly advisable; therefore, it is vital to analyze it as nonlinear. When the GDL is modeled as the incompressible, high and non-uniform slope is observed. In contrast, for the compressible hyperelastic material, it is relatively low and almost uniform. It is also projected that the C-2 design would provide a 30% improvement in contact pressure compared to the C-1 design when GDL is treated as a compressible hyperelastic material.

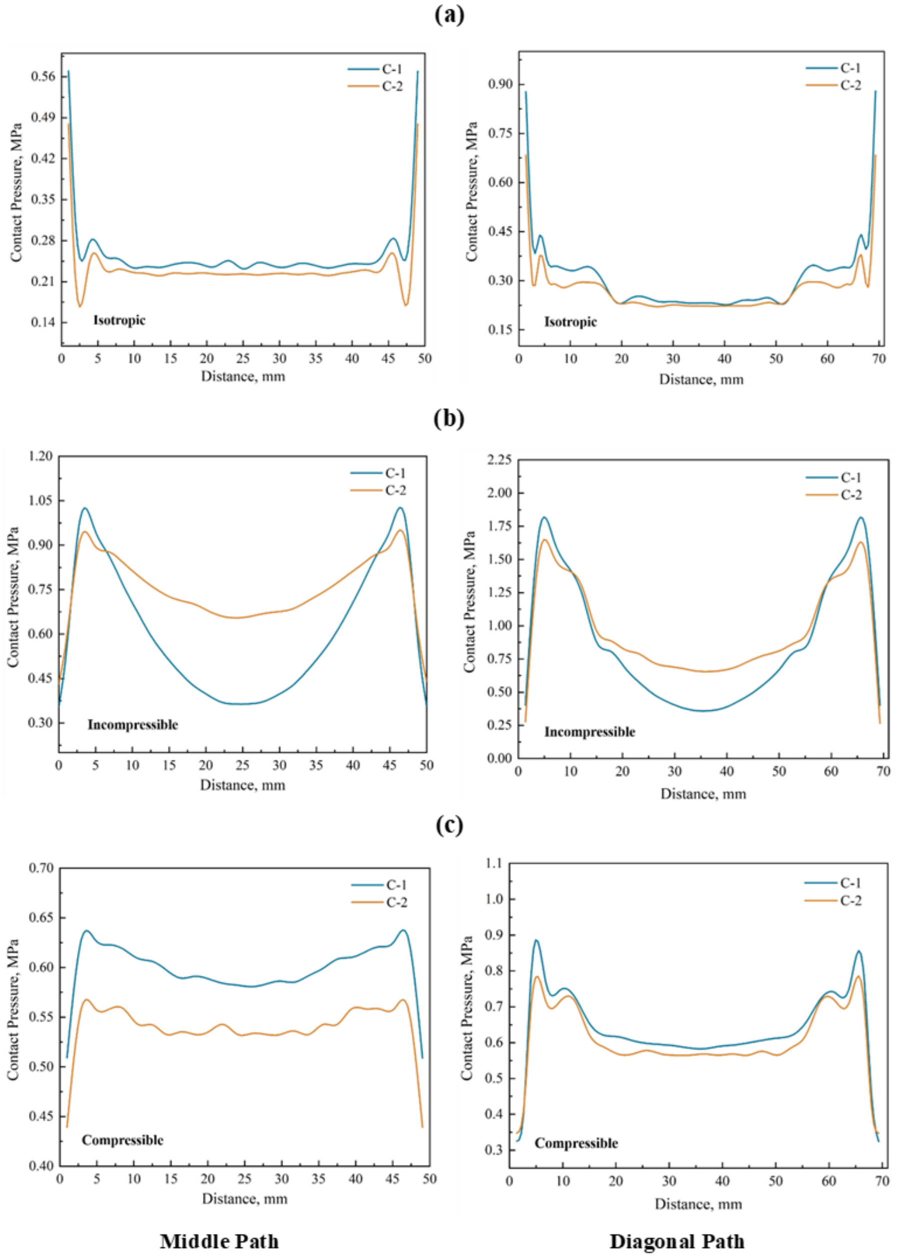

Figure 3.6 The line plots of contact pressure distribution at the interface of GDL|PEM for (a) GDL as Isotropic; (b) GDL as incompressible hyperelastic; and (c) GDL as compressible hyperelastic model

3.3.2 Equivalent stress distribution

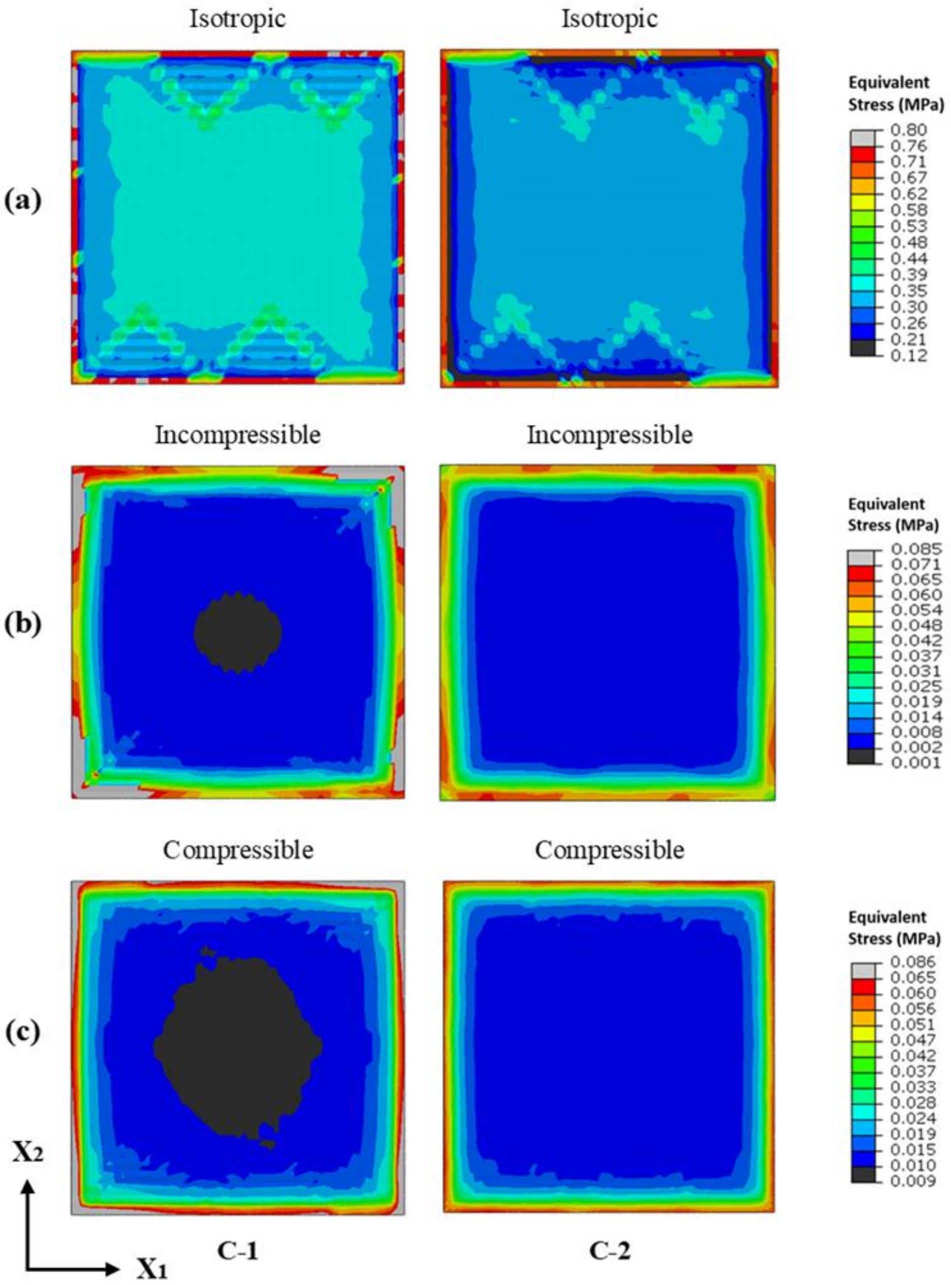

Figure 3.7 The equivalent stress distribution contours for GDL with (a) GDL as Isotropic; (b) GDL as incompressible hyperelastic; and (c) GDL as compressible hyperelastic model

The equivalent stress distribution contours on GDL are shown in Figure 3.7 for both designs. Figure 3.7(a) presents the stress contours when GDL is taken as a linear elastic material. It is observed that the GDL tolerates maximum stresses at the edges; this phenomenon is due to the clamping system and bolt design. In a C-1 design, the equivalent stress distribution formed in the active area is about 0.43 MPa. In comparison, the C-2 design is approximately 0.3 MPa, which is lower than the C-1 design. Therefore, it implies that the C-2 design experiences lower values of equivalent stress in the active area than the C-1 design. The C-1 design bears a magnitude of a difference of 0.584 MPa, whereas it is 0.634 MPa in the C-2 design. Now that GDL is chosen to be an incompressible hyperelastic material, the stress contours are shown in Figure 3.7(b). The difference in stress distribution is 0.083 MPa in C-1 design and 0.064 MPa in the C-2 design. From both design results, it can be inferred that there is visibly no difference in stress contours, except at the middle portion in C-1 design where stress formation is lowest. As a result, GDL assumed as the incompressible hyperelastic model needs to be avoided. In the practical case where GDL is taken as a compressible hyperelastic model, the stress behavior is shown in Figure 3.7(c). The magnitude of difference in stress distribution is 0.075 MPa for C-1 design, as opposed to 0.055 MPa for the C-2 design. It is also noted here that the central portion of the active area bears the lowest equivalent stress distribution in C-1 design compared to the C-2 design, where there is no such lowest stress area at the center.

Figure 3.8 shows the contour distribution of mises stress distribution in PEM. One can observe from Figure 3.8(a) that there is no much difference in stress for the isotropic GDL material model. That is, in a C-1 design, the magnitude of difference in stress is 2.745 MPa. In a C-2 design, it is 2.836 MPa. In contrast, Figure 3.8(b) shows significant differences in the models where GDL is in incompressible form. The impact of different end plate designs is visible with a C-1 design clamping case showing the nonuniform distribution of stresses with stress as low as 0.181 MPa at the central regime. Both of the above GDL models show conflicting results. Moreover, the stress magnitudes are higher in the latter case due to the incompressibility of GDL. When the GDL is modeled in its most effective form, i.e., in the compressible form, the overall stress reduces, as shown in Figure 3.8(c). The stress difference for the PEM is 2.6 MPa in the C-1 case with nonuniform distribution as opposed to 1.93 MPa for the C-2 design with uniform distribution.

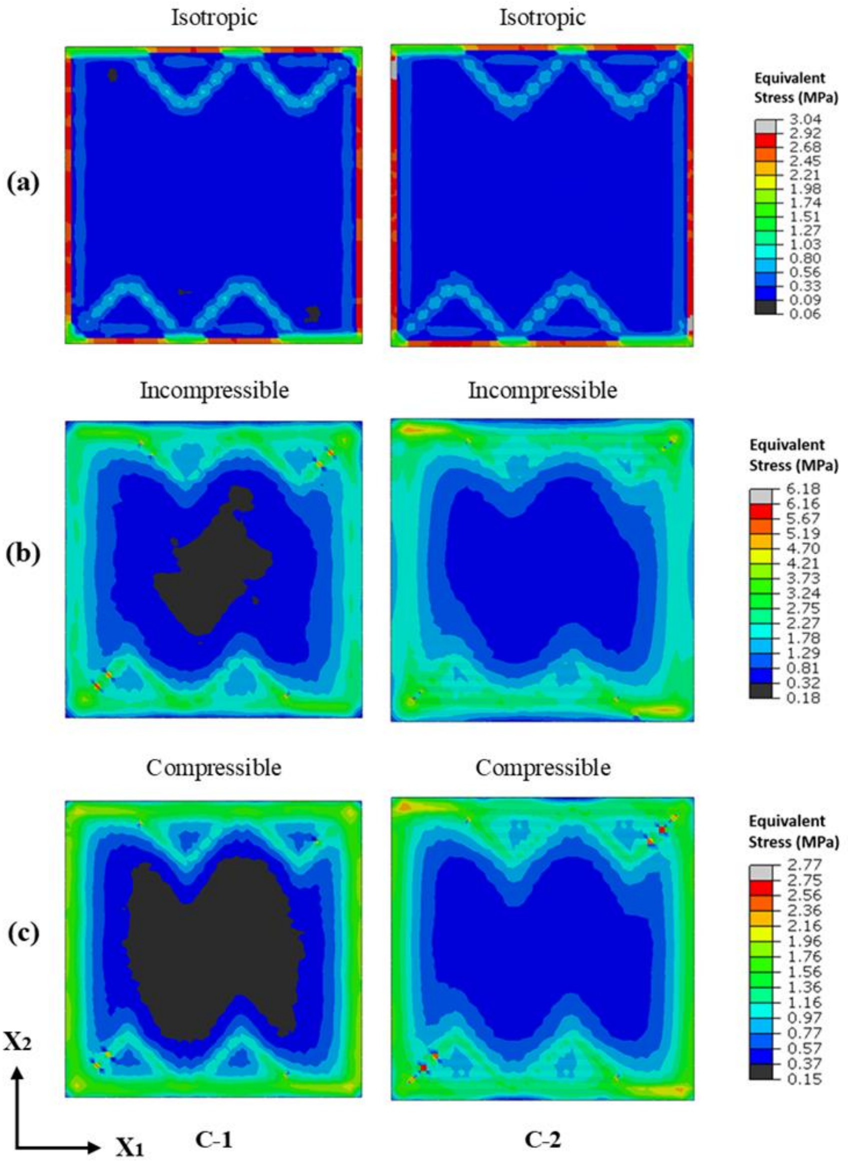

Figure 3.8 The equivalent stress distribution contours for PEM with (a) GDL as Isotropic; (b) GDL as incompressible hyperelastic; and (c) GDL as compressible hyperelastic model

3.3.3 Hydrostatic pressure distribution

Next, hydrostatic pressure σ_h contours of PEM are plotted provided in Figure 3.9. The σ_h is vital to assess the damage initiation or pinhole formation in PEMs that eventually leads to the component's premature failure. As observed in Figure 3.9(a), the isotropic GDL case shows no significant variation in the clamping cases. It is also observed that there is no buildup of negative pressure. In contrast, as in Figure 3.9(b), the nonlinear incompressible GDL model shows differences in pressure in both cases. The impact of clamping designs on the PEMs is visible. Here, the negative pressure in PEMs is observed surrounding the active area. The negative pressure is tensile, which tends to stretch the membrane. The difference in pressure in the C-1 clamping design is relatively high (-1.275 to +1.109 MPa), similar to the C-2 clamping case (-1.78 to +0.4 MPa). Interestingly, the negative pressure observed in the C-2 clamping design is much higher at -1.78 MPa, which is considered not acceptable. However, the negative value is observed near the edges outside the active area directly under the bolt area. Thus this could be alleviated by adopting a better bolt design strategy. Nevertheless, the difference in magnitude of pressure seems on the higher end. Thus Figure 3.9(c) is plotted where the GDL is in the compressible form. One can observe that the pressure level is significantly reduced with a variation from -0.9MPa to 0.33MPa. It is clear from Figure 3.9 that the distribution is nonuniform in C-1 clamping, which is overcome by a C-2 mechanism.

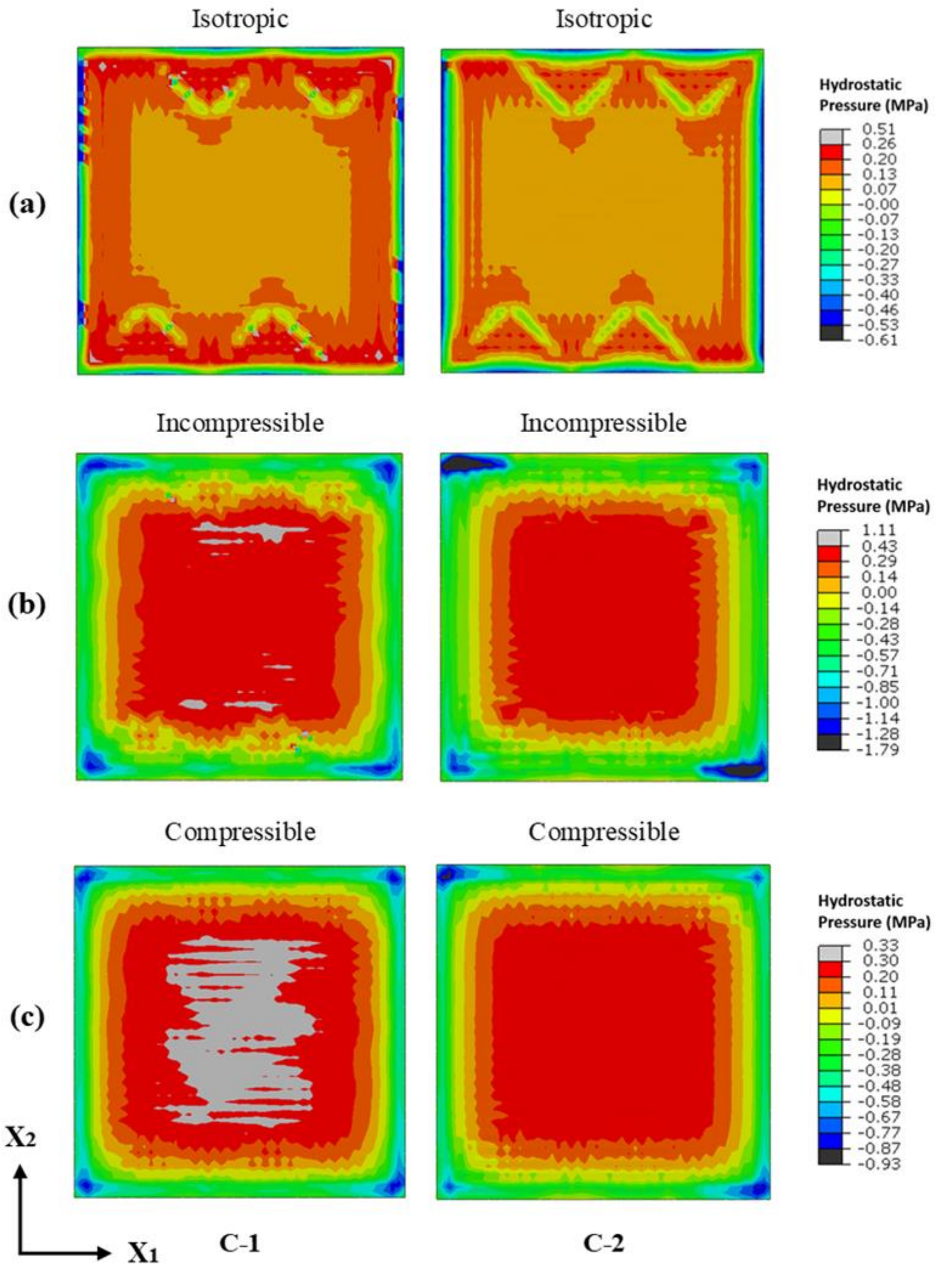

Figure 3.9 The Hydrostatic pressure distribution contours for PEM with (a) GDL as Isotropic; (b) GDL as incompressible hyperelastic; and (c) GDL as compressible hyperelastic model

3.3.4 Through-plane deformation

The deformation of GDLs in the through-plane direction (along the bolt loading direction) is shown in Figure 3.10. The contour plots are obtained by taking the cross-sectional plane at the middle of the GDL. It is observed that the GDL with an isotropic model exhibits the maximum tensile deformation near the channel vicinity regardless of the clamping type design utilised (Figure 3.10(a)). Moreover, this model cannot replicate the consolidation effect generally observed in the porous materials (at a given vicinity, the value of deformation from top surface to the bottom surface is almost the same here). As shown in Figure 3.10(b), the incompressible version of the hyperelastic GDL material model overcomes this issue; however, the model is not able to accommodate volume change. For this reason, the negative deformation is less compared to the previous case. The compressive alternative depicts (Figure 3.10(c)) both negative and positive deformation with the consolidation effect (graded effect). It further shows that at a given vicinity, the value of deformation from top to bottom surface varies and exhibits a differential deformation (tensile to compressive).

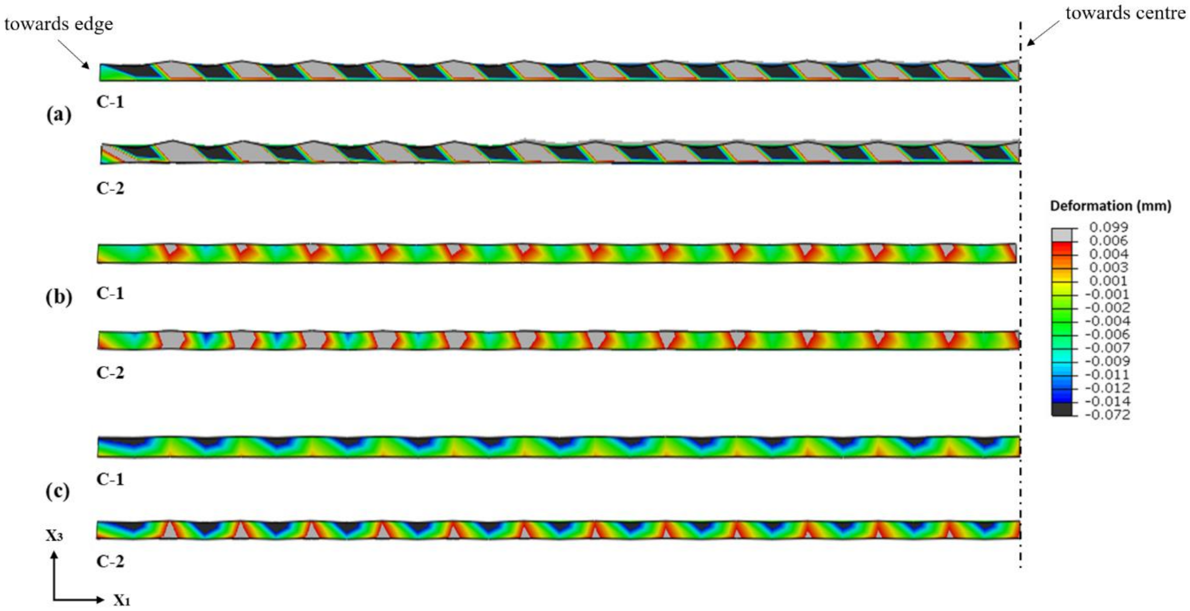

Figure 3.10 The cross-sections showing differences in through-plane deformation (U3) in GDLs with (a) linear elastic isotropic; (b) incompressible hyperelastic; and (c) compressible hyperelastic GDL material models for (1) C-1; and (2) C-2

3.3.5 Bulk resistance and permeability distribution

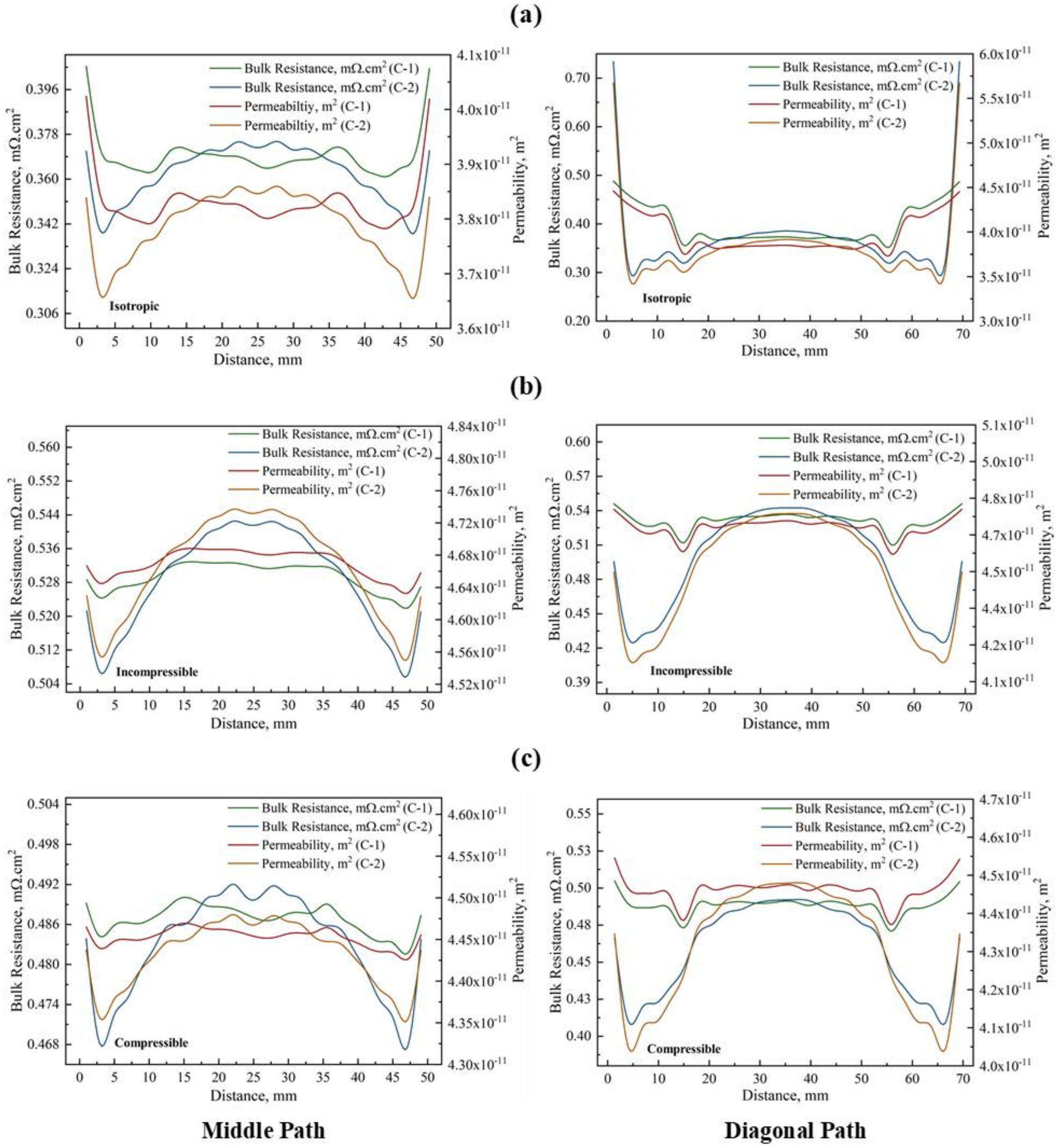

Figure 3.11 The line plots of bulk resistance and permeability distribution of GDL considering (a) GDL as Isotropic; (b) GDL as incompressible hyperelastic; and (c) GDL as compressible hyperelastic model

Further, the impact of material models and designs on the bulk transport properties of GDL is investigated. Figure 3.11 shows the variation in GDL's bulk resistance and permeability, which are extracted using the relationship outlined in Equation 3.3 and Equation 3.6, respectively. Interestingly, the distribution is non-intuitive as one can observe that the modified endplate design C-2 has resulted in increased bulk resistance and decreased permeability. In general, one expects a direct correlation between improved contact interfaces to improved bulk properties. This has not been the case for any of the chosen material models (see, Figure 3.11(a) - (c)). This is due to the localized deformation data that has been taken to arrive at these properties. For poor interface contacts (e.g., the case in C-1), the GDL surface is barely deformed, giving rise to higher interface resistance, and at the same time, it is assumed to bring no change to porosity. However, this trend reversal occurs when a moderate to good contact interface is achieved. While the incompressible GDL model may give exaggerated variation, the compressible version of the model is a good indicator to assess these interface changes and bulk properties.

3.4 Summary

The selection of GDL material models plays a vital role in quantifying bulk and interface properties. Moreover, the influence of clamping endplate design can be easily misinterpreted if it is not for nonlinear models. The isotropic elastic model offers little advantage, whereas the nonlinear incompressible case gives a qualitative understanding of the interfaces' resistance, stress, and pressure distribution. The compressible GDL model offers a reasonable solution to differentiate clamping design on the interface and bulk characteristics. This might be because the compressible model considers the varying density of the material. In contrast, incompressible one resists volume change, giving rise to increased values of measured quantities. The through-plane deformation indicates that the compressible version of the model cannot just take care of the consolidation effect but also demonstrate the differential positive to negative variation in the through-plane section. The major takeaway from this study is the inverse relationship between locally varying contact resistance and bulk resistance. In conclusion, following accurate material models, the numerical investigation can be a powerful alternative solution to complicated and not-so-cost-effective experimental methods to identify the influence of design changes. Table 3.4 briefs about the comparison of current study with the similar work done from literature.

Table 3.4 Comparison of this study with literature

Source	Outcome/Claims
Current Study	Sensitivity analysis of single cell PEFC with conventional and improved endplate designs is studied
	The use of different GDL material models in numerical investigation are explored
	A non-intuitive relationship between interface and bulk properties (electical/flow) is revealed
Wang et al. (2008)	An inbuilt hydraulically pressurized pocket is designed in the endplate to obtain more uniform pressure distribution and improve fuel cell performance.
Carrel and Mele (2014)	Higher number of cells (2-16) led to more uniform compression of MEA in centre of the stack
Alizadeh et al. (2017)	An pneumatically exerted clamping mechanism is built on the PEMFC assembly for the uniform contact pressure distribution.
Barzegari et al. (2020)	The weight and reliability of the optimized pneumatic system lead to better results than the conventional endplate configuration.

3.5 Closure

GDL material models and clamping configuration play crucial roles in quantifying the bulk and interface properties of GDL on a single-cell PEFC, as demonstrated in this chapter. In the following chapter, heterogeneous electrical and flow properties of GDL, along with varying RH on single-channel PEFC, are taken into account to evaluate transport characteristics and cell performance.

CHAPTER 4

EFFECTS OF GDL ELECTRICAL AND FLOW HETEROGENEITY ON PEFC PERFORMANCE

4.1 Introduction

GDL in PEFC is considered to be one of the main components that facilitate the transport of reactants, conducting of electrons, providing physical support to the membrane, and consecutively removing heat and products from the reaction sites (O’Hayre et al. 2016; Poornesh and Cho 2015; Zhang et al. 2013). The properties such as porosity, permeability, interfacial contact resistance (ICR), and bulk resistance of GDL play significant roles in the fuel cell performance (Akiki et al. 2012; Bhosale and Rengaswamy 2019; Gostick et al. 2006; Poornesh et al. 2010d). These properties vary substantially under mechanical compression, and in PEFCs, these GDLs may undergo non-uniform compression. In other words, this non-uniformity is caused by the uneven distribution of contact pressure during assembly clamping. Therefore, achieving fuel cell performance under these realistic conditions is highly desirable.

It is evident from the literature that numerical studies on the combined influence of electrical/flow heterogeneities and inlet RH on PEFC performance are limited. This chapter aims to examine the performance characteristics of PEFC under these conditions.

4.2 Model Description

4.2.1 Numerical Model and Assumptions

Figure 4.1 shows a schematic of a three-dimensional single-flow channel geometrical model considered in the present study. Figure 4.1(a) illustrates the homogeneous GDL condition, whereas Figure 4.1(b) illustrates the heterogeneous GDL condition. The detailed geometric model description and operating conditions are listed in Table 4.1. The assumptions made in this study are steady-state flow, multiphase, isothermal, ideal gas mixture, laminar flow, material properties being homogeneous and isotropic in membrane and anode/cathode catalyst layer. The various parameters considered in the numerical model are listed in Table 4.2. The ANSYS Fluent tool is used to carry out the analysis.

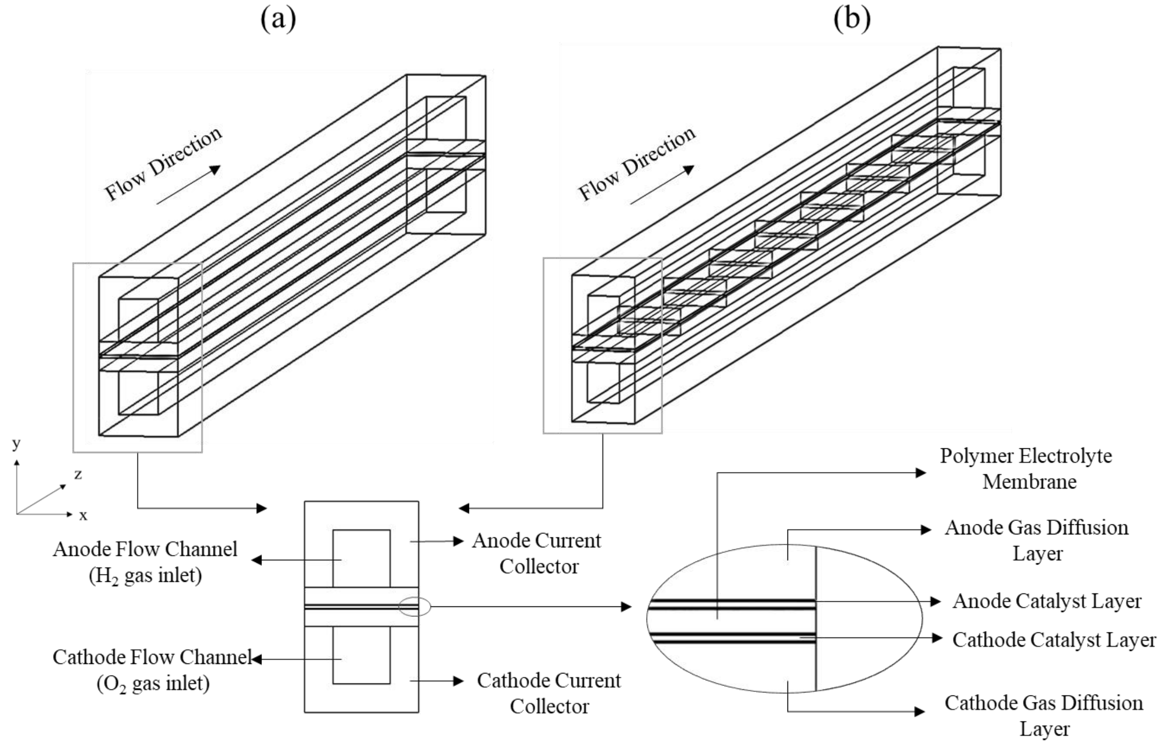
(a)
(b)
Flow Direction
Flow Direction
y
z
x
Anode Flow Channel (H_2 gas inlet)
Cathode Flow Channel (O_2 gas inlet)
Anode Current Collector
Cathode Current Collector
Polymer Electrolyte Membrane
Anode Gas Diffusion Layer
Anode Catalyst Layer
Cathode Catalyst Layer
Cathode Gas Diffusion Layer

Figure 4.1 Schematic of single channel PEMFC with (a) Homogeneous GDL; (b) Heterogeneous GDL

The list of parameters such as porosity, permeability, and ICR considered in the heterogeneous GDL case is presented in Table 4.3. The heterogeneity in GDL is known to occur due to non-uniform contact pressure induced during the assembly of the fuel cells. In this study, the GDL has been divided into eight sections along the channel flow directions. At the fuel inlet portion, the GDL is compressed more (with porosity 0.4); at the fuel outlet portion, the GDL is compressed least (with porosity 0.75). The corresponding permeability of each GDL section is listed in Table 4.3. Moreover, the non-uniform ICR occurring between GDL|CC is given in Table 4.3. These ICR values are taken from ref (Shinde and Koorata 2021) and consider that, as compressive pressure decreases, porosity increases, resulting in a higher value of ICR.

Table 4.1 Geometrical parameters and operating conditions

Parameter	**Value**	**Reference**
Fuel cell length	50 mm	(Li et al. 2017a; Li and Sundén 2018)
Fuel cell width	2 mm	
Flow channel width	2 mm	
Current Collector Rib width	1 mm	
Current Collector Rib height	1.5 mm	
GDL thickness	0.3 mm	(Wang et al. 2016)
Catalyst thickness	0.015 mm	(Padavu et al. 2021)
Membrane thickness	0.05 mm	(Li et al. 2017a; Li and Sundén 2018)
Anode/Cathode Pressure, P_a/P_c	1/1 atm	
Relative humidity, RH_a/RH_c	1) 100%/100% 2) 100%/60% 3) 60%/100% 4) 60%/60%	
Stoichiometric ratio, $\mathcal{E}_a/ \mathcal{E}_c$	1.5/2	
Operating temperature, T_a/T_c	353K/353K	

Additionally, various inlet relative humidity (RH) combinations has been carried in the present study in order to predict fuel cell performance such as:

- Homogeneous GDL without ICR (RH_a=100%, RH_c=100%),
- Heterogeneous GDL without ICR (RH_a=100%, RH_c=100%),
- Heterogeneous GDL with ICR (RH_a=100%, RH_c=100%),
- Heterogeneous GDL with ICR (RH_a=60%, RH_c=100%),
- Heterogeneous GDL with ICR (RH_a=100%, RH_c=60%),
- Heterogeneous GDL with ICR (RH_a=60%, RH_c=60%).

The reason behind considering RH values at anode and cathode of different combinations is due to the fact that performance of PEMFC varies along with the consideration of ICR and heterogeneous compression of the GDL (Zhou and Wu 2007).

Table 4.2 Parameters considered in the numerical model

Parameter	**Value**	**Reference**
Reference current density, I_{ref}	10000 A/m^2	(Padavu et al. 2021)
Anode reference exchange current density, $i_{0,a}^{ref}$	7496.25 A/m^2	Calculated
Cathode reference exchange current density, $i_{0,c}^{ref}$	0.003748 A/m^2	Calculated
Anode transfer coefficient, α_a	0.5	(Li et al. 2017b; Padavu et al. 2021)
Cathode transfer coefficient, α_c	1	
Reference hydrogen concentration, C_{H2}^{ref}	40.88 mol/m^3	
Reference oxygen concentration, C_{O2}^{ref}	40.88 mol/m^3	
Porosity of GDL, ε_{gdl} (for heterogeneous case refer Table 4.3)	0.8	(Wang et al. 2016)
Permeability of GDL, K_{gdl} (for heterogeneous case refer Table 4.3)	8.53 x 10^{-12} m^2	Calculated
Porosity of CL, ε_{cl}	0.2	(Li et al. 2017b)
Permeability of CL, K_{cl}	2 x 10^{-13} m^2	
Electrical conductivity of CC, σ_{cc}	14,000 S/m	
Electrical conductivity of GDL, σ_{gdl}	1,250 S/m	
Electrical conductivity of CL, σ_{cl}	300 S/m	
Thermal conductivity of CC, k_{cc}	20 W/mK	
Thermal conductivity of GDL, k_{gdl}	1 W/mK	
Thermal conductivity of CL, k_{cl}	1 W/mK	

Table 4.3 Parameters of heterogeneous GDL porosity, permeability and ICR at interface of GDL|CC

GDL Section	**Porosity**	**Permeability,** m^2	**ICR,** ohm.m^2
1	0.4	1.2×10^{-13}	4.8×10^{-7}
2	0.45	2.0×10^{-13}	4.9×10^{-7}
3	0.5	3.3×10^{-13}	5.0×10^{-7}
4	0.55	5.5×10^{-13}	5.1×10^{-7}
5	0.6	9.0×10^{-13}	5.2×10^{-7}
6	0.65	1.5×10^{-12}	5.3×10^{-7}
7	0.7	2.5×10^{-12}	5.4×10^{-7}
8	0.75	4.5×10^{-12}	5.5×10^{-7}

The fuel cell computational domain consists of two flow channels, two GDLs, two catalysts and a membrane. The grid size in the single flow channel is 55 grid points in the through-plane direction (y-axis), 10 grid points in flow channels (x-axis), 5 grid points in the land portion on either side of flow channels (x-axis) and 480 grid points along the flow channel (z-axis).

4.2.2 Governing Equations

4.2.2.1 Equation for mass conservation

$$\nabla \cdot \left(\rho \vec{u} \right) = S_{mass} \tag{4.1}$$

where ρ is density of fluid mixture (kg/m^3.s), $\vec{u}$ is fluid velocity vector (m/s) and S_m is the mass source/sink term (kg/m^3.s) given in Table 4.4.

4.2.2.2 Equation for momentum conservation

$$\nabla \cdot \left(\rho \vec{u} \vec{u} \right) = \nabla \cdot \left(\mu \nabla \vec{u} \right) - \nabla P + S_{mom} \tag{4.2}$$

where P is pressure mixture (N/m^2), μ is dynamic viscosity (kg/m.s), and S_{mom} is the source term for drop in pressure in porous component for fluid flow derived from Darcy's law (kg/m^3.s^2) provided in Table 4.4.

4.2.2.3 Equation for species conservation

$$\nabla \cdot \left(\rho \vec{u} Y_i \right) = \nabla \cdot \left(\rho D_{eff,i} \Delta Y_i \right) + S_i \tag{4.3}$$

where Y_i is mass fraction, $D_{eff,i}$ is ith species effective diffusivity (m^2/s) and S_i is the species source/sink term (kg/m^3.s) given in Table 4.4.

Using Bruggeman correlation, effective diffusivity is evaluated on the tortuous flow of porous components given by:

$$D_{eff,i} = \varepsilon^{1.5} D_{i,m} \tag{4.4}$$

where $D_{i,m}$ is the mass diffusivity of ith species in the mixture (m^2/s), and ε is the porosity.

4.2.2.4 Equation for energy conservation

$$\nabla \cdot \left(\rho c_p \vec{u} T \right) = \nabla \cdot \left(k_{eff} \Delta T \right) + S_T \tag{4.5}$$

where c_p is specific heat (J/kg.K), k_{eff} is effective thermal conductivity (W/m.K) and S_T is the source term associated for entropy losses during electrochemical reactions listed in Table 4.4.

$$k_{eff} = \left(1 - \varepsilon\right) k_s + \varepsilon k_f \tag{4.6}$$

where k_s and k_f are the thermal conductivity of the solid and gas phases (W/m.K), respectively.

4.2.2.5 Equation of charge conservation

$$\nabla \cdot \left(\sigma_{eff,s} \nabla \phi_s \right) + S_s = 0 \tag{4.7}$$

$$\nabla \cdot \left(\sigma_{eff,m} \nabla \phi_m \right) + S_m = 0 \tag{4.8}$$

where $\sigma_{eff,s}$ and $\sigma_{eff,m}$ is the effective electronic and protonic conductivity, whereas S_s and S_m are source terms in anode and cathode CL (A/m3) listed in Table 4.4.

Table 4.4 List of source terms considered in governing equations

Source Term	**Units**	**Zone**
$S_{mass} = S_{H_2}$	kg/m^{3}s	Anode CL
$S_{mass} = S_{O_2}$	kg/m^{3}s	Cathode CL
$S_{mass} = S_{H_2O}$	kg/m^{3}s	Cathode CL
$S_{mom} = -\frac{\mu}{K}\vec{u}$	kg/m^{2}s^2	Anode/Cathode GDL & CL
$S_{H_2} = -\frac{j_a}{2F}M_{H_2}$	kg/m^{3}s	Anode CL
$S_{O_2} = -\frac{j_c}{2F}M_{O_2}$	kg/m^{3}s	Cathode CL
$S_{H_2O} = -\frac{j_c}{2F}M_{H_2O}$	kg/m^{3}s	Cathode CL
$S_T = j_a \mid \eta_a \mid + \sigma_{eff,m}\nabla\phi_m^2 + \sigma_{eff,s}\nabla\phi_s^2$	W/m^3	Anode CL
$S_T = j_c \mid \eta_c \mid - j_c \frac{dU_o}{dT}T + \sigma_{eff,m}\nabla\phi_m^2 + \sigma_{eff,s}\nabla\phi_s^2$	W/m^3	Cathode CL
$S_T = \sigma_{eff,m}\nabla\phi_m^2$	W/m^3	Membrane
$S_T = \sigma_{eff,s}\nabla\phi_s^2$	W/m^3	Anode/Cathode GDL
$S_s = -j_a$	A/m^3	Anode CL
$S_s = +j_c$	A/m^3	Cathode CL
$S_m = +j_a$	A/m^3	Anode CL
$S_m = -j_c$	A/m^3	Cathode CL

4.2.2.6 Volumetric current densities

The reactions taking place at anode CL and cathode CL are described using Butler-Volmer equations as given below:

$$j_a = i_a a \left(\frac{C_{H_2}}{C_{H_2}^{ref}} \right)^{\frac{1}{2}} \left[e^{\alpha_a F \eta_a / RT} - e^{-\alpha_c F \eta_a / RT} \right] \tag{4.9}$$

$$\eta_a = \phi_s - \phi_m \tag{4.10}$$

$$j_c = i_c a \left(\frac{C_{O_2}}{C_{O_2}^{ref}} \right)^{1} \left[-e^{\alpha_a F \eta_c / RT} + e^{-\alpha_c F \eta_c / RT} \right] \tag{4.11}$$

$$\eta_c = \phi_s - \phi_m - E \tag{4.12}$$

where j_a, j_c are volumetric current densities (A/m^3), i_a, i_c are reference exchange current densities (A/m^2), α_a, α_c are transfer coefficients, F is Faradays constant (96487 C/mol), η_a, η_c are overpotentials (V), C_{H_2}, C_{O_2} are hydrogen and oxygen species concentrations, $C_{H_2}^{ref}$, $C_{O_2}^{ref}$ are reference hydrogen and oxygen species concentration ϕ_s, ϕ_m are phase potentials of solid and membrane, R is the universal gas constant (8.314 J/mol.K), E is the Nernst voltage (V), and T is the temperature (K). The subscripts a and c represent anode and cathode, respectively.

4.2.2.7 Electronic Conductivity

The electronic conductivity in GDL and CL is given by,

$$\sigma_{eff,s} = \varepsilon_s^{1.5} \sigma_s \tag{4.13}$$

where $\sigma_{eff,s}$ is the effective electronic conductivity, ε_s is the porosity, and σ_s is the electronic conductivity of GDL and CL, respectively.

4.2.2.8 Electrolyte Conductivity

The electrolyte (or the membrane) conductivity is calculated using,

$$\sigma_{\text{mem}} = \left(0.514\lambda - 0.326\right) \cdot \exp\left[1268\left(\frac{1}{303} - \frac{1}{T}\right)\right] \tag{4.14}$$

where λ is water content in membrane and T is the operating temperature (K)

4.2.2.9 Dissolved phase model

In the catalyst layers (ionomers) and the membrane, dissolved phases exist. The equation for transport and generation of the dissolved water phase is given by

$$\nabla\left(\vec{i}_m \frac{n_d}{F} M_w\right) - \nabla\left(M_w D_w^i \nabla\lambda\right) = S_{ld} + S_{gl} + S_\lambda \tag{4.15}$$

where

$$\vec{i}_m = -\sigma_{mem}\nabla\phi_{mem} \tag{4.16}$$

is the ionic current density, and ϕ_{mem} is the membrane potential.

$$S_{gd} = \left(1 - s^\theta\right)\gamma_{gd} M_{w,H_2O}\frac{\rho_i}{EW}\left(\lambda_{eq} - \lambda\right) \tag{4.17}$$

$$S_{ld} = s^\theta \gamma_{ld} M_{w,H_2O}\frac{\rho_i}{EW}\left(\lambda_{eq} - \lambda\right) \tag{4.18}$$

S_{gd} is the rate of mass change between gas and dissolved phases, S_{ld} is the rate of mass change between liquid and dissolved phases, $M_{w,H2O}$ is water molecular mass, ρ_i is the membrane density, EW is the membrane equivalent weight, λ is the dissolved water content, λ_{eq} is the equilibrium water content, n_d is the osmotic drag coefficient, S_λ is the water generation rate at the cathode side reaction, D_w^i is water content's diffusion coefficient, γ_{gd}, γ_{ld} is gas and liquid mass exchange rate constants.

The equilibrium water content is described as below,

$$\begin{aligned}\lambda_{eq} = {} & 0.3 + 6a\left(1 - \tanh\left(a - 0.5\right)\right) + 0.69\left(\lambda_{a=1} - 3.52\right) \\ & \times a^{0.5}\left(1 + \tanh\left(\frac{a - 0.89}{0.23}\right)\right) + s\left(\lambda_{s=1} - \lambda_{a=1}\right)\end{aligned} \tag{4.19}$$

where a is the water activity

$$a = \frac{p_{wv}}{p_{sat}} \tag{4.20}$$

where p_{wv} is the partial pressure of water vapour, and p_{sat} is the saturation pressure

4.2.2.8 Liquid water transport model

The equation for liquid water transport in GDL and membrane is given by,

$$\nabla\left(\frac{\rho_l K K_r}{\mu_l}\nabla\left(p_c + p\right)\right) = S_{ld} - S_{gl} \tag{4.21}$$

The relative permeability in porous GDLs is obtained using

$$K_r = s^b \tag{4.22}$$

Relative permeability in membrane is given by

$$K_r = \left(\frac{\frac{M_{w,H_2O}}{\rho_l}\lambda_{s=1} + \frac{EW}{\rho_l}}{\frac{M_{w,H_2O}}{\rho_l}\lambda + \frac{EW}{\rho_l}} \cdot \frac{\lambda}{\lambda_{s=1}} \right)^2 \tag{4.23}$$

where ρ_l is liquid water density, μ_l is liquid dynamic viscosity, K, K_r is absolute, and relative permeability, p_c, p_l, p are capillary, liquid and gas pressure.

Capillary pressure (p_c) is a function of saturation, liquid saturation, which can computed as defined below,

$$p_c = \sigma\left|\cos\theta_c\right|\sqrt{\frac{\varepsilon}{K}}J\left(s\right) \tag{4.24}$$

$$J\left(x\right) = ax - bx^2 + cx^3 \tag{4.25}$$

where σ is the surface tension, θ_c is the contact angle, and a, b, and c are the user-defined Leverett function parameters as described in Eq. (23).

4.2.3 Boundary Conditions

Anode terminal is selected by assigning anode land region $\phi_s = 0$, and for the cathode terminal cathode land region is assigned as $\phi_s = V_{cell}$

4.2.3.1 Anode and Cathode inlet velocity

$$U_{in,a} = \xi_a \cdot \frac{I_{ref}}{2Fx_{H_2}}\left(\frac{A_r RT}{A_i P_a}\right) \tag{4.26}$$

$$U_{in,c} = \xi_c \cdot \frac{I_{ref}}{4Fx_{O_2}}\left(\frac{A_r RT}{A_i P_c}\right) \tag{4.27}$$

where $U_{in,a}$, $U_{in,c}$ are inlet velocities of reactants (m/s), ξ_a, ξ_c are stoichiometric ratios, x_{H_2}, x_{o_2} are mass fractions of hydrogen and oxygen reactants, A_r is membrane reactive area (m^2), A_i is the inlet cross-section area the of flow channel (m^2), P_a, P_c are inlet gas pressure (atm). Subscripts a and c denotes anode and cathode.

The mass fraction at the anode inlet is obtained using,

$$x^a{}_{H_2O} = \frac{P_{sat} \cdot RH_a}{P_a} \tag{4.28}$$

$$x_{H_2} = 1 - x^a{}_{H_2O} \tag{4.29}$$

$$P_{sat} = \left(10^{\left[-2.1794+(0.022953)(T-273)-\left(9.1837\times10^{-5}\right)(T-273)^2+\left(1.4454\times10^{-7}\right)(T-273)^3\right]}\right) \times 101325 \tag{4.30}$$

Similarly, the mass fraction at cathode is obtained using,

$$x^c{}_{H_2O} = \frac{P_{sat} \cdot RH_c}{P_c} \tag{4.31}$$

$$x_{O_2} = 0.21\left(1 - x^c{}_{H_2O}\right) \tag{4.32}$$

where $x^a_{H_2O}$, $x^c_{H_2O}$ are anode and cathode inlet mass fractions, P_{sat} is the saturation pressure of water vapour at anode (P_a) and at cathode (P_c), RH_a and RH_c are inlet relative humidity at anode and cathode respectively.

4.3 Results and discussion

4.3.1 Cell performance

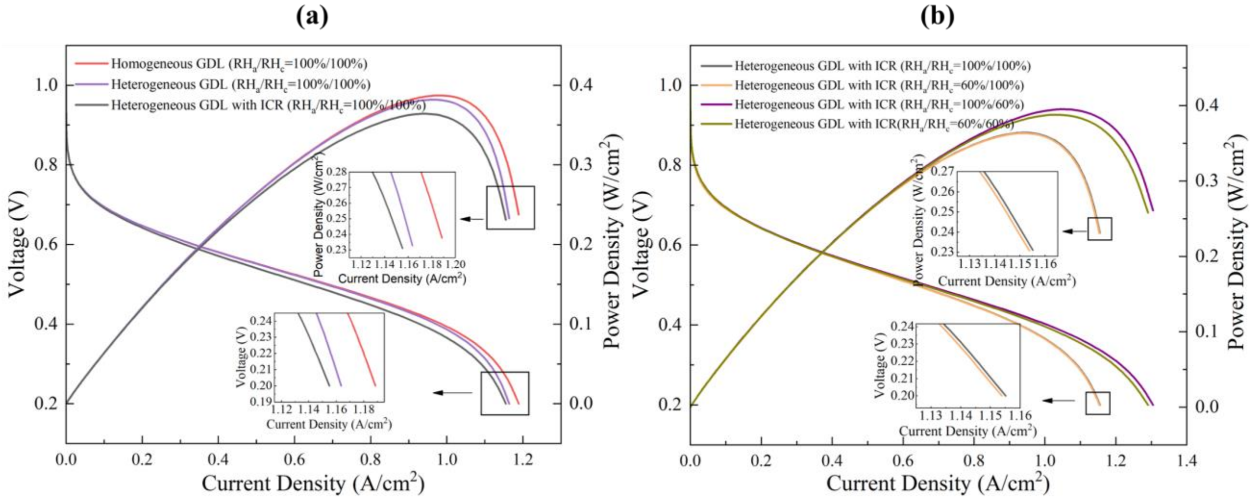

Figure 4.2 Cell performance under (a) full humidification conditions, (b) different humidification conditions

Figure 4.2 shows cell performance plots of all the simulation cases. Two sets of cases are compared. In the first set, as can be seen from Figure 4.2(a), simulation cases with fully humidified inlets are compared. It is seen that the current density for homogeneous, heterogeneous GDL (w/o ICR), and heterogeneous GDL (w/ ICR) cases is around 1.189 A/cm^2, 1.164 A/cm^{2,} and 1.155 A/cm^{2,} respectively at 0.2 V. As expected, consideration of ICR results in reduced current and power density, beginning from the ohmic region of interest. It is also very practical to consider non-uniform ICR in the computational model. Figure 4.2(b) shows cell performance curves obtained with different combinations of inlet humidity conditions for heterogeneous GDL with a non-uniform ICR case (as it is the most practical case to be simulated). The current density at 0.2 V for RH$_a$|RH$_c$ of 100%|100%, 60%|100%, 100%|60%, and 60%|60% is around 1.155 A/cm^2, 1.154 A/cm^2, 1.305 A/cm^2, and 1.291 A/cm^2, respectively. This is to say that the performance is highest in the case of the fully humidified anode and partially humidified cathode (i.e., $RH_a|RH_c$ = 100%|60%). This could be as a fully humidified cathode inlet may lead to flooding and inhibit reactant reaction kinetics and transport. On the other hand, a partially humidified anode may lead to lower membrane conductivity, causing a loss in performance.

4.3.2 Hydrogen mass fraction distribution

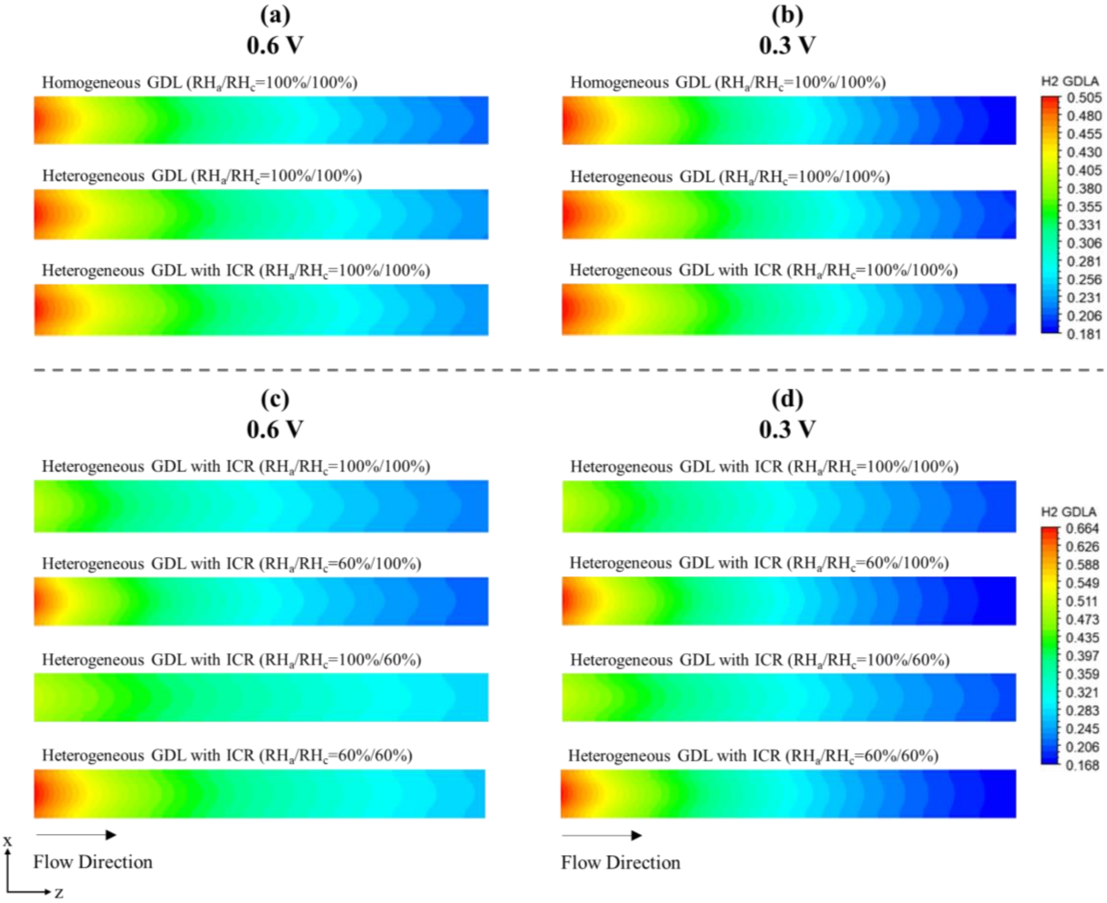

Figure 4.3 Hydrogen mass fraction distribution in midsection of anode GDL at: (a) 0.6 V with full humidification, (b) 0.3 V with full humidification, (c) 0.6 V with different humifications, (d) 0.3 V with different humifications

The H_2 mass fraction distributions in the midsection of anode GDL at 0.6 V and 0.3 V cell voltages for all cases are shown in Figure 4.3. It can be seen from Figures 4.3(a) and 4.3(b) that the maximum H_2 mass fraction under full humidification ($RH_a|RH_c$ = 100%|100%) is at the inlet, and the distribution is almost the same. While at the outlet in homogeneous GDL (w/o ICR), heterogeneous GDL (w/o ICR), and heterogeneous with ICR varies under 0.6 V and 0.3 V, indicating the consumption of H_2 reactants at lower voltages. It is also seen that heterogeneous GDL with ICR results in more diffusion of reactants (less gradient) compared to homogeneous and heterogeneous GDL without ICR. Further, Figure 4.3(c) and 4.3(d) illustrate the H_2 mass fraction under different humidification conditions. It is clear that at $RH_a|RH_c$ = 100%|60%, diffusion of H_2 reactants at 0.6 V and 0.3 V is significant, with more consumption of H_2 at lower voltages. At 0.3 V, a magnitude difference of 0.219 in H_2 mass fraction is seen, while in other cases, 0.229, 0.466, and 0.496 for $RH_a|RH_c$ of 100%|100%, 60%|100 and 60%|60%, respectively, is observed. Therefore, it is implied that enhanced diffusion of H_2 reactant from inlet to outlet leads to increased activity of hydrogen oxidation reaction (HOR) in the case of heterogeneous GDL with ICR at $RH_a|RH_c$ = 100%|60%. A higher amount of H_2 at an inlet in the case of $RH_a|RH_c$ = 60%|100% and 60%|60% is due to lower inlet humidity at the anode side. The distribution of hydrogen mass fraction in anode catalyst shows a similar pattern at higher current loads with a more uniform distribution of hydrogen reactants for the case of $RH_a|RH_c$ = 100%|60% as described in Figure 4.4.

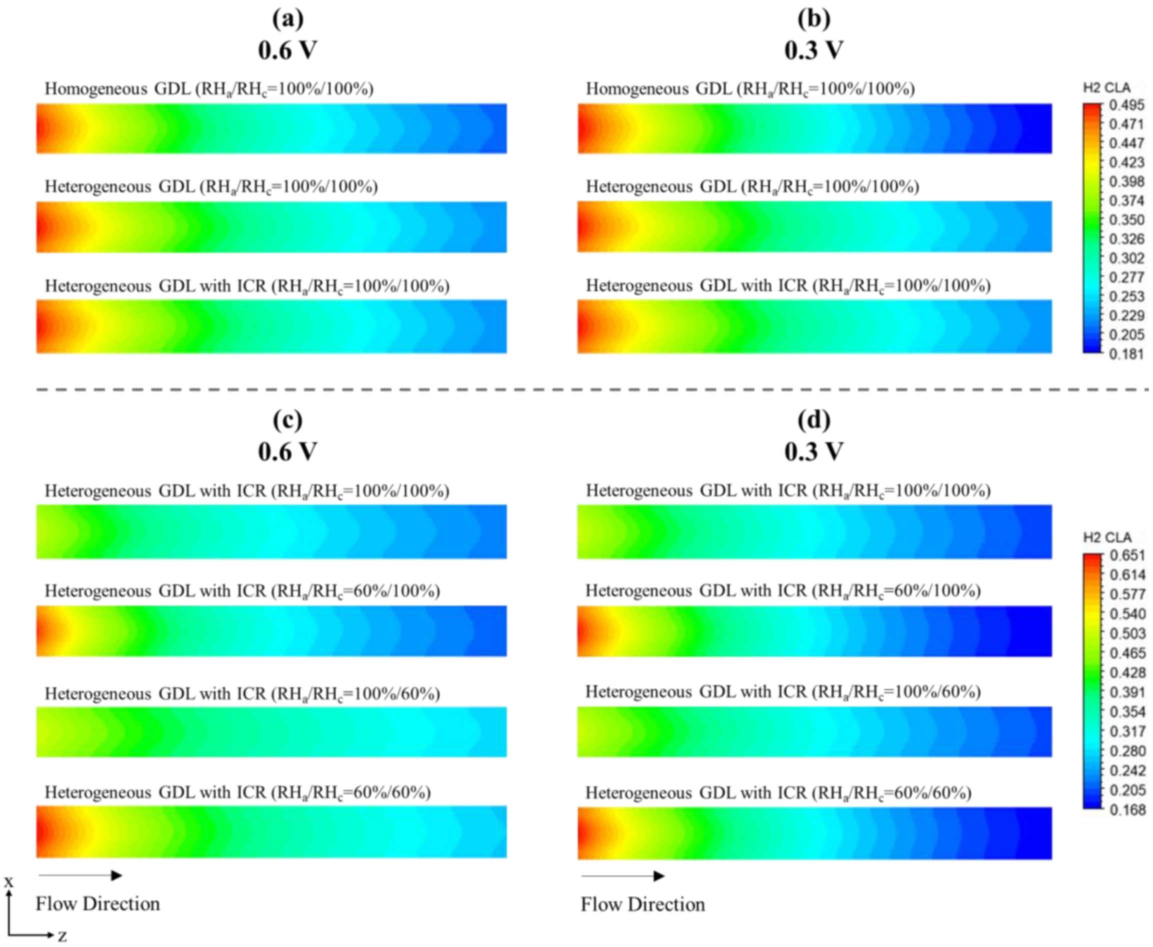

Figure 4.4 Hydrogen mass fraction distribution in midsection of anode catalyst at: (a) 0.6 V with full humidification, (b) 0.3 V with full humidification, (c) 0.6 V with different humifications, (d) 0.3 V with different humifications

4.3.3 Oxygen mass fraction distribution

The oxygen mass fraction distributions in the midsection of cathode GDL at 0.6 V and 0.3 V for all the aforementioned cases are shown in Figure 4.5. It is observed from Figure 4.5(a) that at 0.6 V, the O_2 mass fraction distribution is almost uniform, indicating a lack of consumption of the reactant. At higher loads, as in Figure 4.5(b), reasonable consumption of reactants from inlet to outlet is observed, with values approaching zero at the end. With the maximum amount of oxygen reactants available at the inlet for $RH_a|RH_c$ = 100%|60% and 60%|60%, a clear indication of reactant consumption is visible from Figure 4.5(c) to Figure 4.5(d) with average O_2 mass fraction of 0.13 at 0.6 V to 0.03 at 0.3 V; a difference of 0.1.

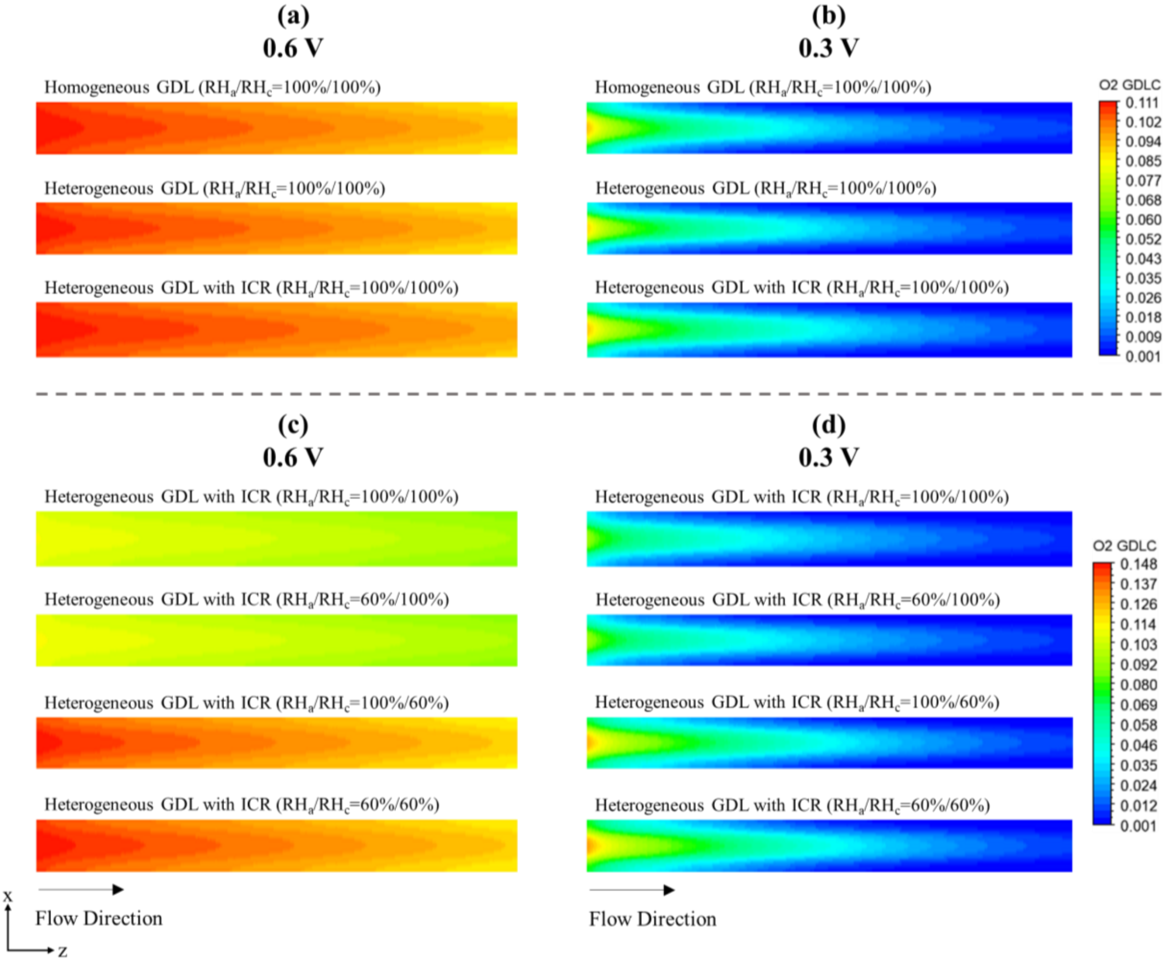

Figure 4.5 Oxygen mass fraction distribution in midsection of cathode GDL at: (a) 0.6 V with full humidification, (b) 0.3 V with full humidification, (c) 0.6 V with different humifications, (d) 0.3 V with different humifications

This, however, is not true in the case of a fully humidified cathode, where this difference falls to 0.065. It is known that as RH at the cathode lowers, the availability of O_2 for oxygen reduction reaction (ORR) is higher, reducing the immediate risk of cathode flooding and improving cell performance (Kahveci and Taymaz 2015). This seems to have been reflected in the performance curve (Figure 4.2(b)). On an interesting note, though there exist a slight difference in oxygen reactant distribution for $RH_a|RH_c$ =100%|60% and 60%|60%, the cell performance with $RH_a|RH_c$ =100%|60% provides higher performance, perhaps due to reasonable water content in the membrane. The water concentration on the cathode side is discussed in subsequent sections. This O_2

reactant distribution pattern is similar for the midsection of the cathode catalyst, as plotted in Figure 4.6

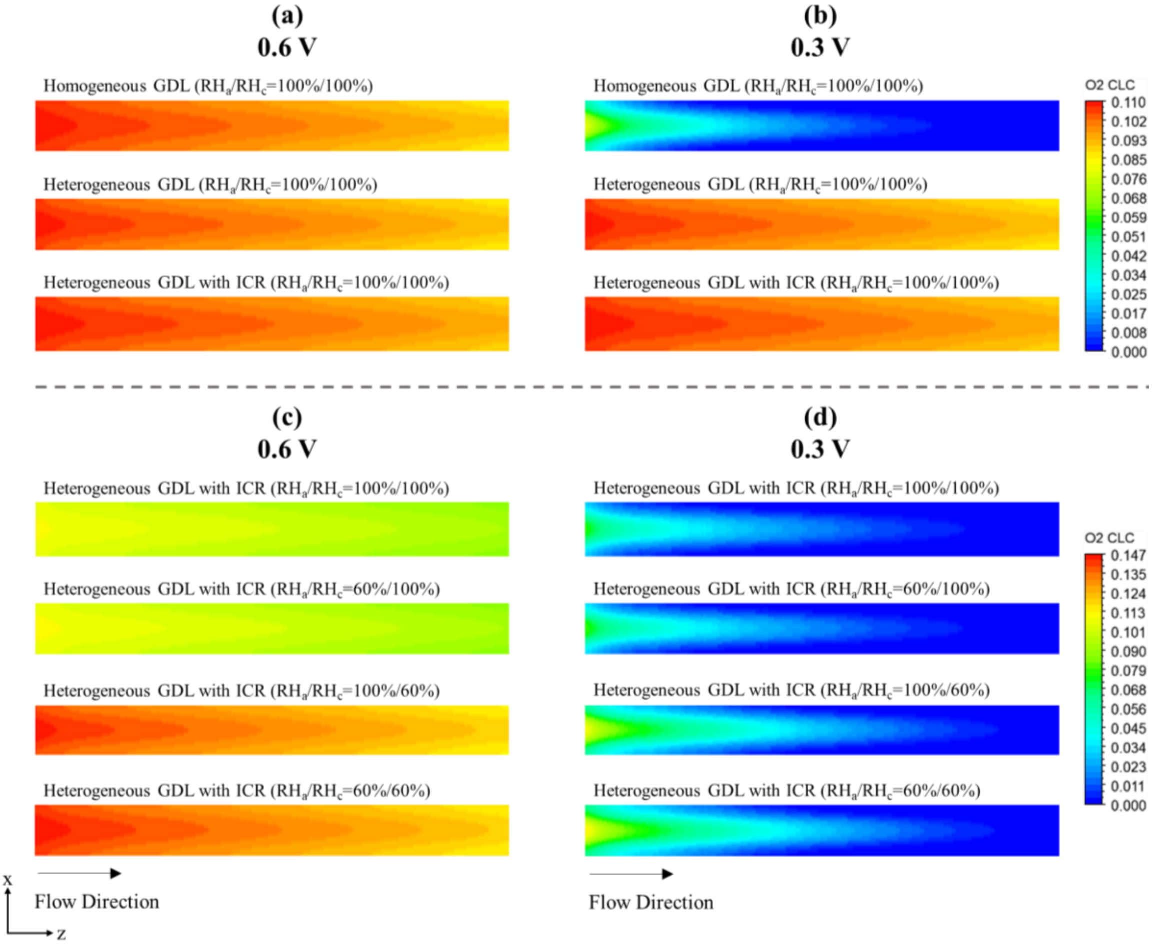

Figure 4.6 Oxygen mass fraction distribution in midsection of cathode catalyst at: (a) 0.6 V with full humidification, (b) 0.3 V with full humidification, (c) 0.6 V with different humifications, (d) 0.3 V with different humifications

4.3.4 Water content distributuion

Excess membrane water content may lead to cathode flooding, while lower water content dries the membrane. Hence water management of membrane during fuel cell operation becomes crucial (Yinqi Shen 2017). Figure 4.7 illustrates the water content distributions in the midsection of the membrane at 0.6 V and 0.3 V for all the simulated cases. As expected, the membrane water content is higher at high loads, and heterogeneous GDL cases show relatively less water fraction than their homogenous counterpart (Figure 4.7(a) and (b)). Cathode inlet humidity directly impacts the water content distribution in the membrane, with partial cathodic humidification leading to a lowest water content of ~4.5 (Figure 4.7(c)) under low load. However, as seen in Figure 4.7(d), at 0.3 V, a higher amount of water in the membrane is observed, perhaps due to increased reaction kinetics. The case with $RH_a|RH_c$ =100%|60% gives better performance (Figure 4.2(b)) as water distribution is nominal, not too high or too low.

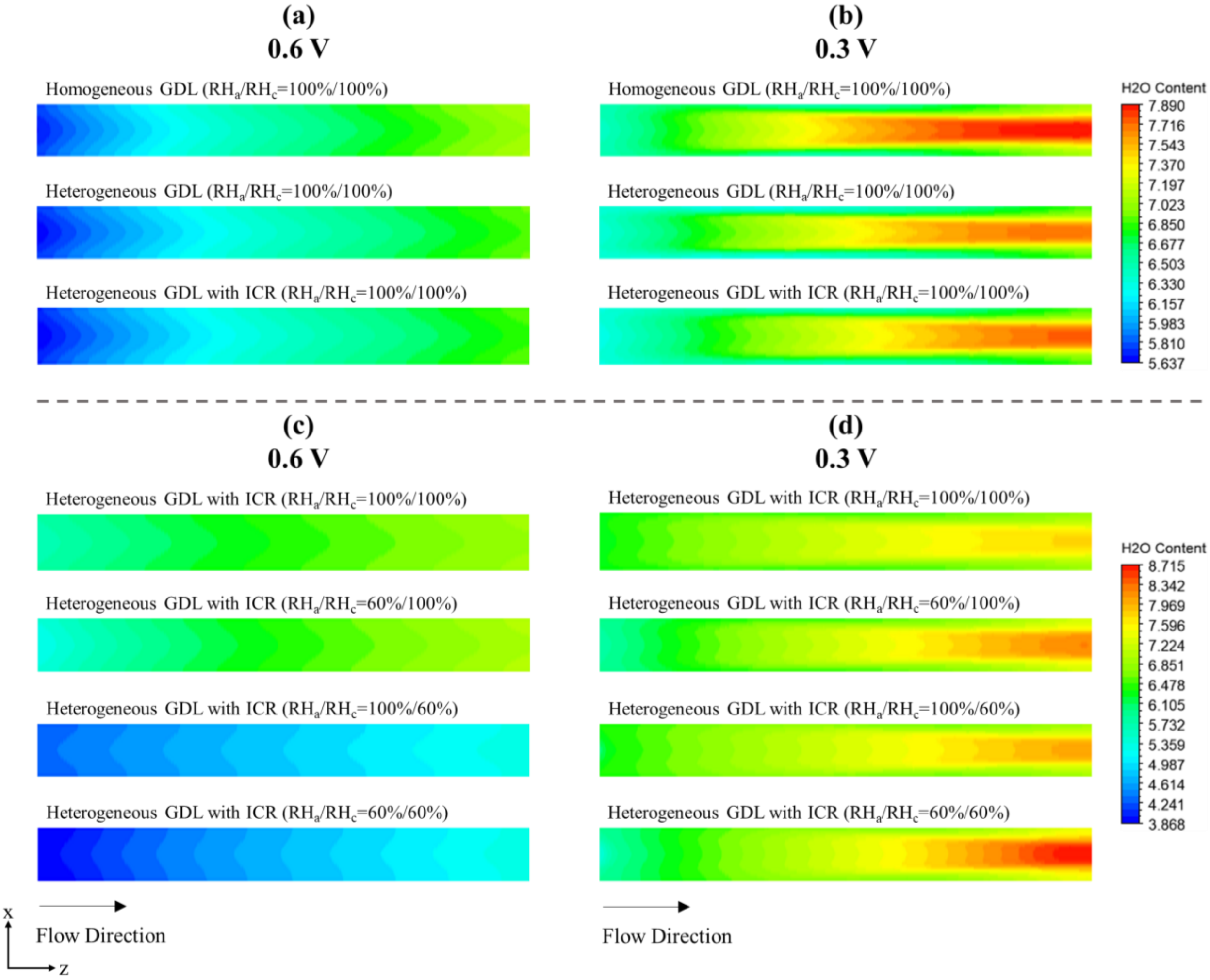

Figure 4.7 Water content distribution in midsection of membrane at: (a) 0.6 V with full humidification, (b) 0.3 V with full humidification, (c) 0.6 V with different humifications, (d) 0.3 V with different humifications

4.3.5 Local current density distribution

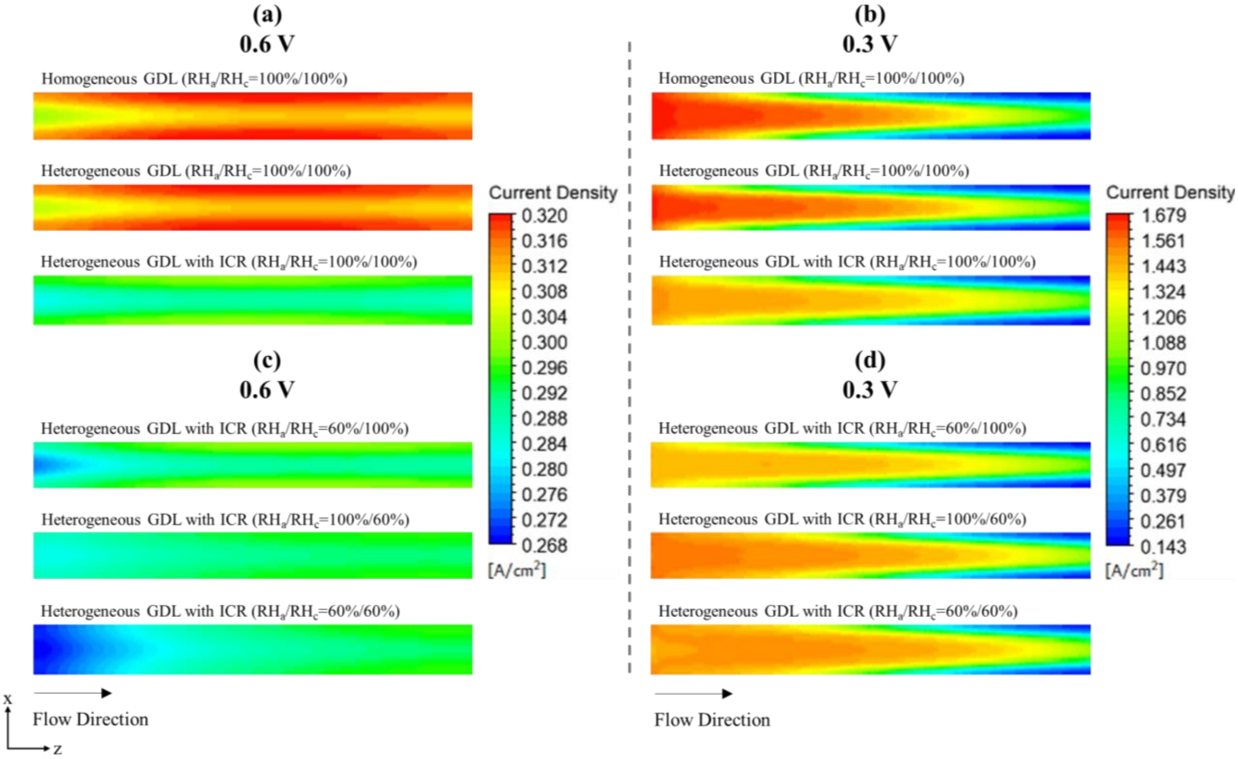

Figure 4.8 Local current distribution in midsection of membrane at: (a) 0.6 V with full humidification, (b) 0.3 V with full humidification, (c) 0.6 V with different humifications, (d) 0.3 V with different humifications

Figure 4.8 shows plots for local current density at the mid-section of the membrane. A low local current density indicates poor ORR kinetics. As shown in Figure 4.8(a), at low load, the current density is higher for the homogenous case and uniform overall. The maximum current density obtained at a higher load is about 1.679 A/cm^2 (Figure 4.8(b)). A reduction of 150-300 mA/cm^2 is observed in the case of flow and electrical heterogeneities. With reference to inlet humidity variations, one can observe from Figure 4.8(c) that a near-uniform current density distribution is observed in case of $RH_a|RH_c$ = 100%|60%. Moreover, at higher load, as observed from Figure 4.8(d), this case exhibits higher current density distribution at around 1.5 A/cm^2. This is the reason for higher performance observed for this particular case, as in Figure 4.2(b). The non-uniformity in local current density distribution from inlet to outlet, which was not clear at lower loads, is due to the reduced amount of O_2 reactant.

4.3.6 Temperature distribution

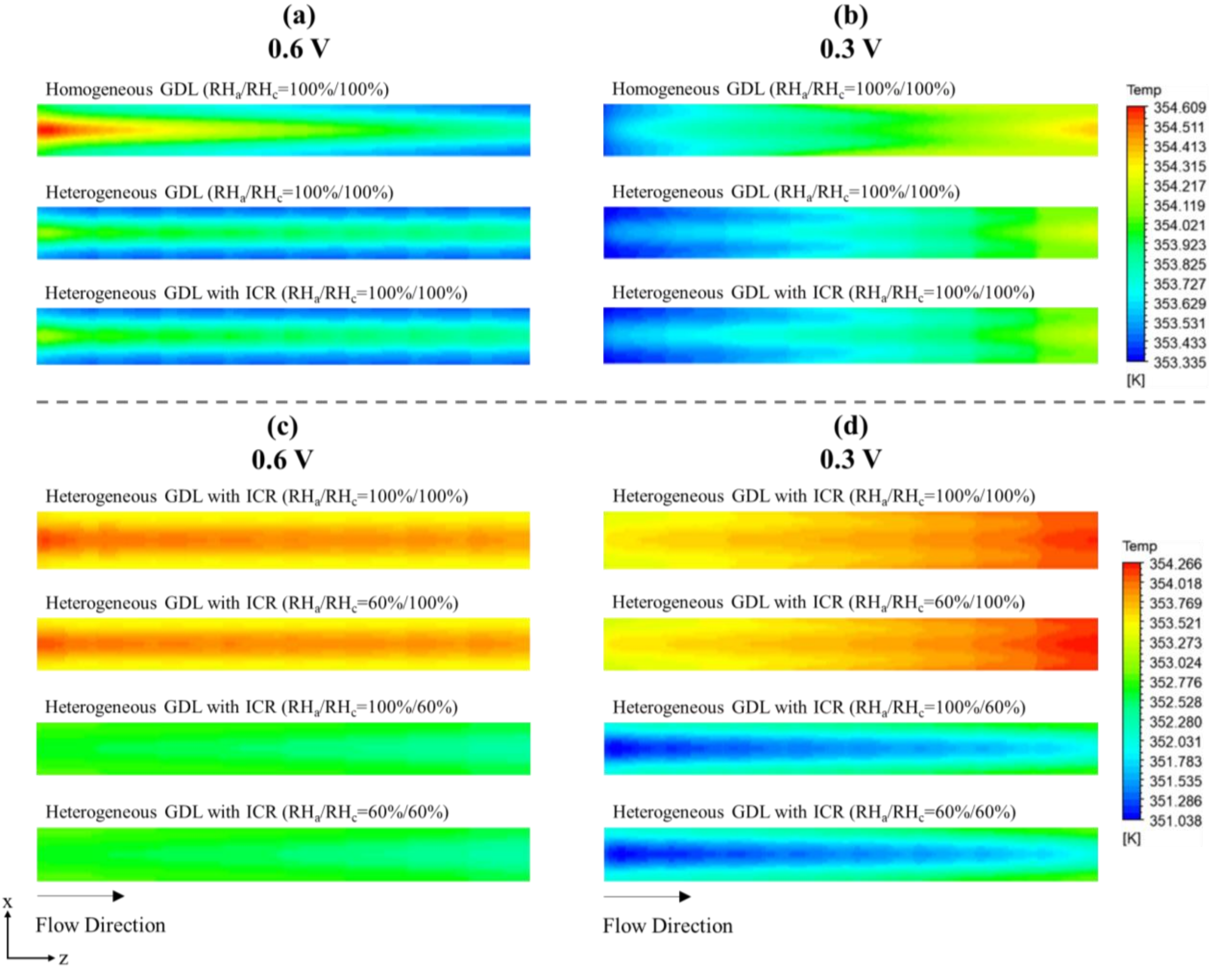

Figure 4.9 Temperature distribution in midsection of membrane at: (a) 0.6 V with full humidification, (b) 0.3 V with full humidification, (c) 0.6 V with different humifications, (d) 0.3 V with different humifications

The temperature distribution in midsection of membrane is plotted in Figure 4.9. As in Figure 4.9(a) and (b), for 0.6 V, the temperature is higher at the inlet, and for 0.3V, the temperature is higher near the exit. It is vital to note that the temperature is higher in the channel region than in the rib region. This might be due to enhanced contact thermal conductivity in the rib region. The higher temperature gradient towards the exit at high load may be due to reaction kinetics, and the reasons could be clarified from the cathodic water concentration distribution pattern (as discussed later). Overall, from Figure 4.9(a) and (b), it is observed that the maximum to minimum temperature difference is only ~1K. This, however, is not true when the cell is tested with different inlet humidity conditions. Figure 4.9(c) shows that irrespective of anodic inlet humidity conditions, a fully humidified cathode gives rise to higher temperatures. This trend is also maintained at higher loads, as seen in Figure 4.9(d). When cathodic inlet humidity drops to 60%, the temperature at 0.6 V is as same as the input temperature of 353K. Whereas at higher load, i.e., at 0.3 V, the temperature decreases further to ~350K, and now, this time, the channel region has a lesser temperature than the rib region. This is to say that the cooling effect has more to do with reaction kinetics-induced water production than inlet humidity. Notably, variation in anodic humidity has less impact on change in temperature distribution. All in all, in the case of Figure 4.9(c) and (d), the maximum to minimum temperature difference is ~3K.

4.3.7 Water mass fraction distribution

Figure 4.10 shows the water mass fraction in midsection of cathode catalyst layer. As observed from Figure 4.10(a) and 4.10(b), the water concentration is higher at higher loads, and GDL's flow/electrical heterogeneity reduces this concentration. The increased inhomogeneity in the distribution of water concentration from inlet to outlet at 0.3 V might have affected the temperature distribution pattern, as observed in Figure 4.9(b). Figures 4.10(c) and (d) show that irrespective of anode inlet humidity, cathode inlet humidity directly impacts water concentration in the cathode catalyst layer. It is interesting to note here that increase in water concentration at higher loads in fully humidified cathode cases is comparatively much less (0.42 at 0.6 V to 0.476 at 0.3 V) than partially humidified cathode cases (0.266 at 0.6 V to 0.38 at 0.3 V).

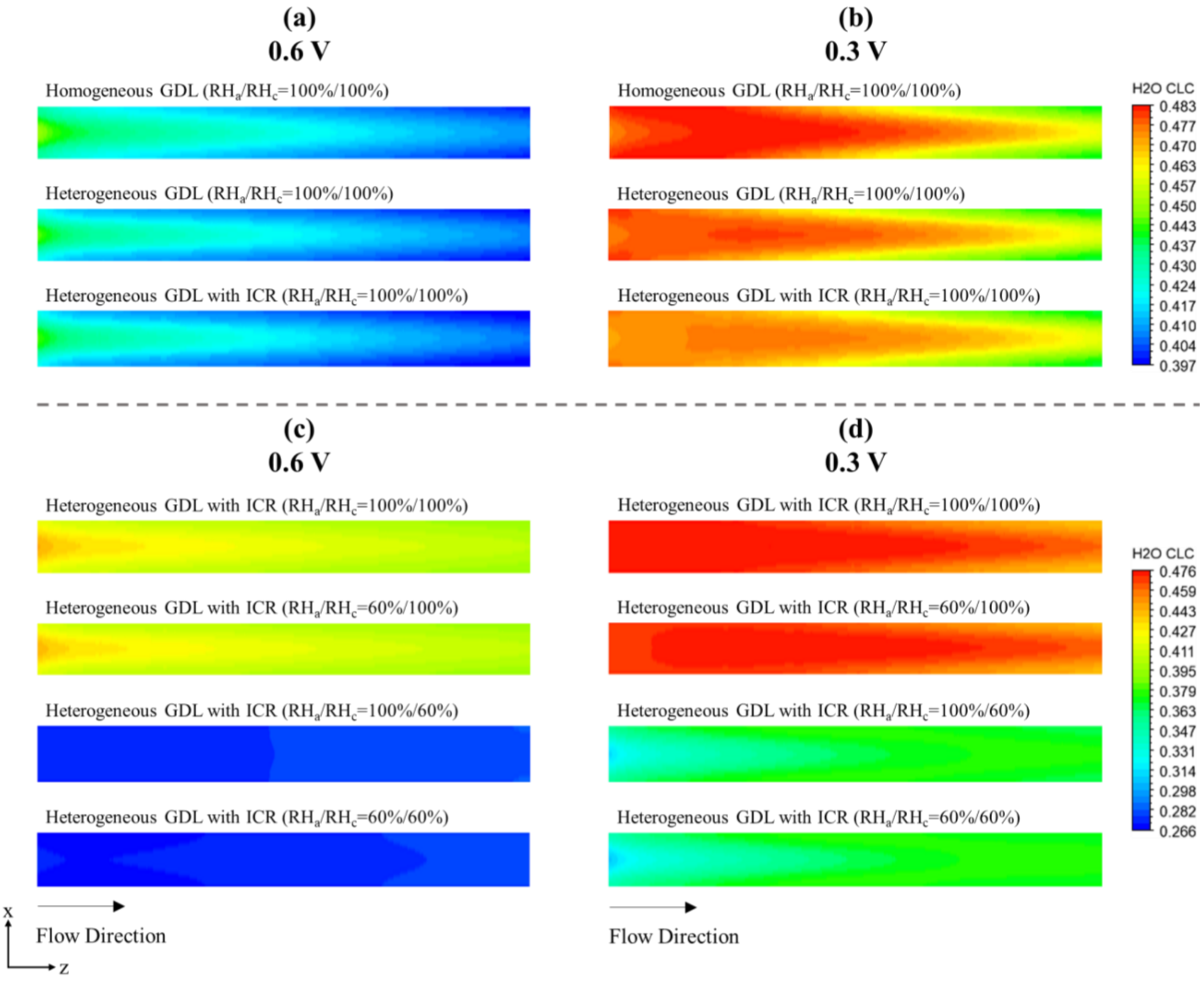

Figure 4.10 Water mass fraction distribution in midsection of cathode catalyst at: (a) 0.6 V with full humidification, (b) 0.3 V with full humidification, (c) 0.6 V with different humifications, (d) 0.3 V with different humifications

4.3.8 Cathodic overpotential distribution

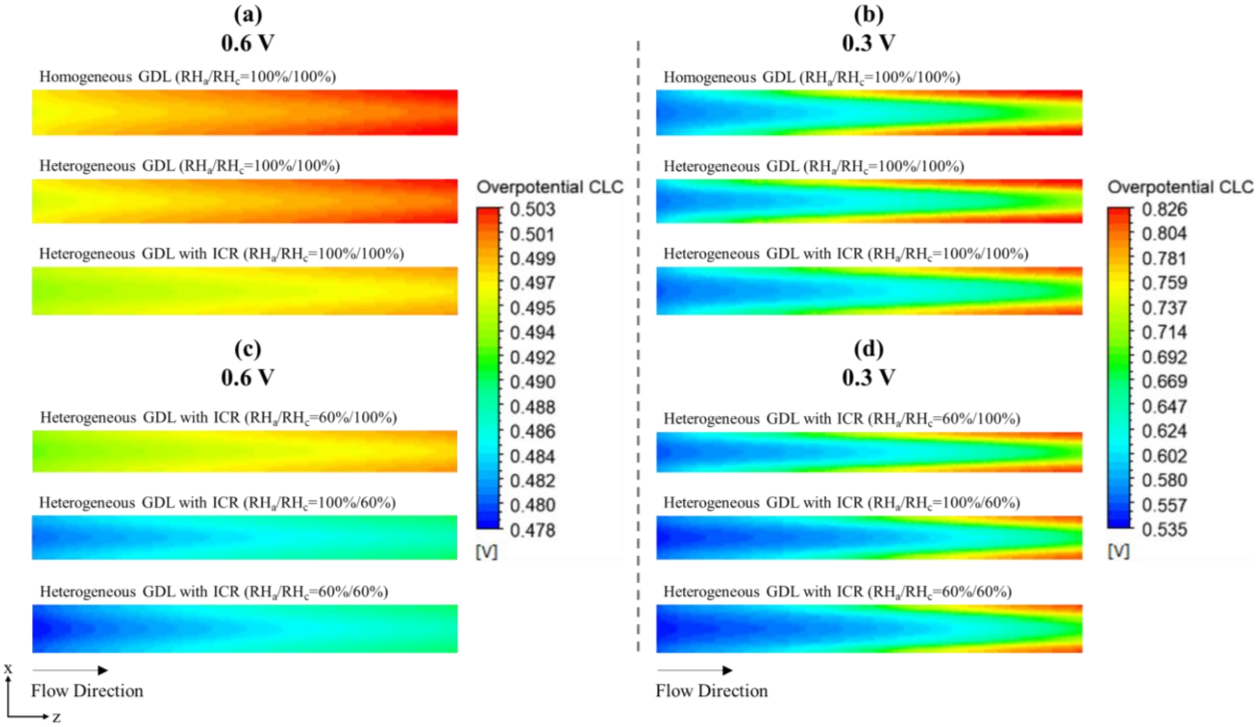

Figure 4.11 Cathodic overpotential in midsection of cathode catalyst at: (a) 0.6 V with full humidification, (b) 0.3 V with full humidification, (c) 0.6 V with different humification, (d) 0.3 V with different humifications

Figure 4.11 shows cathodic overpotential, which could be interpreted from O_2 mass fraction in cathode catalyst layer (see, Figure 4.6) or quite roughly from O_2 mass fraction in cathode GDL as in Figure 4. The difference in overpotential at 0.6 V for all cases is not very high, and the overpotential is around 0.47 to 0.5 V. This changes at higher load, where the difference is not only high (0.535 to 0.826) but also highly inhomogeneous from inlet to outlet. Nonetheless, overpotential may not be used to describe or interpret performance variation in the cell, at least numerically. This is because, though the performance curve of the homogenous case, as shown in Figure 4.2(a), is higher, Figure 4.11 shows higher values of overpotential for the homogenous case among all the other cases. Similarly, $RH_a|RH_c$ = 100%|60% case exhibits higher performance as in Figure 4.2(b), but $RH_a|RH_c$ = 100%|100% shows lowest cathodic overpotential as in Figure 4.11.

Overall, out of all cases with GDL heterogeneities, $RH_a|RH_c$ = 100%|60% exhibits higher performance compared to any other case, majorly due to reasonable consumption of H_2 and O_2 reactants (leading in enhanced HOR and ORR), increased local current density, the optimum water content in membrane, and lower water mass fraction at the cathode catalyst.

4.4 Summary

A numerical study is performed to investigate the combined influence of inlet relative humidity and ICR on the performance of single-channel PEFC with GDL flow/electrical heterogeneities. This study considers a multiphase steady-state computational model to investigate the homogeneous and heterogenous GDL. The study cases are evaluated for the cell performance, distribution of reactants, local current density, water mass fraction, temperature, and cathodic overpotential.

As compared to the conventional homogeneous model, flow/electrical heterogeneity in GDL reduces the performance by ~4.4% (at 0.3 V) with full inlet humidification. Full anodic and partial cathodic inlet humidification (i.e., $RH_a|RH_c$ = 100%|60%) is observed to increase the performance by ~19.2% at 0.3V. The H_2 and O_2 reactants show a lower mass fraction gradient from inlet to outlet at lower voltages with reasonable consumption from higher to lower voltages, indicating increased activity of HOR and ORR for heterogeneous GDL with $RH_a|RH_c$=100%|60%. Nominal (not high and not low) water content distribution in the membrane is observed at higher loads for heterogeneous GDL with ICR at $RH_a|RH_c$=100%|60% due to increased reaction kinetics, and this may have been one of the reasons for enhanced cell performance. Further, under partial cathodic humidification at higher loads, the temperature distribution in the membrane is found to reduce to ~350 K with heterogeneous GDL cases, possibly due to water production due to increased ORR.

Interestingly, it is observed that anodic humidification has less impact on the temperature distribution. Anode inlet humidity has no direct impact on water concentration in cathode catalyst layer. Interestingly, the increase in water concentration at higher loads in fully humidified cathode cases is comparatively much less than in partially humidified ones. Cathodic overpotential may not be an indicator of cell performance, or in other words, it fails to explain the reasons for losses or gains in performance. Table 4.5 outlines the comparison of the present study with literature of similar interest.

Table 4.5 Comparison of this study with literature

Source	**Outcome/Claims**
Current Study	Effect of electrical/flow heterogeneity of GDL under different inlet humidification is simulated
	Heterogeneity lead to ~4.4% reduction in current density (from ~1.2A/cm^2 to ~1.15A/cm^2) under full humidification
	~19% increase in current density (from ~1.1A/cm^2 to ~1.3A/cm^2) is observed with RHa|RHc=100%|60%
Hottinen et al. (2007)	The effects of both homogeneous and heterogeneous GDL on mass and charge transfer in PEFC. Findings demonstrated that heterogeneous GDL greatly impacts the local current density due to changing interfacial contact resistance, affecting the cell's performance.
Padavu et al. (2021)	Studied the effects of heterogeneous GDL in depth-dependent flow channels. Results indicates the heterogeneous GDL has a little lower performance than homogeneous GDL, which may be attributable to a more efficient hydrogen oxidation reaction and a decreased oxygen reduction reaction.
Akiki et al. (2012)	The local varying fields of GDL porosity and permeability result in varying ICR deducing the polarization curves.
Emmanuel et al. (2018)	The higher RH at the anode helps increase the performance of fuel cells, whereas, at higher current density, lower RH at the cathode is recommended to enhance the PEMFC performance.
Zhou and Wu (2007)	Numerically assessed that effects of heterogeneous compression is higher at higher RH leading to lower performance.

4.5 Closure

This chapter describes how the electrical and flow heterogeneity of GDL and full humidification at the anode, and partial humidification at the cathode led to the best PEFC performance. The subsequent chapter describes evaluating multichannel PEFC performance for endplate plate configurations previously considered.

CHAPTER 5

COMPUTATIONAL ANALYSIS OF 25cm^2 ACTIVE AREA PEFC WITH HETEROGENEOUS GAS DIFFUSION LAYER

5.1 Introduction

This chapter explores the transport characteristics and cell performance evaluation of the two single-cell PEFC clamping designs investigated in chapter 3. It is reported in chapter 3 that the use of an additional clamping plate (clamping 2) resulted in a more uniform distribution of various properties in different PEFC components compared to the clamping 1 design. The selection of GDL material models is crucial for quantifying bulk and interface properties, as was described earlier. In addition, it has been found that the influence of clamping endplate design might be easily misconstrued without nonlinear models for GDL.

This work entails considering GDL as a compressible material model (which is more realistic) and evaluating transport characteristics and PEFC performance. The properties obtained in GDL, such as interfacial contact resistance, porosity, and permeability, are retrieved from the chapter 3 study and developed further in this work.

5.2 Computational model description

Figure 5.1 depicts a schematic representation of the three-dimensional multichannel geometrical model analyzed in this work. ANSYS Fluent tool is used to carry out the analysis.The geometric model's description is the same as presented in Chapter 3, which is considered a 25cm^2 active area. However, parameters such as interfacial contact resistance at the interface of BPP|GDL and bulk properties of GDL (porosity and permeability) obtained in the chapter 3 study for both clamping designs are extracted to advance further in this investigation. This numerical model considers the same operational conditions and parameters as Chapter 4. In this study, however, the relative humidity at the anode and cathode inlets is considered 100% ($RH_a|RH_c$ = 100%|100%). Multiphase, steady-state, isothermal, perfect gas mixture, and laminar flow are the presumptions underlying this investigation. Material properties in the membrane and anode/cathode catalyst layer are assigned as homogeneous and isotropic.

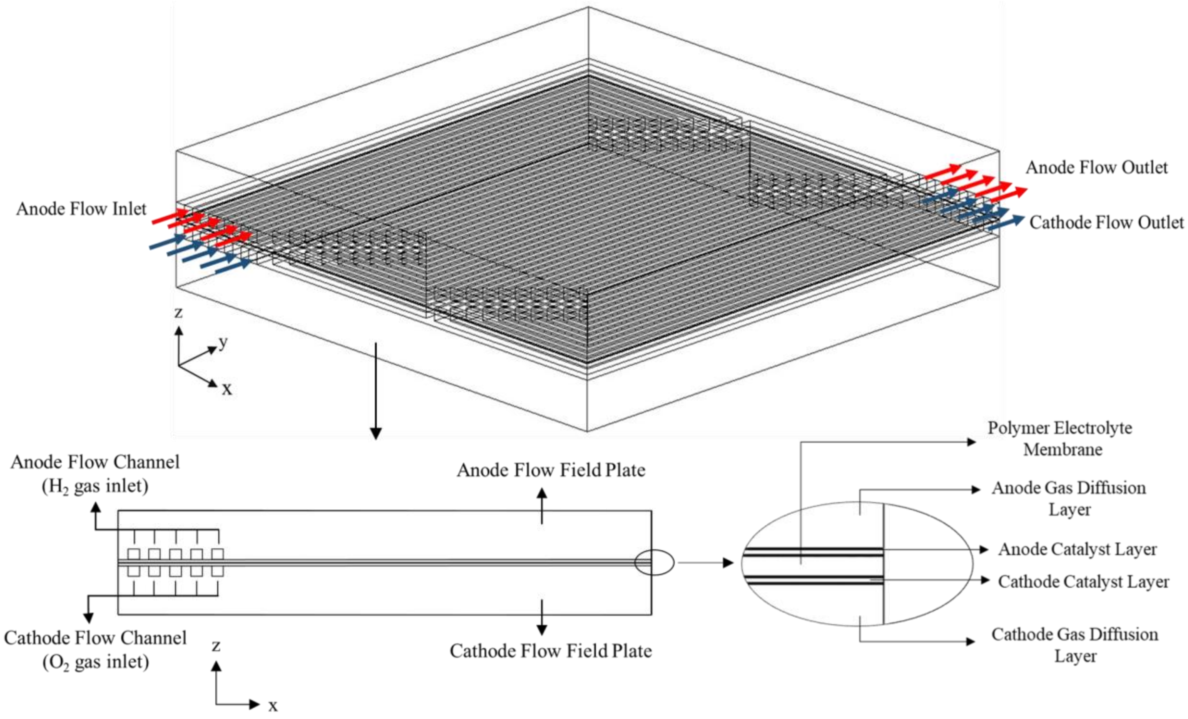
Anode Flow Inlet
Anode Flow Outlet
Cathode Flow Outlet
z
y
x
Anode Flow Channel
(H_2 gas inlet)
Anode Flow Field Plate
Polymer Electrolyte Membrane
Anode Gas Diffusion Layer
Anode Catalyst Layer
Cathode Catalyst Layer
Cathode Gas Diffusion Layer
Cathode Flow Channel
(O_2 gas inlet)
z
x
Cathode Flow Field Plate

Figure 5.1 Schematic illustration of multichannel PEMFC with an active area of 25cm^2

This study employs the same set of governing equations, liquid water transport models, dissolved phase models, inlet velocity equations, and boundary conditions as Chapter 4's single-channel fluent analysis

Figure 5.2 depicts the meshed model configuration taken into account in the present investigation. The meshed model is composed of a hexahedral mesh, and the anode flow field plate has been suppressed to display the flow channel mesh geometries. The computational domain is comprised of five multichannel flow channels (at both the anode and cathode), two GDLs, two catalysts, and a PEM membrane. The meshed model has a grid size of 55 grid points in the through-plane direction (z-axis), 5 grid points for flow channels and flow field ribs (x-axis), and 250 grid points each in x and y axes.

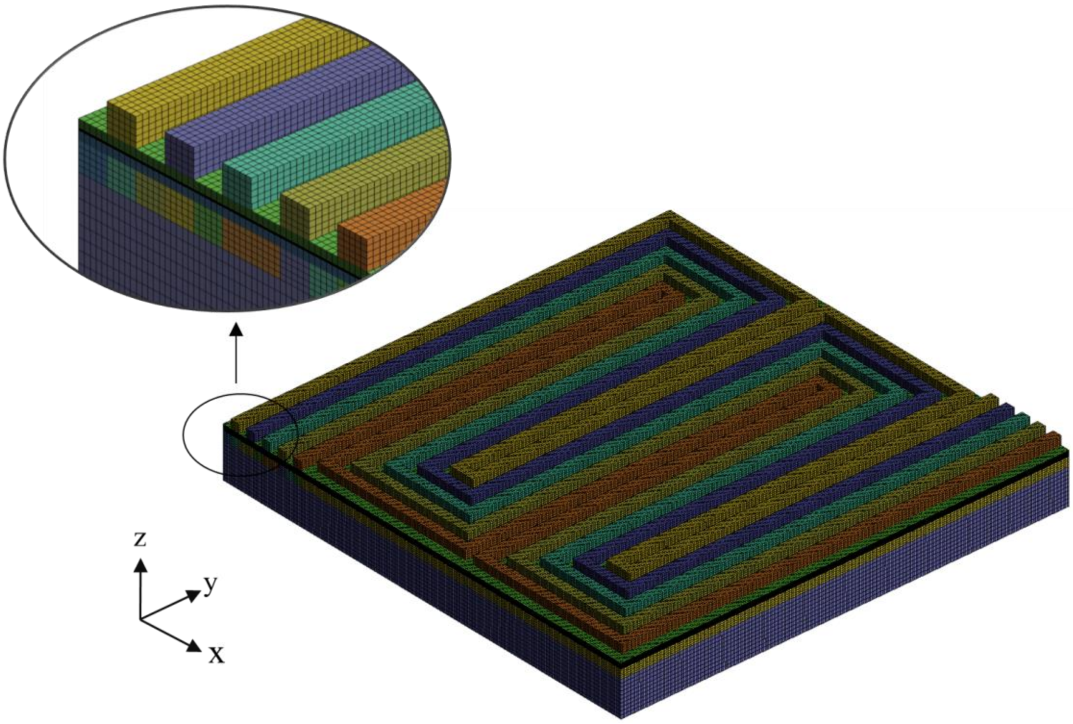

Figure 5.2 Computational mesh model of PEMFC

5.3 Results and Discussion

5.3.1 Cell Performance

Figure 5.3 depicts the cell performance for the two clamping designs. When the voltage of the cell is greater than 0.45V, the average current densities of the designs coincide. Due to a more uniform distribution of properties in GDL (as discussed in chapter 3), C2 design configuration is said to provide higher cell performance compared to C1 design. C1 and C2 designs have average current densities of 1.21 A/cm^2 and 1.25 A/cm^{2,} respectively, at a cell voltage of 0.2V. In addition, the power density curves for the two designs, given in Figure 5.3, reveal that the highest power density occurs at a cell voltage of 0.2 V, with the C2 design offering a higher value than C1. In the following sections, the hydrogen mass fraction, oxygen mass fraction, local current density, water mass fraction, and temperature distribution are described in detail to investigate the effects of two design cases on local transport characteristics.

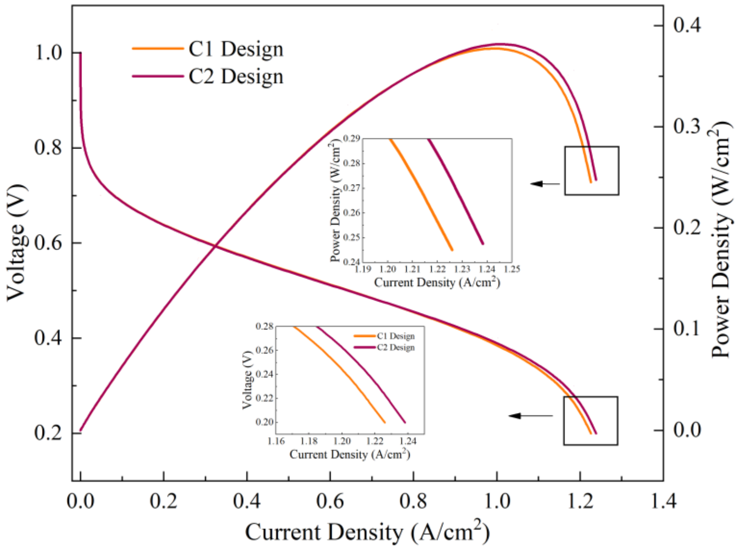

Figure 5.3 Performance of the PEMFC for C-1 and C-2 design

5.3.2 Hydrogen mass fraction distribution

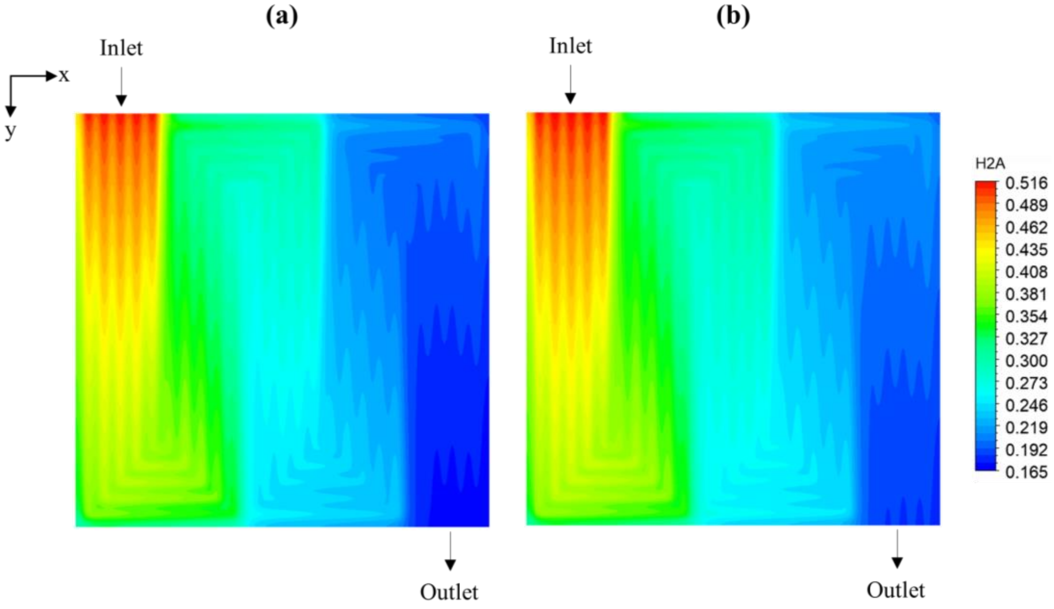

Figure 5.4 Hydrogen mass fraction distribution in mid-section of anode GDL at 0.3V for (a) C-1 design; (b) C-2 design

Figure 5.4 depicts the H_2 mass fraction distribution in the midsection of anode GDL at 0.3V cell voltages for both clamping mechanisms. A higher H_2 mass fraction implies a higher hydrogen oxidation reaction (HOR). Figure 5.4 demonstrates that the distribution of hydrogen is higher at the inlet and decreases throughout the serpentine flow channel towards the outlet—the better the performance of PEFC, the greater the diffusion of reactants. Figure 5.4 demonstrates that the C2 design gives a slight increase in hydrogen mass fraction distribution from inlet to outlet compared to the C1 design. At the inlet, the maximum H_2 mass fraction for the C1 and C2 designs is 0.501 and 0.516, respectively, while at the outlet, it is 0.165 and 0.192. Thus, it is evident that the C2 mechanism allows for more diffusion of reactants from the inlet to the output, which may be one of the factors contributing to the enhanced performance of the PEFC.

5.3.3 Oxygen mass fraction distribution

The distribution of the O_2 mass fraction in the midsection of the cathode GDL at 0.3V for the two-clamping design configuration is depicted in Figure 5.5. The oxygen mass fraction decreases from inlet to outlet in both clamping design cases, indicating the consumption of reactants. In other words, at higher current densities, electrochemical reactions accelerate, consuming a higher amount of oxygen reactants. Moreover, the lower oxygen availability indicates an insufficient oxygen reduction reaction (ORR), which reduces the cell's performance. Compared to the C1 design, the C2 design provides a higher distribution of reactants from the inlet to the outlet, indicating a greater ORR. It is reported that C1 and C2 provide a maximum oxygen mass fraction of 0.099 and 0.106, respectively, while at the outlet, it is 0.008 and 0.016 along the channel. Compression of the flow field rib region causes insufficient reactions, resulting in the availability of lower reactants outside the flow channel path. Consequently, this increase in ORR in the C2 design may contribute to the likely improvement in cell performance.

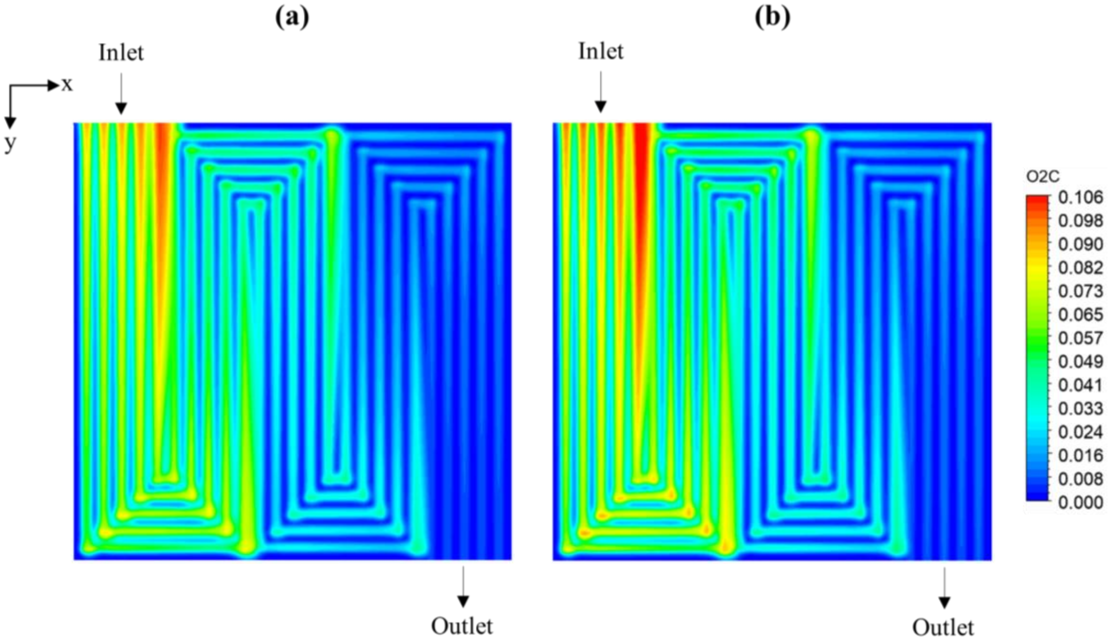

Figure 5.5 Oxygen mass fraction distribution in mid-section of cathode GDL at 0.3V for (a) C-1 design; (b) C-2 design

5.3.4 Local current density distribution

Figure 5.6 plots the local current density distribution in the mid-section of the membrane at 0.3V. The current density distribution exhibits the same trend as the oxygen mass fraction in all regions, as shown in Figure 5.5. It is visualised that the ribs between the adjacent channels function as electrical conductors. Rapid electrochemical reactions ensue from oxygen in the channel region, leading to the current generation. As illustrated in Figure 5.6, the availability of reactants is lower beneath the rib than in the channel, resulting in a decrease in current production under the rib. As depicted in Figure 5.5, both clamping designs demonstrate that a substantial amount of oxygen is available at the inlet, which will optimally promote the electrochemical process. It is observed that the local current density of the C2 design is higher than that of the C1 design, resulting in a likely improvement in cell performance.

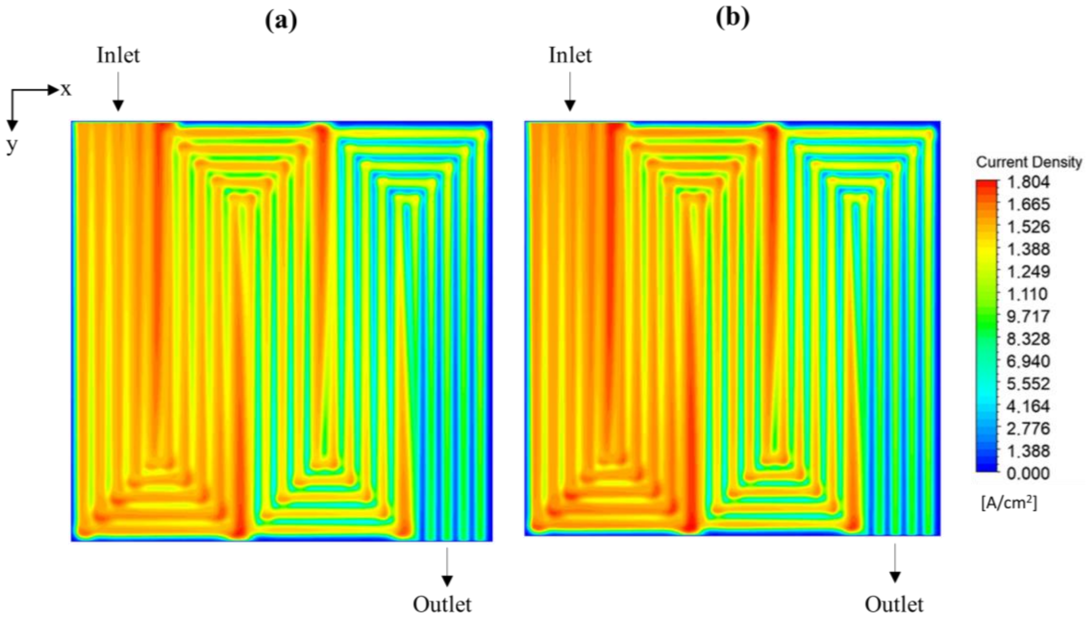

Figure 5.6 Local current density distribution in mid-section of membrane at 0.3V for (a) C-1 design; (b) C-2 design

5.3.5 Water content distribution

The water content distribution in mid-section of membrane at 0.3V for C1 and C2 design is as illustrated in Figure 5.7. It is well known that an excess membrane water content can result in cathode flooding, while a low membrane water content dries the membrane. Consequently, water management of membrane during PEFC operation is crucial (Yinqi Shen 2017). From both clamping designs, Figure 5.7(a) and (b), it is evident that there is a slight change in the distribution of water content in the membrane. The maximum water content for the C1 design is around 8.909, whereas for the C2 design, it is 9.104. A slight increase in C2's water content may have increased protonic conductivity, resulting in improved cell performance.

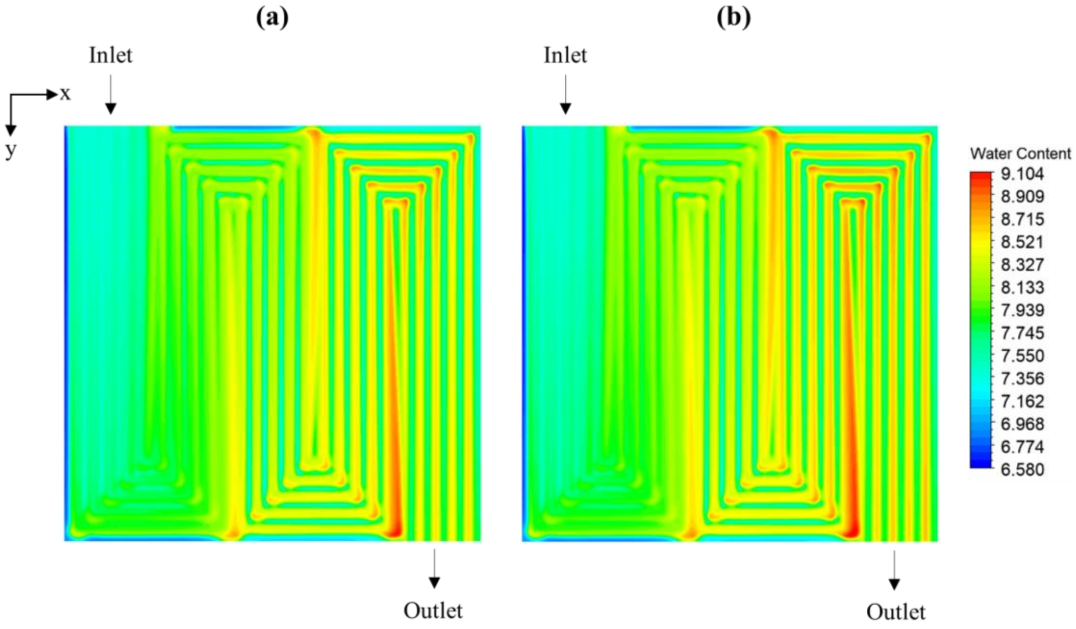

Figure 5.7 Water content distribution in mid-section of membrane at 0.3V for (a) C-1 design; (b) C-2 design

5.3.6 Temperature distribution

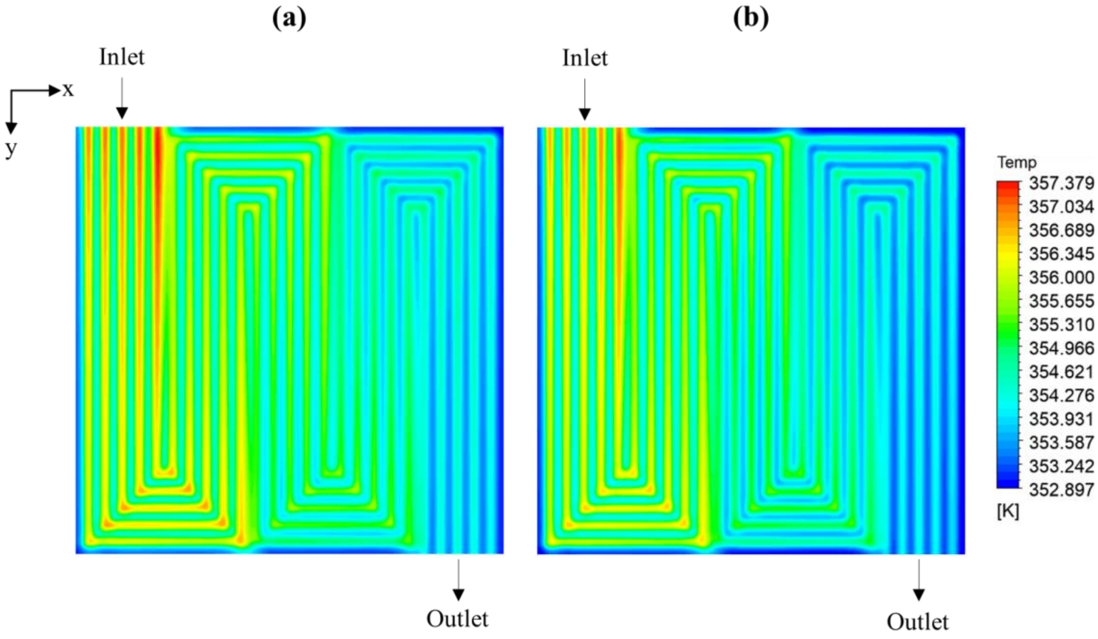

Figure 5.8 Temperature distribution in mid-section of membrane at 0.3V for (a) C-1 design; (b) C-2 design

Temperature is one of the significant factors influencing transport properties, electrochemical kinetics, and cell performance. The temperature distribution in the membrane's midsection is depicted in Figure 5.8. The temperature distribution plots show that the inlet temperature is greater than the outlet temperature. Due to the high thermal conductivity of the rib, the temperature below the flow field rib region is lower than that of the flow channel path. It is seen that the C2 design provides a lower temperature gradient from the flow channel's inlet to the outlet than C1 design. The maximum temperature for cases C1 and C2 is 357.38K and 357.05K, respectively, whereas the minimum temperature is nearly the same at 353.5K. It provides adequate surface area for electrochemical processes to occur at the surface, which may result from the uniform distribution of mechanical, electrical, and flow properties in the C2 design. This observed low-temperature gradient in C2 may have contributed to the improvement in cell performance.

5.3.7 Water mass fraction distribution

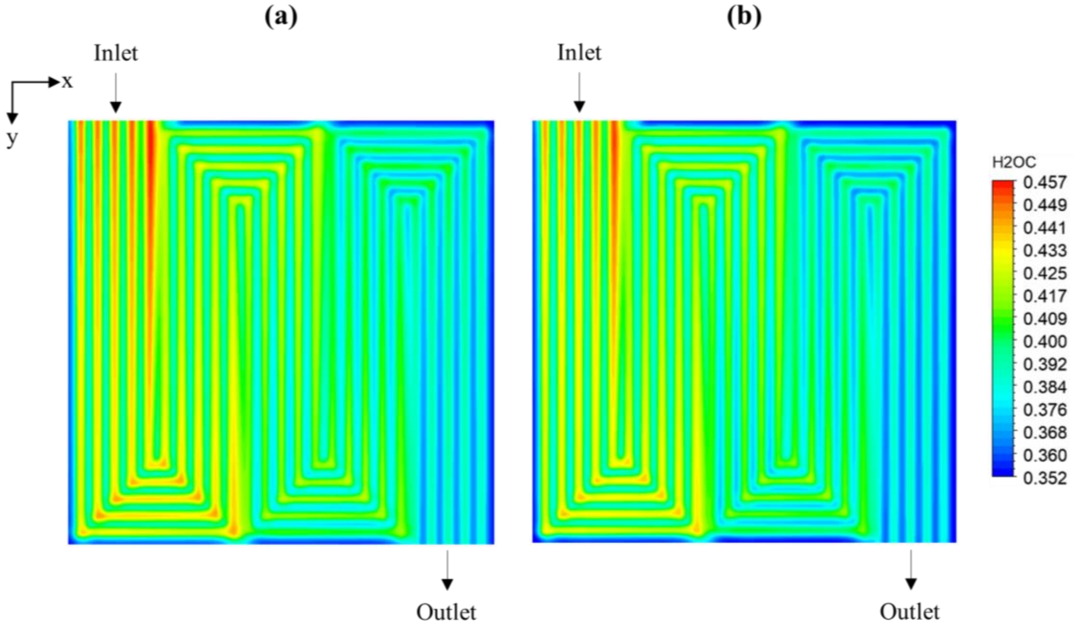

Figure 5.9 Water mass fraction distribution in mid-section of cathode catalyst at 0.3V for (a) C-1 design; (b) C-2 design

Figure 5.9 illustrates the distribution of the water mass fraction in the midsection of the cathode catalyst at 0.3V for the two clamping designs. Hydrogen and oxygen reactants are consumed in the electrochemical reaction, producing water as a byproduct. The C2 design is observed to have a lower water mass fraction distribution than the C1 design. The maximum water mass fraction for case C1 is 0.457, while the maximum water mass fraction for case C2 is 0.430. Even if the values differ marginally, this may have been one of the contributing elements to improving PEFC performance. Higher water mass fraction at the cathode may cause flooding of the gas channels, preventing the entry of new reactants for further electrochemical reactions, decreasing cell performance. Since the C2 design has a lower water mass fraction, it is evident that it improves the cell's performance.

5.4 Summary

This study uses a multichannel, three-dimensional PEFC numerical model with a 25cm2 active area to analyse transport characteristics and cell performance for the two clamping mechanisms discussed in chapter 3. This work uses a multiphase steady-state computational model to analyse the heterogeneous properties of GDL acquired in chapter 3 in order to assess transport characteristics. The properties of GDL, including interfacial contact resistance, porosity, and permeability, are retrieved from the chapter 3 study and further developed in this work. Due to the efficient reaction of the reactants, this study reveals that the C-2 design gives better cell performance than the C-1 design. It is suggested that the increased amount of oxygen reactants led to a rise in oxygen reduction reaction (ORR), which in turn increased the local current density. The availability of higher water content in the membrane results in higher protonic conductivity is also explored. The lower temperature distribution in the membrane further emphasized the cause for higher PEFC performance, due to adequate surface area for electrochemical reactions to occur at the surface for the C2 design. In addition, a lower water mass fraction at the cathode may prevent flooding of the gas channels, thereby allowing the entry of fresh reactants to accelerate electrochemical processes and enhance cell performance. Table 5.1 summarizes the current study with literature of the similar work.

Table 5.1 Comparison of the present study with literature

Source	Outcome/Claims
Current Study	The efficient reaction of the reactants reveals that the modified clamping design offers better cell performance than the conventional clamping design.
	Study reveals the increased amount of oxygen reactants led to a rise in oxygen reduction reaction (ORR), which in turn led in enhancing the local current density.
Wang et al. (2016)	Heterogeneous compression has an adverse effect on the concentration of reactants and cell performance. However, it is illustrated that better performance can be achieved by applying optimum clamping force.
Yan et al. (2020)	The heterogeneous compression of GDL helps in thermal management. It thus decreases the average temperature at the cathode catalyst layer and lowering the maximum temperature to avoid local hotspots.
Zhou et al. (2006)	Uniform contact pressure distribution leads to minimum ICR, which is necessary to optimize the fuel cell unit.

5.5 Closure

This chapter reveals that the performance of the proposed endplate configuration is better than that of the conventional endplate arrangement of a single-cell PEFC due to more uniform electrical and flow properties. The subsequent chapter details an experimental evaluation of the cyclic mechanical response of GDL with and without MPL at various temperatures and pre- and post-hotpress conditions.

CHAPTER 6

INVESTIGATION OF CYCLIC MECHANICAL RESPONSE OF GDL

6.1 Introduction

As is well known, the GDL is crucial to the efficient operation of polymer electrolyte fuel cells (PEFCs). This component uniformly distributes reactants to the reaction sites and possesses excellent structural durability. (Morgan and Datta 2014; Ozden et al. 2019; Yarar Kaplan et al. n.d.). In general, the GDLs are subjected to pre-assembly hot press pressure and in-situ micro-cyclic loadings induced due to cell operating conditions (start-up/shutdown or hygrothermal cycle) (Bouziane et al. 2020; Carral and Mele 2022; Silberstein and Boyce 2010). As the durability of this layer is directly proportional to its structural resilience, it is highly desirable to investigate the structural response under situations similar to cell operation.

GDLs are often not installed directly in fuel cell units. Prior to cell integration, the GDL undergoes a hot-press pre-assembly fabrication technique to build an assembly with PEM. Although the pre-assembly properties of GDLs are mostly well documented, the post-fabrication response is yet to be fully explored. In order to explore the temperature response of GDL (with and without MPL) and the pre-assembly hot-press effect, experimental schemes are proposed in this chapter.

6.2 Experimental Details

The commercially available GDL (here SGL Carbon -Sigracet 39BC series (“Powering up fuel cells” n.d.)) and GDL (here Toray Carbon Paper (“Toray Carbon Paper TGP-H-060 |” n.d.)) material are carefully cut into 1cm×1cm size samples. A number of such samples stacked together for compressive cyclic testing. Figure 6.1 shows the experimental setup at room temperature (Figure 6.1(a)) and at different temperature (Figure 6.1(b)). Both samples are subjected to these schemes. Figure 6.1(c) shows cyclic compressive loading of the samples at different temperatures, i.e., 22°C, 55°C, and 80°C.

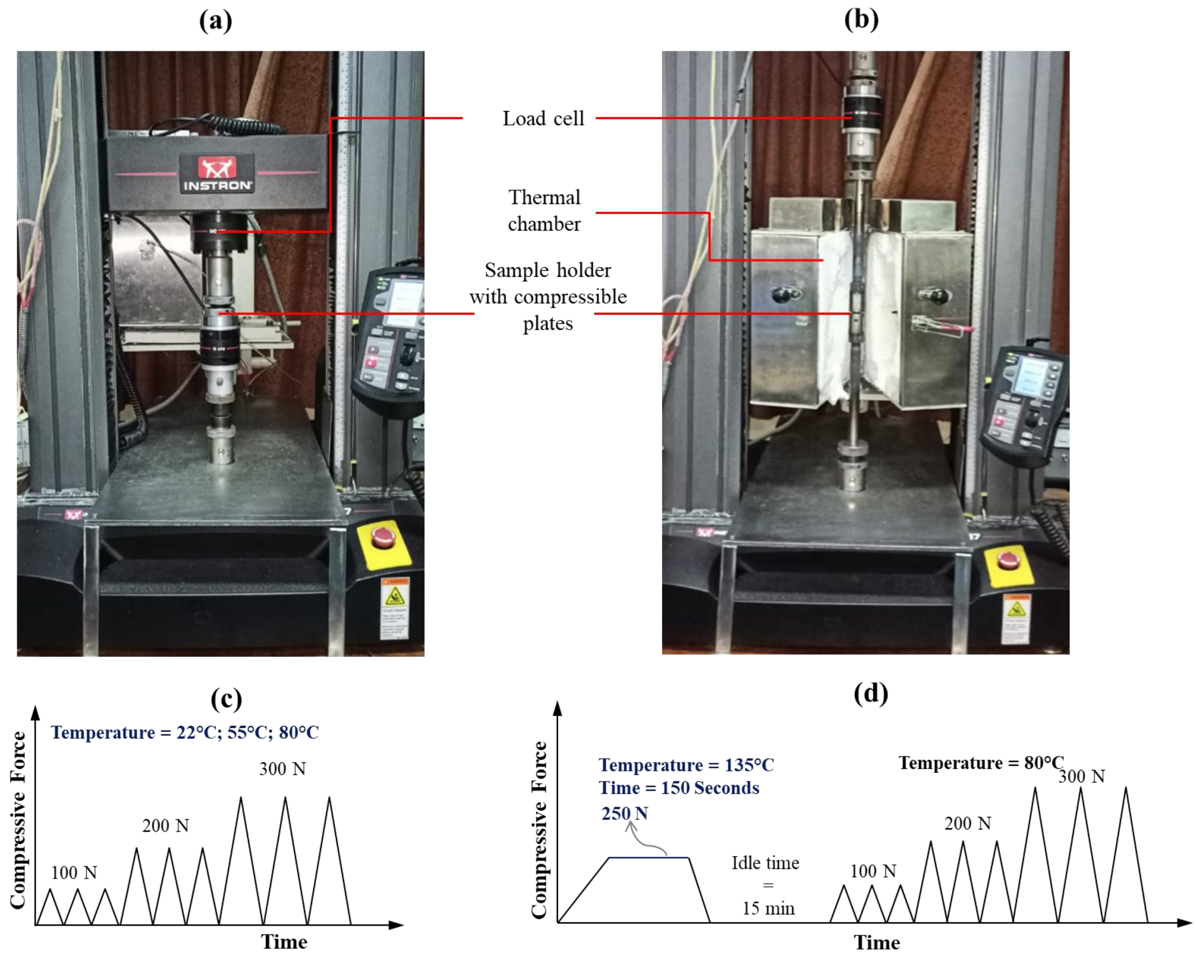
(a)
(b)
INSTRON
Load cell
Thermal chamber
Sample holder with compressible plates
(c)
Compressive Force
Temperature = 22°C; 55°C; 80°C
100 N
200 N
300 N
Time
(d)
Compressive Force
Temperature = 135°C
Time = 150 Seconds
250 N
Idle time = 15 min
Temperature = 80°C
100 N
200 N
300 N
Time

Figure 6.1 Experimental setup at (a) room temperature; (b) different temperature; (c) pre hot- press condition; (d) post hot-press condition

There is no exerted pre-load of any sort until the environmental chamber reaches the set temperature. The sample was then equilibrated with a set temperature for some initial duration before applying the pre-load of 5N. As shown, the samples are subjected to repetitive cycles at four force levels, i.e., 100N, 200N, 300N, and 400N. At each force level, the compressive cycle is repeated three times. Figure 6.1(d) shows the experimental scheme that imitates the operational conditions of the pre-assembly hot-press and post-assembly cell. Thus, the scheme is divided into a 2-stage cycle. In the 1st stage, the samples are subjected to a hot-press cycle, i.e., temperature 135°C; pressure 2.5MPa; and time=3 minutes. This is followed by the post-assembly cycle, which includes a compressive cyclic pattern, the same as Figure 6.1(a) but under 80°C. All tests are performed at a low strain rate using the 3kN capacity INSTRON universal testing facility at the Indian Institute of Science in Bangalore, India.

6.3 Models and Analysis

6.3.1 Linear Regression Analysis

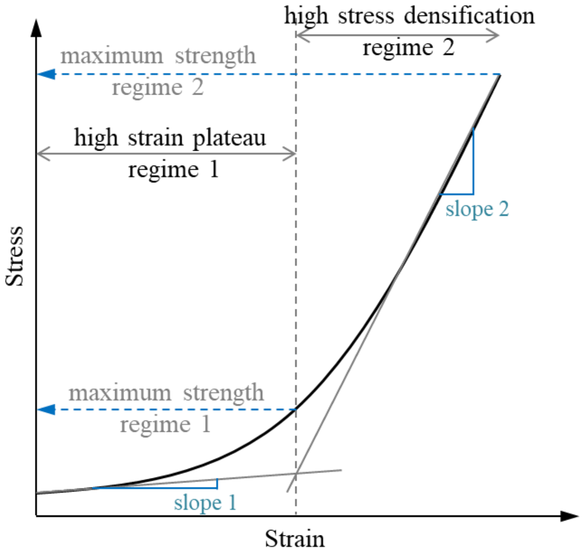
high stress densification
regime 2
maximum strength
regime 2
high strain plateau
regime 1
slope 2
Stress
maximum strength
regime 1
slope 1
Strain

Figure 6.2 Linear regression analysis using Qualitative analysis

This approach may not reveal the influence of constituents on the observed changes in the experiment. Nonetheless, this will provide a qualitative understanding of variations in basic properties such as stiffness and resilience. As shown in Figure 6.2, the likely response will be divided into two regimes. The 'regime-1 plateau corresponds to a high-strain response under near-constant load. The 'regime-2' corresponds to densification zone with high load response at low strain. The stiffness is measured as the slope of these regions. The material's resilience is determined by comparing its strength to its stiffness. In order to acquire comparable data, the strength is measured at a specific load.

6.4 Results and Discussion

6.4.1 Mechanical response at various temperature

Figure 6.3 demonstrates the cyclic mechanical response of GDL with and without MPL at three temperature limits. It is observed from the plots that GDL with MPL shows a significant strain response with a low resistance to force (Figure 6.3(a)), whereas the layer without MPL exhibits higher stress-to-strain ratio (Figure 6.3(b)).

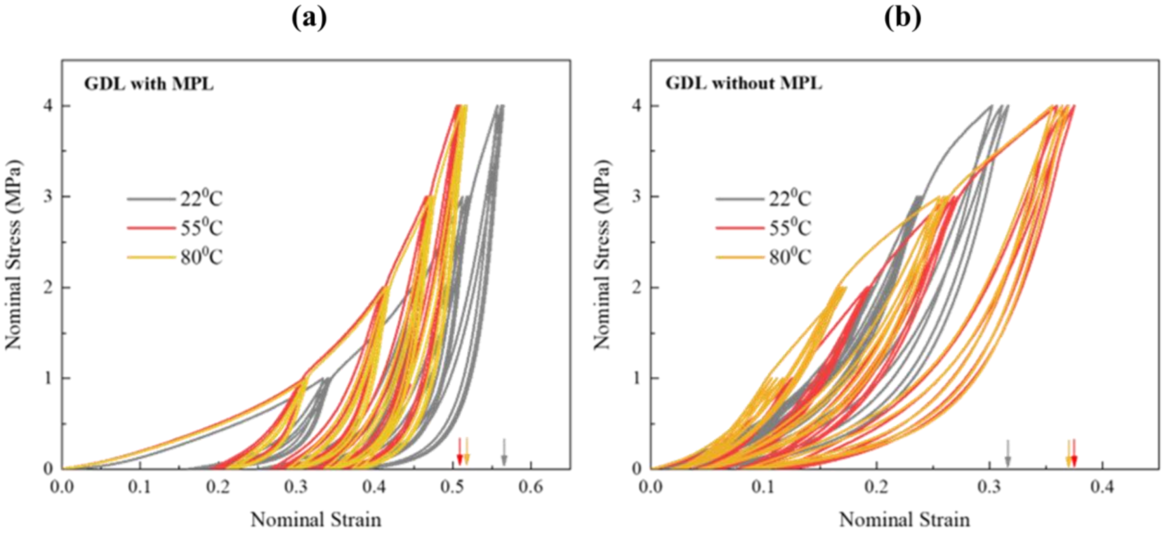

Figure 6.3 Mechanical Response at different temperature for (a) GDL with MPL, (b) GDL without MPL

MPL plays a critical role here as its particles intrude into the GDL; the matrix becomes more compliant and hence offers less stiffness to load. In the absence of MPL, the load bearing capacity is only through resin matrix and fibers. Another important observation is made in terms of the effect of elevated temperature. In both materials, the influence of temperature on the cyclic response is almost negligible. GDL with MPL shows slightly improved stress-to-strain ratio as a function of increased temperature. This is counter-intuitive. This slight variation is explained by the softening of the matrix domain due to increased temperature, and the stress applied is readily borne by the fiber fraction.

Further, it is noted that the presence of MPL contributes to a larger residual strain upon unloading (Figure 6.3(a)). In the case of carbon paper, however, one can observe near-elastic unloading (Figure 6.3(b)). At the end of load-unloading cycles, the residual strain stands at 10% and 2%, respectively, for GDL with MPL and without MPL. In the above case, the GDL was subjected to no prior treatment, and the material was as-received. However, hotpress conditions present a realistic understanding of these materials for the mechanical response.

6.4.2 Effects of pre- and post-hotpress condition

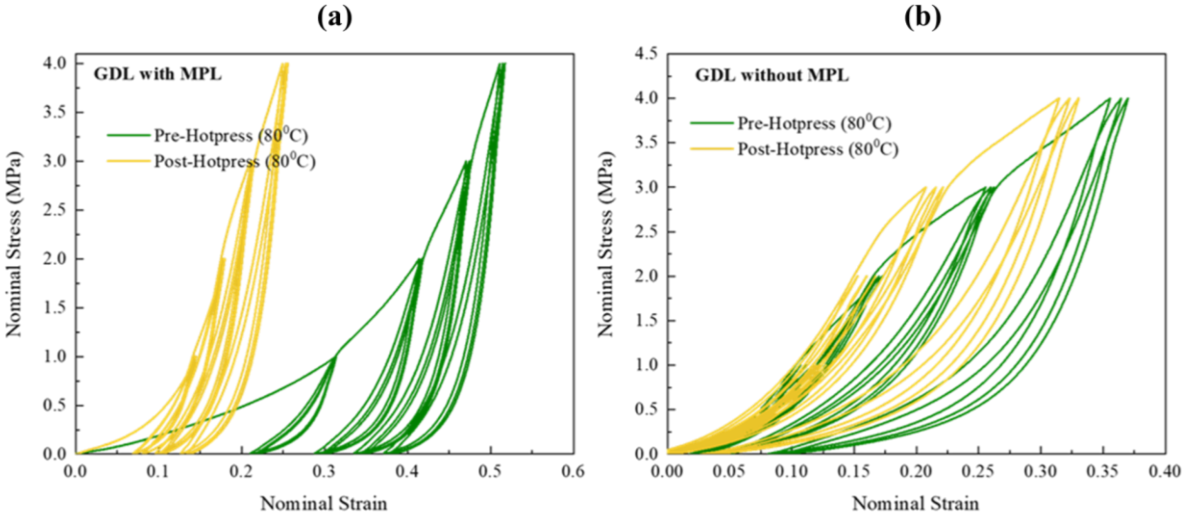

Figure 6.4 Effects of pre and post hot press for (a) GDL with MPL, (b) GDL without MPL

Further, Figure 6.4 shows the influence of hot-press on both of the materials. Strikingly but understandably, the GDL with MPL (Figure 6.4(a)) shows remarkable variation in the mechanical response with an almost 120% increase in stress-to-strain ratio with the post-hotpress condition. It is clear that the hotpress pressure played a vital role since hotpress temperature might not be a huge contributor to this variation, as its negligible influence on the mechanical response is evident from Figure 6.3. The pressure, in this case, might have induced residual strain at the end of hotpress procedure, and the effect might have carried on to influence the observed post-hotpress response. Figure 6.4(a) also highlights the substantial influence of hotpress in the variation of residual strain from 10% to 3.75% at the end of 4th load-unload cycle. Interestingly, on the other hand, the carbon paper response, as shown in Figure 6.4(b), is relatively unchanged. There is a slight variation in the stress-to-strain ratio at higher stress levels, but there is also no significant variation. Therefore, it is now evident that the presence of MPL significantly affects the pre- and post-hotpress responses of GDL material.

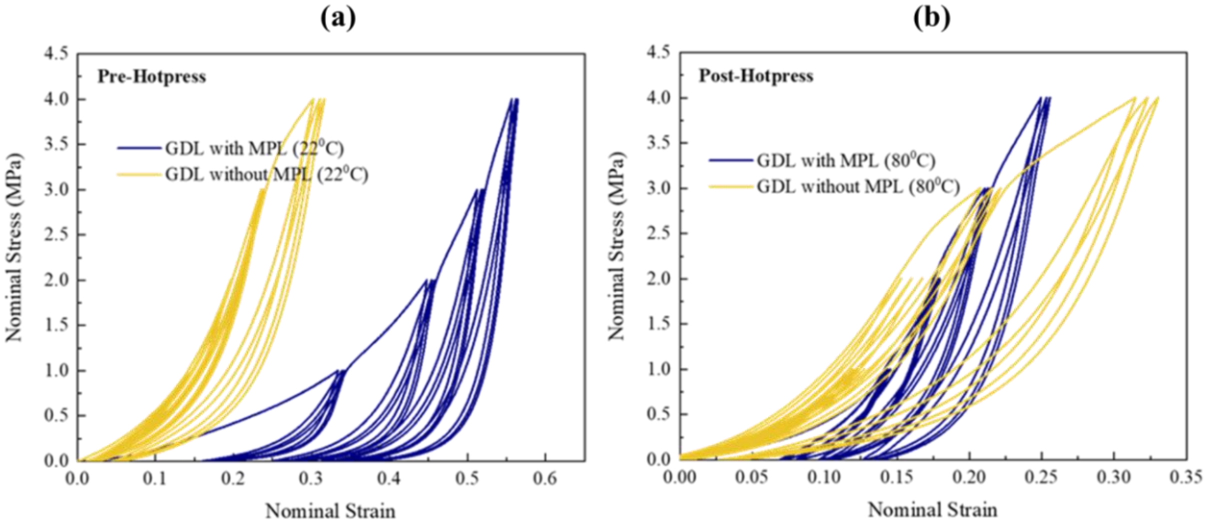

Figure 6.5 Effects of GDL response for (a) Pre-Hotpress condition; (b) Post-Hotpress condition

Figure 6.5 depicts the GDL materials with and without MPL under pre- and post-hot-press conditions at temperature 22°C and 80°C. As illustrated in Figure 6.5(a), pre-hotpress condition GDL without MPL exhibits a higher stress-to-strain ratio than GDL with MPL at 22^0C. It is evident that GDL with MPL reduces strain response by approximately 110 percent. Also, significant residual strain is observed with MPL cases during unloading, whereas cases without MPL show low residual stresses. Consequently, in the post-hot-press state at 80^0C, as shown in Figure 6.5(b), there is no significant difference between the two GDL materials; nevertheless, GDL with MPL exhibits a slight rise in stress-to-strain ratio with reasonable residual strain in each unload scenario. Consequently, it is evident from Figure 6.5 that hot-press pressure plays a crucial role in the mechanical reaction of both GDL materials.

6.4.3 Compressive strength

Figure 6.6 illustrates the compressive strength of GDL with and without MPL under pre- and post-hot-press conditions. Compressive strength indicates the GDL material's resistance to external compressive loads. As shown in Figure 6.2, regime 1 relates to a high strain response at constant load, whereas regime 2 corresponds to a high load response at low strains. Figure 6.6 demonstrates that the pre-hotpress state of both GDL materials is lower than its post-hotpress condition. Moreover, it is noted that the post-hotpress case for GDL with MPL leads to a nearly 600% increase in compressive strength in regime 1, while there is a 200% increase in regime 2.

Consequently, the GDL with MPL under post-hot press varies significantly. Due to the absence of the MPL layer, Toray paper exhibits no substantial change in compressive strength post-hot press condition. Only resin matrix and fibers contribute to the limited load-bearing capability. Consequently, it is evident that the presence or absence of MPL significantly impacts the compressive strength of GDL materials.

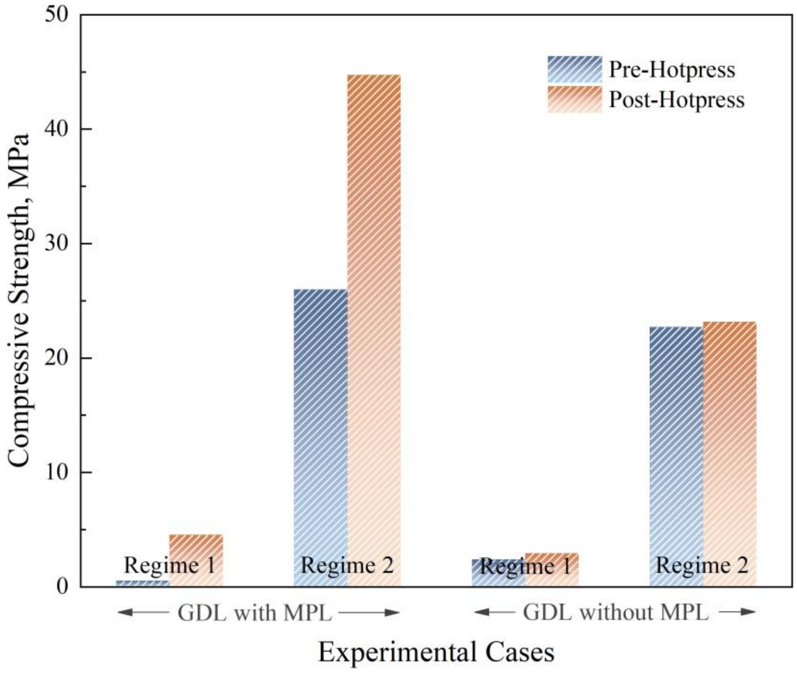

Figure 6.6 Compressive strength of GDL materials under pre- and post-hotpress conditions

6.4.4 Elastic resilience

Figure 6.7 depicts the elastic resilience of GDL with/without MPL during pre- and post-hotpress conditions. In GDL, elastic resilience is the capacity of a material to absorb energy when elastically deformed and release it when unloaded. Figure 6.7 demonstrates that the resilience decreases nearly 600% in regime 1 and about 200% in regime 2 for GDL with MPL. It is clear that post-hotpress depicting the actual PEFC operating conditions show significant variation in elastic resilience when GDL with MPL is taken into consideration. Consequently, GDL without MPL under post-hotpress show a slight variation in elastic resilience, which is negligible.

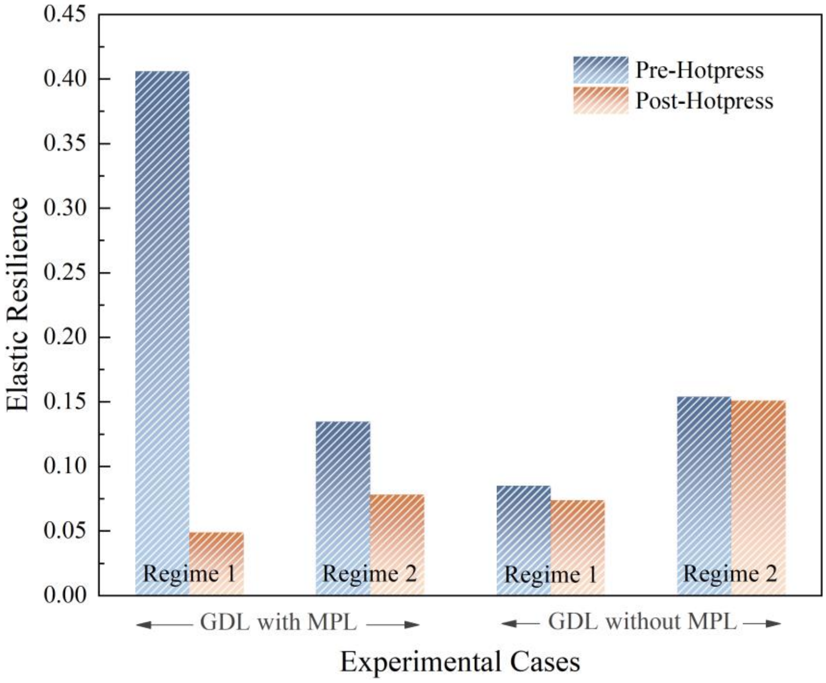

Figure 6.7 Elastic resilience of GDL materials under pre- and post-hotpress conditions

6.5 Summary

The effect of hot-press conditions, which comprise elevated pressure and temperature, is studied on the cyclic behaviour of gas diffusion media with and without a microporous porous layer (MPL). Hot-press is an integral part of the pre-assembly process for polymer electrolyte fuel cell (PEFC) and membrane electrode assembly fabrication (MEAs). The cyclic response of GDLs exposed to cell operational temperatures within 20°C to 80°C is investigated. Investigation of the cyclic mechanical response under pre- and post-hotpress conditions GDL materials is carried out. The study reports that the mechanical response of GDL with MPL varies significantly, with the stress-to-strain ratio increasing by approximately 120% post-hotpress. It is evident that the hotpress pressure had a crucial role, while the hotpress temperature may not have been a major contribution to this variation due to its insignificant impact on the mechanical response. In addition, when hot-pressed GDL with MPL is evaluated, the compressive strength increases by about 600 percent while elastic resilience reduces by a similar amount. It is also noticed that GDL without MPL offers slight variation under hot-pressed conditions.

Table 6.1 Comparison of the current study with literature

Source	Outcome/Claims
Current Study	The study reports that the mechanical response of GDL with MPL varies significantly, with the stress-to-strain ratio increasing by approximately 120% in post-hotpress condition.
	Under hot-pressed evaluation for GDL with MPL, the compressive strength increases by about 600% while elastic resilience reduces by a similar amount.
Zhang et al. (2020)	The contact pairs and pore space play an essential role in deciding the nonlinearity of the compressive curve is revealed. It is showed the average porosity decreases with increasing pressure in GDL, resulting in a non-uniform distribution of porosity in the through-plane direction.
Sadeghi et al. (2010)	Different values of GDL's Toray carbon paper such as geometric, mechanical, and thermal parameters reach a steady state after five loading-unloading cycles leading to no further changes.

6.6 Closure

This chapter contains information about the experimental investigation of the cyclic mechanical response of GDL with and without MPL under pre- and post-hotpress conditions. The results showed that GDL with MPL under post-hotpress conditions offered better stress-to-strain ratio compared to GDL without MPL. The next chapter discusses the development of a phenomenological constitutive model to predict the cyclic bulk electrical conductivity of GDLs.

CHAPTER 7

DEVELOPMENT OF PHENOMENOLOGICAL CONSTITUTIVE MODEL TO PREDICT CYCLIC BULK ELECTRICAL CONDUCTIVITY OF GDL

7.1 Introduction

GDL is a crucial functional component of PEM fuel cells, facilitating the efficient transport of reactants and providing mechanical stability. It is essential for the transfer of reactants to catalyst layers, water and heat management, and high electronic conductivity (Millichamp et al. 2015; Ozden et al. 2019; Wang et al. 2011). The influence of the deformation of these layers on the PEFC performance is a widely researched topic. This is because highly porous GDL deformation in the compression direction leads to variations in physical properties such as permeability, porosity, thermal and electrical contact resistance, and bulk resistance (Atyabi et al. 2019; Movahedi et al. 2018; Mukherjee et al. 2020; Omrani and Shabani 2019; Ouaidat et al. 2020; Qiu et al. 2017; Sow et al. 2015). These variations are often localized due to inhomogeneity in deformation (García-Salaberri et al. 2019; Khetabi et al. 2019; Li et al. 2019; Mahmoudi et al. 2016; Roy Chowdhury et al. 2016; Vikram et al. 2016; Yan et al. 2020).

In practice, relative humidity and temperature changes result in hygro-thermal stresses in GDL and membrane, causing a cyclic effect.(Kusoglu et al. 2006; Lu et al. 2011; Silberstein and Boyce 2011; Solasi et al. 2007). Since the operating conditions of PEFC cells induce cyclic effects, investigating the local cyclic response of the aforementioned properties is particularly important in understanding the performance limiting factors of PEFCs. Although there exist limited data on the experimental cyclic response of GDLs, a constitutive model that can be used to predict the in-situ local response under cyclic operating conditions is so far missing in the literature. In this study, a phenomenological constitutive model that can predict the cyclic ohmic response of GDLs under repetitive compressive loading is proposed.

7.2 Methodology

The proposed phase-dependent constitutive model is initially checked for monotonic and cyclic electrical conductivity experimental data. These sets of experimental data are taken from the literature (Ref. (Mason et al. 2012; Radhakrishnan and Haridoss 2010)) as detailed in the subsequent sections. The experimental data is available only for Toray paper with 5 to 30wt% PTFE loading (with no microporous layer (MPL)).

7.2.1 Model Development

The compression of GDL leads to a change in the physical and transport properties of the material. This is associated with the change in porosity, and the density of fiber interactions. This force sometimes results in fiber cracks leading to sudden variations in properties.

First, it is necessary to define this compression. Here, the change in ohmic resistance of GDL is assumed to be a function of porosity variation and the contact density between fibers. Hence the compressive ratio (ϕ) can be defined by a simple relation between the limits of compression as in Equation 7.1:

$$\phi = \left(\frac{\sigma_c}{\sigma_s} \right) \tag{7.1}$$

where σ_C signifies the applied compressive stress and σ_S represents the saturation limit upto which the GDL is compressed.

Now it is known from the literature that the relation between conductivity is nonlinear with compression (Mason et al. 2012; Qiu et al. 2018; Radhakrishnan and Haridoss 2010; Vikram et al. 2016). Hence the electrical conductivity of GDL is expected to vary exponentially due to compression that is limited here by saturation limit *(d)*. The following relation can give this:

$$K_{f(\sigma_c)} = 1 - e^{-(\phi)^d} \tag{7.2}$$

where $K_{f(\sigma c)}$ is the electrical bulk conductivity.

The electrical conductivity of GDL depends on its constituents. Hence, two constituent parameters are associated with the above conductivity equation. The '***C₁***' parameter is a dependent function of porosity (this being a mathematical term and is made inversely proportional to actual porosity in the current problem). The porosity varies with successive loading cycles, which phenomenologically correlate to the fiber and resin matrix density change. The second parameter is a function of contact density between carbon fibers (number of fiber contacts) and is represented by parameter '***C₂***'. Incorporating these parameters, a renewed equation for electrical conductivity is established:

$$\left(K_{f(\sigma_c)}\right)_l = C_1 + C_2\left(1 - e^{-(\phi)^d}\right) \tag{7.3}$$

It is noted that an increase in compressive stress reduces the porosity of the GDL and increases the internal fiber connection, which plays a significant role in higher electrical conductivity. The porosity parameter expressed as a porosity variation is illustrated in supplement Figure 7.1.

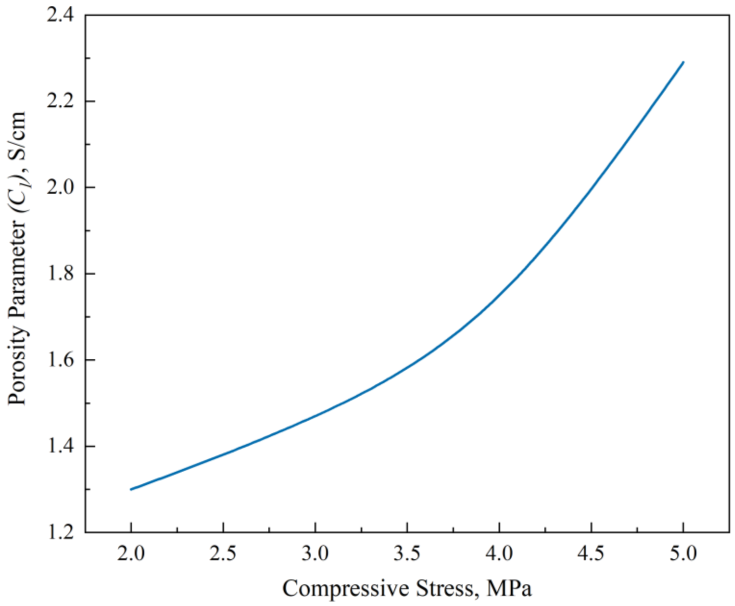

Figure 7.1 Variation of porosity parameter with compressive stress

Equation 7.3, however, has a limitation because it cannot account for the changes due to cyclic loading. This means that Equation 7.3 is not equipped to take residual effects upon unloading (It is noted that the loading and unloading conductivity paths do not overlap due to dissipation-induced residual effect). Thus, additional parameters are incorporated to address this limitation. These additional parameters related to physical changes in the GDL microstructure upon unloading or repeated loading. The parameter $\boldsymbol{s_a}$ is used to account for the accumulation of residual conductivity due to cyclic loading, whereas the parameter s_b accounts for the damage/dissipation parameter and can now be expressed as in Equation 7.4:

$$\left(K_{f(\sigma_c)}\right)_2 = C_1 + C_2\left(1 - e^{-\left(\frac{\phi}{s_b}\right)^{(d\times s_a)}}\right) \tag{7.4}$$

The $\boldsymbol{s_a}$ and $\boldsymbol{s_b}$ parameters are taken into account only during unloading conditions. Therefore, it can be written as, during primary loading, $\boldsymbol{s_a}$ and $\boldsymbol{s_b}$ are inactive, which can be assigned to a constant value that is presumed to be 1. Therefore, it can be rewritten as

For Loading Condition:

$$\left(K_{f(\sigma_c)}\right)_l = C_1 + C_2\left(1\text{-}e^{-\left(\frac{\phi}{s_2}\right)^{(d\times s_1)}}\right) \tag{7.5}$$

Here $s_1 = s_2 = 1$.

The subscript ***l*** in Equation 7.5 defines the material response during loading conditions under which the parameters $\boldsymbol{s_1}$ and $\boldsymbol{s_2}$ are inactive.

For Unloading Condition:

$$\left(K_{f(\sigma_c)}\right)_{ul} = C_1 + C_2\left(1\text{-}e^{-\left(\frac{\phi}{s_4}\right)^{(d\times s_3)}}\right) \tag{7.6}$$

where $s_3 \neq 1$, $s_4 \neq 1$

Here the subscript ***ul*** in Equation 7.6 depicts the material response during the unloading condition due to dissipation induced residual effect.

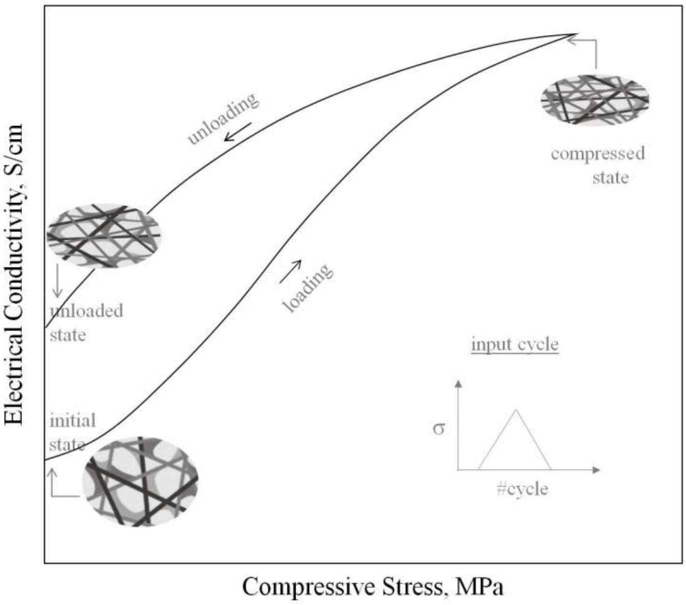
unloading
compressed state
unloaded state
loading
input cycle
σ
#cycle
initial state
Electrical Conductivity, S/cm
Compressive Stress, MPa

Figure 7.2 Schematic representation of expected variation in electrical conductivity of GDL with cyclic compressive stress

Figure 7.2 schematically shows the variation in electrical conductivity of GDL at the initial, intermediate, and relaxed stages. With the increase in compressive stress, the number of fiber contact points increases resulting in elevated electrical conductivity.

At critical loads, the GDL develops fiber cracks/dislocations, and as a consequence, the conductivity slope is expected to reduce with increased load/damage. Here the **'C_2'** parameter takes this into account, whose value is taken as a reduction factor due to fiber cracks and dislocations.

7.3 Results and Discussion

7.3.1 Model Response and Validation

Figure 7.3 shows simulated model results of electrical conductivity-compressive stress response up to a compressive load of 3.5MPa. The proposed model is validated with experimental findings by Radhakrishnan and Haridoss (Radhakrishnan and Haridoss 2010) (the active area in their study was 50 cm^2). As one can observe, the model accurately captures the nonlinear response governed by its prime parameters C_1, C_2, and d.

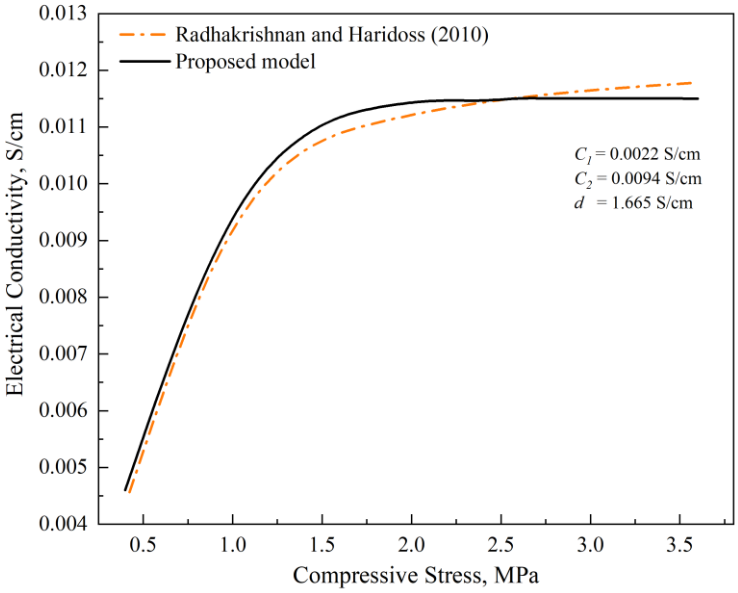

Figure 7.3 Simulated response of electrical conductivity as a function of compressive stress. The response is validated against experimental data. The values of model variables are noted in the figure.

The experimental response shown in Figure 7.3 is not as expected for highly porous structures such as GDL. Such response may have been due to high PTFE loading of about 30wt%, as reported in ref. (Radhakrishnan and Haridoss 2010), leading to a high initial increase in electrical conductivity. Nevertheless, this monotonic loaded variation is easily captured using the proposed model.

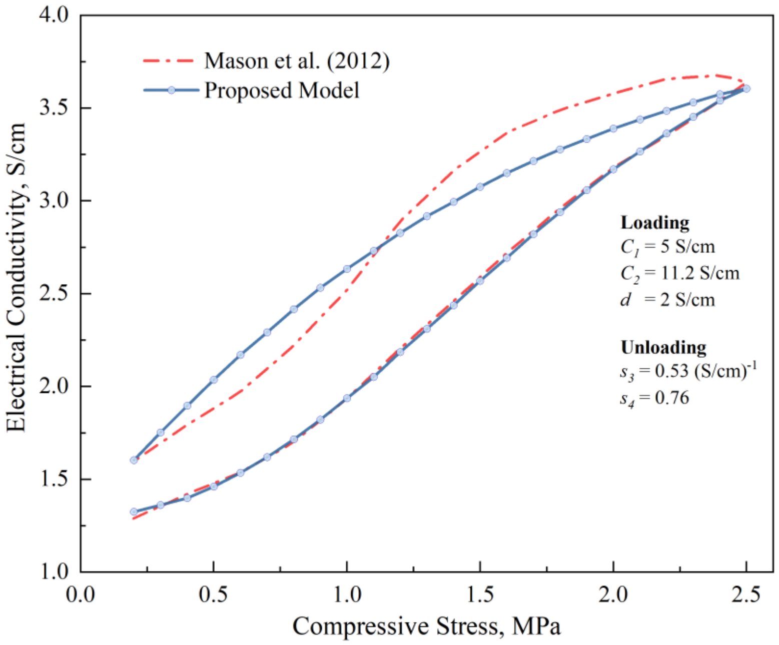

Figure 7.4 Simulated cyclic response with example maximum compressive stress limit of σ = 2.5MPa. The response is validated against experimental data. The values of model variables are noted in the figure.

The cyclic response is shown in Figure 7.4, where a single load-unload cycle is modeled against the literature experimental data reported in Mason et al. (Mason et al. 2012) (in this work, the literature resistivity values are stated in conductivity). The response here differs from Figure 7.2, as PTFE loading, in this case, is much less (5wt%) (Mason et al. 2012). This is the typical response one would expect from highly porous GDL with low PTFE loading. Model-wise, the loading and unloading behaviour unfollow each other and are marked by distinguished nonlinearities. More importantly, the completely unloaded position is marked by residual conductivity, which is an increase of **~21%** from the initial value. It is observed that this response is matched with the experimental observations. The electrical conductivity is generally considerably lower at the initial stages due to insufficient compression leading to lower fiber-to-fiber interaction density. This, however, is modeled to increase dramatically as a function of increasing compressive stress. The irrevocable deformation at the end of the cycle is due to the inelastic deformation of porous composite that leads to a permanent set, causing an increase in the conductivity from the initial state. The magnitude of this residual may attenuate over subsequent cycles, which is reported in the next section.

7.3.2 Electrical cyclic conductivity response

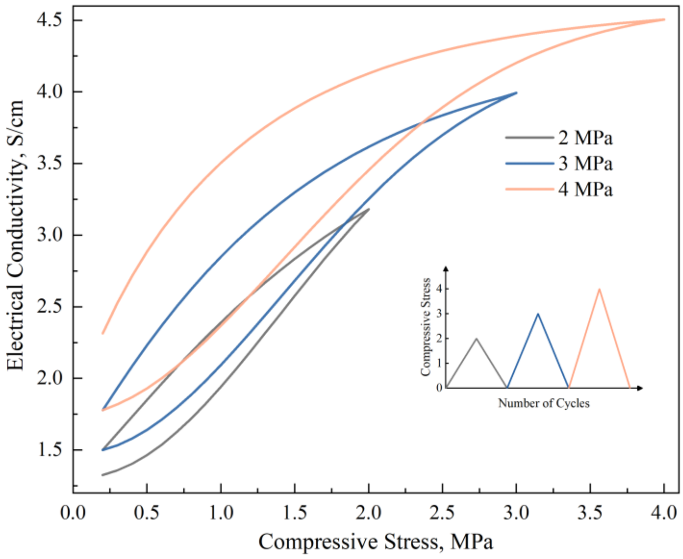

Figure 7.5 Simulated cyclic response with example maximum compressive stress limits of σ = 2 MPa, 3 MPa, and 4 MPa.

Figure 7.5 shows the cyclic behavior of electrical conductivity response at different stress limits of 2 MPa, 3 MPa and 4 MPa. It is observed that the model is able to predict distinguishable uncertainties associated with the nonlinearities both in the loading as well as unloading state. For example, the difference in conductivity between the start-to-end of a loading-unloading cycle for the 2MPa cycle is lower (~ 0.18 S/cm) than the successive cycles for the stress limit of 3MPa (~ 0.28 S/cm) and 4MPa (~ 0.49 S/cm) cases, respectively. Further, it is noted from the figure that the conductivity do not increase monotonically as an increasing function of stress, which is convincingly relatively clear from practical situation where the limits are governed by thresholds relying on the saturation limit of fiber contact density. The plateau at 4MPa case is reflective of this saturation beyond which the there is not further increase in conductivity. There could, however, be a breakdown.

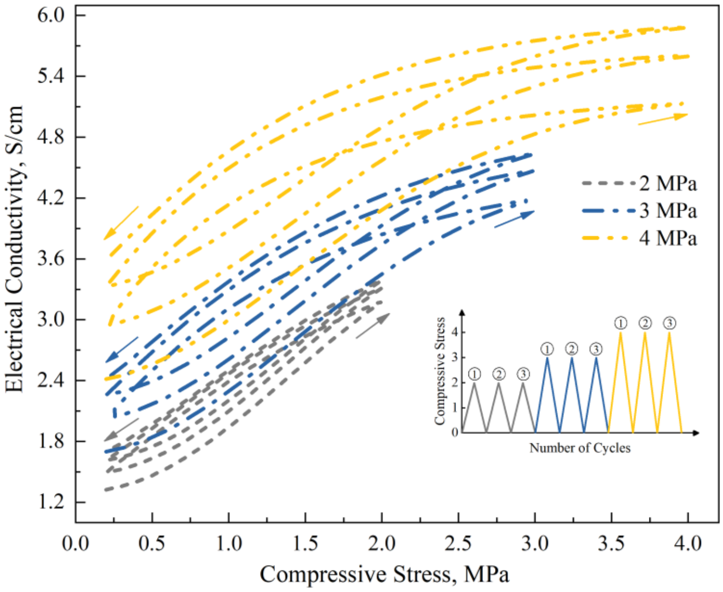

Figure 7.6 Simulated repetitive cyclic response with example maximum compressive stress limits of σ = 2 MPa, 3 MPa, and 4 MPa.

To test the capability of the model for the repetitive cycles under a fixed peak load, a numerical experiment is performed. This has a practical significance as the GDL will be under fixed compressive load, and intrinsic operating conditions may indeed represent these repetitive cycles, albeit not of the same order. Figure 7.5 shows the outcome of this simulation, where one can note that the difference in start-to-end conductivity reduces for subsequent cycles. This can be termed as 'electrical softening'. Thus, the proposed model is versatile in predicting complex uncertainties and nonlinearities. The residual conductivity variation on par with the 'electrical softening' per cycle is further explored in Figure 7.7, where residual conductivity predicted by the model is plotted for different stress levels with a respective number of cycles.

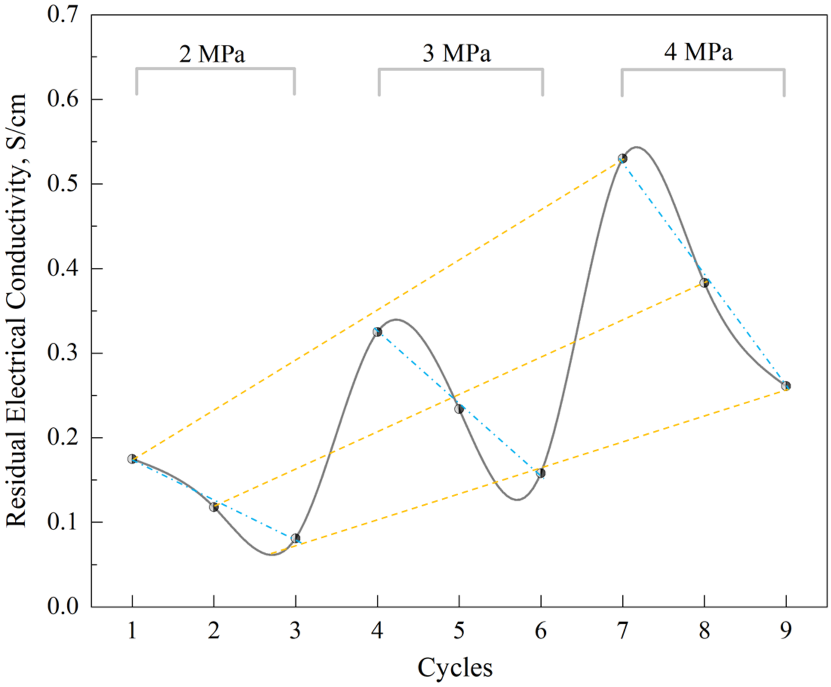

Figure 7.7 Variation of residual electrical conductivity for repetitive stress cycles

It can be observed that a maximum residual conductivity in each stress case is during the first load-unload cycle, which reduces with subsequent cycles due to increased permanent set. The slope of this reduction is more severe at higher stress levels, as indicated by blue dotted lines. This can also be observed from horizontal slope lines plotted for respective cycles per stress limits.

The values of parameters such as $\boldsymbol{C_1}$, $\boldsymbol{C_2}$, $\boldsymbol{d}$, $\boldsymbol{s_3}$, and $\boldsymbol{s_4}$ vary cyclically between different stress limits and the number of cycles. Hence, obtaining the evolution equations for each of these parameters is necessary. The material parameter's evolution equations are provided in the supplementary information.

7.3.3 Parametric Evaluation

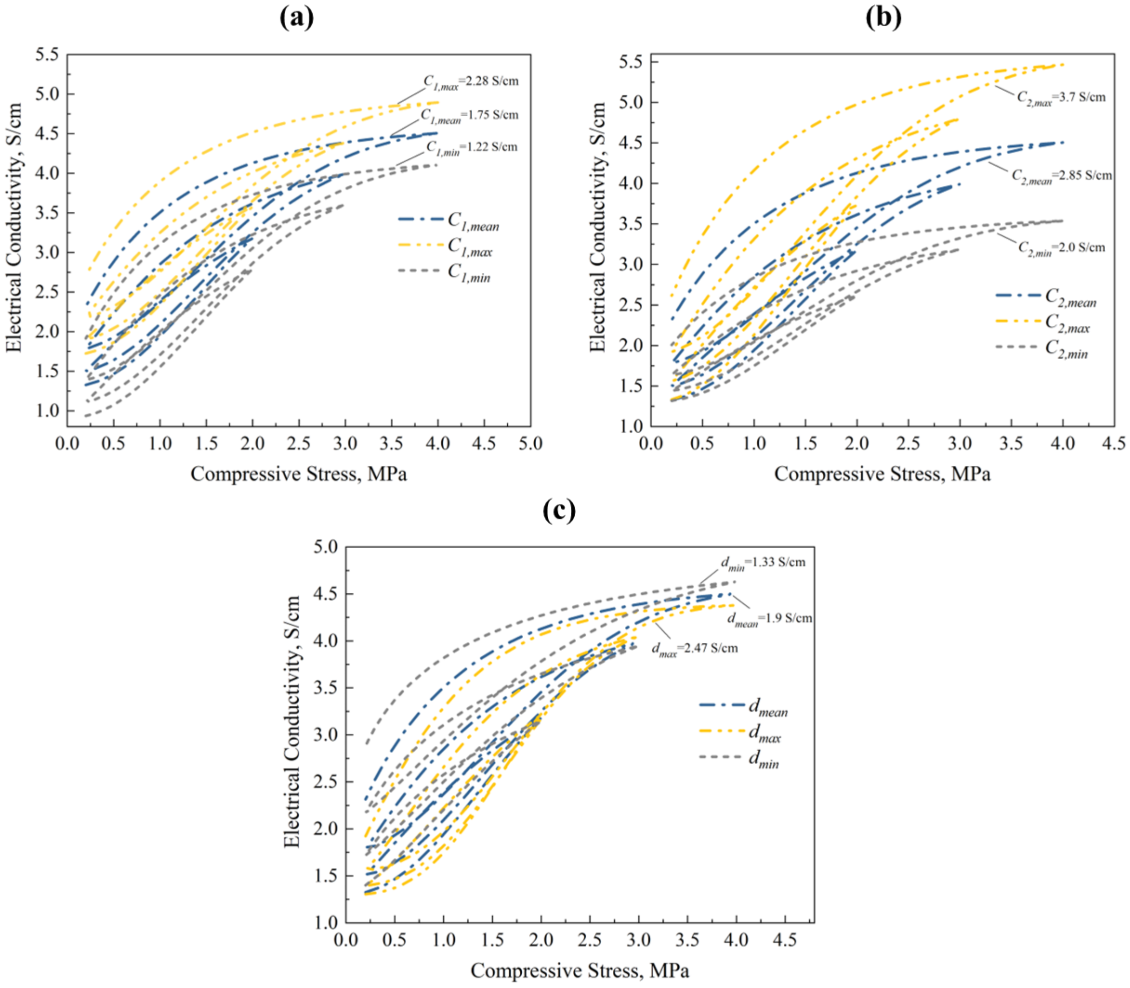

Figure 7.8 Parametric evaluation for parameters: (a) porosity parameter 'C1'; (b) fiber contact density parameter 'C2'; and (c) saturation limit parameter 'd'

In order to test the versatility of the model in view of its constitutive parameters that define phenomenological narrative of the proposed model, a parametric analysis of vital variables is performed. As dictated by the relation in Equation 7.4, the electrical conductivity response is influenced by several variables relating to GDL's constituents. Figure 7.8(a) shows model results for $\boldsymbol{C_1}$ variable. Though this variable is a function of porosity, it has a inverse relation. Nevertheless, its physical importance is quite evident, where one can observe a comprehensive shift in the conductivity curve as a function of $\boldsymbol{C_1}$. For higher value of $\boldsymbol{C_1}$ (a case where structural porosity is low), the initial intercept of the conductivity also shifts to higher value along with the entire conductivity response. In order to understand the influence of fiber density factor on the overall response, parametric evaluation of $\boldsymbol{C_2}$ is performed, and the results are shown in Figure 7.8(b). Evidently, $\boldsymbol{C_2}$ seems to affect the latter portion of the response curve where the compressive stress is high. This is reasonable as higher stresses lead to increased fiber contact density, which is reflected in the model results. A notable difference between the C1 and C2 is that the latter will not affect the initial portion of the conductivity response that is essentially a function of porous matrix response governed by $\boldsymbol{C_1}$. Mathematically, the exponential increase of conductivity as a function of compressive stress is limited by parameter $\boldsymbol{d}$ (which can be called as a damping factor). Therefore, $\boldsymbol{d}$ is linked to saturation limit of contact density of fibers. The parametric evaluation of $\boldsymbol{d}$ is shown in Figure 7.8(c). If the saturation parameter is set to minimum, electrical conductivity increases relatively as damping factor or resistance to contact density is lower.

Although above results give an overall sense of the proposed model's capability, it is desirable to understand the model's versatility for physical events such as break stress. Figure 7.9 shows cyclic response with and without break stress factor in the model. The input cycle is shown in the inset figure, and the first set of stress cycle is same as the previous cases, where break stress function is disabled to mark the visual difference with the other case. The consequent second set of stress cycle is enabled with break stress factor where the limiting stress is fixed to 2MPa (also termed as critical or transition stress limit (Qiu et al. 2018)). This can be understood from Figure 7.9. Figure 7.9(a) shows model response under normal conditions, where compressive load is within the limiting stress. However, as soon as the compressive load increases up to threshold limit, the following cycle must show a reduced conductivity. This is reported in Figure 7.9(b), whereas the first input cycle reaches 2MPa limit, the response of the following cycle is not as same as the one observed from Figure 7.9(a). That is to say, as the critical stress level is breached, the electrical conducting capacity of GDL relatively reduces over number of repetitive cycles. The difference between both the models is shown in Figure 7.9(c), where the slope of model response curve, beyond the threshold line, with the break stress enabled case is much lower than the one without this limitation. This effectively, in comparison, reduces the electrical conductivity during the unloaded stage. Next, the work considers taking a simulation case where the models are simulated under different levels of compressive loads. Clearly, as observed from Figure 7.9(d), the model without the break stress factor cannot take into effect of slope reduction in subsequent cycles even though the compressive stress reaches the threshold limit. Overall, the relative percentage reduction in case of break-stress model is taken to be around 15% which is consistent with the literature experimental data (Qiu et al. 2018).

7.3.4 Break stress behaviour

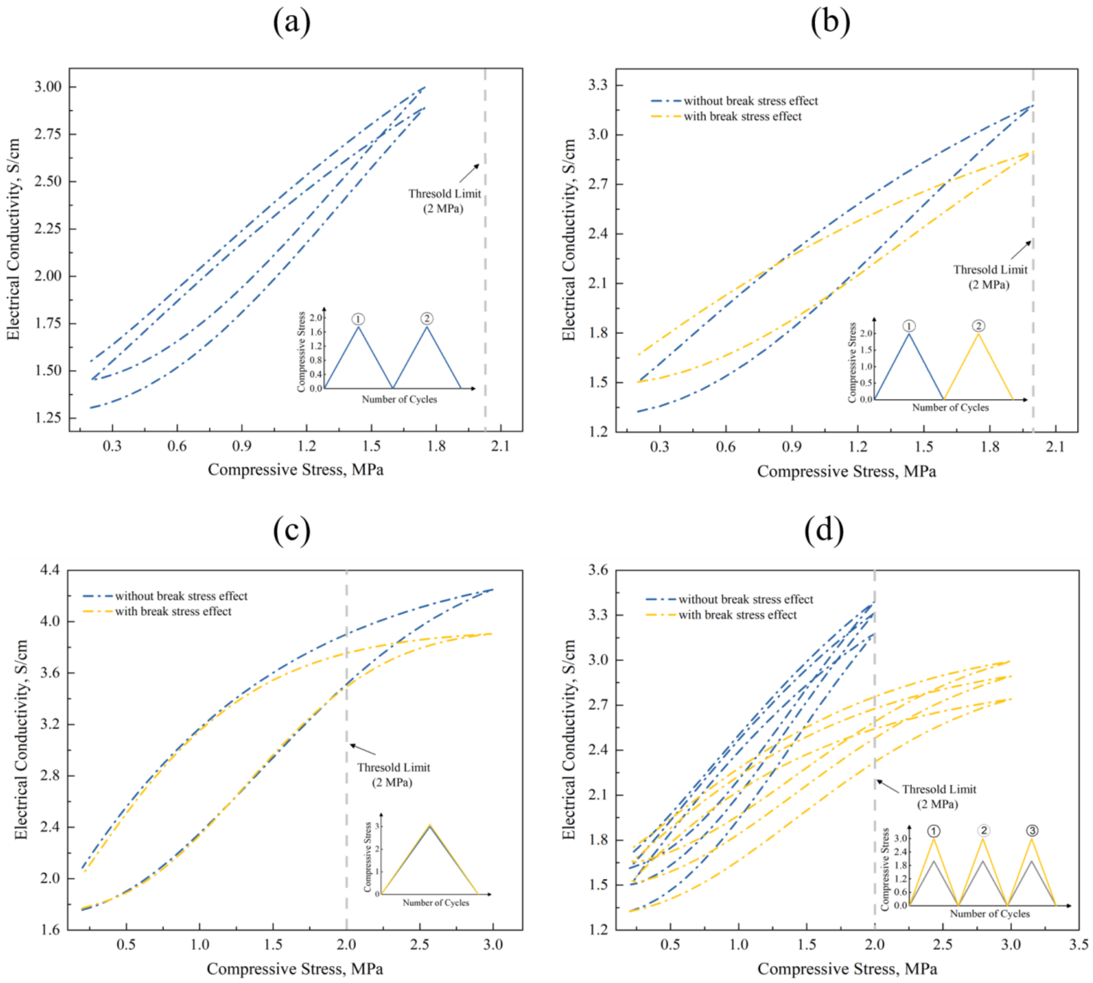

Figure 7.9 Model response curves (a): for applied compressive load is less than the threshold limit; (b): for applied compressive load is same as threshold limit and its influence on subsequent cycle of same stress limit with break stress factor enabled; (c)

with break stress and without break stress factor for stress load beyond threshold limit; (d) with break stress and without break stress factor for repetitive stress cycles.

In terms of model equations, the break stress factor is introduced in Equation 7.4, in which the fiber contact density dictated by *'C_2'* is made to reduce beyond critical stress limit. Below are the details on the models and evolution equations considered for the study.

The evolution equations for various parameters such as C_1, C_2, d, s_3 and s_4 are as expressed below. The parameters *a,b,c* and *d* with different subscripts are the fitting parameters. Symbols σ and n represents applied compressive stress and cycle number, respectively.

$$C_1 = \frac{a_1}{1+(b_1\cdot\sigma)+(c_1\cdot n)} \tag{7.7}$$

where a_1 = 0.8886 S/cm, b_1 = -0.1448 (MPa)$^{-1}$, c_1 = -0.05282

$$C_2 = e^{\left[a_2+(b_2\cdot\sigma)+(c_2\cdot n)\right]} \tag{7.8}$$

where a_2 = 1.0421 S/cm, b_2 = 0.00667 (S/cm.MPa) c_2 = -0.02354 S/cm

$$d = a_3\left(1-\left(\frac{\sigma}{b_3}\right)\right) \qquad 7.9$$

where a_3 = 2.3 S/cm and b_3 = 23 MPa.

$$s_3 = a_4+(b_4\cdot\sigma)+(c_4\cdot n) \tag{7.10}$$

where a_4 = 0.58 (S/cm)$^{-1}$, b_4 = -0.04 (S·MPa/cm)$^{-1}$, c_4 = 0.06 (S/cm)$^{-1}$.

$$s_4 = \frac{a_5+(b_5\cdot\sigma)+(c_5\cdot n)}{(d_5\cdot\sigma)+n} \tag{7.11}$$

where a_5 = 2.3311, b_5 = -0.2017 (MPa)$^{-1}$, c_5 = 0.990, d_5 = 1.01 (MPa)$^{-1}$

The parameters C_1, C_2 changes under break stress condition and are expressed as below:

$$C_1 = \frac{a_6}{1+\left(b_6 \cdot \sigma\right)+\left(c_6 \cdot n\right)} \tag{7.12}$$

where a_6 = 0.93693 S/cm, b_6 = -0.13063 $(\mathrm{MPa})^{-1}$, c_6 = -0.04671

$$C_2 = e^{\left[a_7+\left(b_7 \cdot \sigma\right)+\left(c_7 \cdot n\right)\right]} \tag{7.13}$$

where a_7 = 2.33294 S/cm, b_7 = -0.6374 (S/cm·MPa), c_7 = -0.0246 S/cm.

7.4 Summary

In order to predict the cyclic electrical conductivity of GDL, a constituent-dependent phenomenological model is proposed and developed. The model validation is presented by matching the experimental data, from which basic model parameters are further explored to predict cyclic response. The cyclic electrical conductivity response is simulated to be the outcome of cumulative changes in constitutive phases such as porous matrix and fiber network of GDL. The model is capable of predicting residual conductivity upon unloading cycles. The difference in conductivity between loading and unloading cycles is significantly large at the initial stages and continues to reduce with repeated cycles within the same stress limit (termed here as 'electrical softening'). Besides, parametric evaluation is performed, and the findings outlined that the porosity parameter impacts the initial stages of compression. The fiber contact density parameter impacts the final stage of loading and the initial stage of unloading. A concept of break stress where the compressive load reaches the threshold limit is included to showcase the versatility of the model. Overall, the model discussed in the present work provides the main framework for obtaining cyclic electrical conductivity and can be used to examine the localised variations in GDL. Table 7.1 briefs about the present study with the work of similar interest from literature.

Table 7.1 Comparison of the current study with literature

Source	**Outcome/Claims**
Current Study	A constitutive phenomenological model to predict cyclic electrical conductivity in GDLs is presented
	Residual conductivity, conductivity softening, and break stress are predicted.
	Electrical softening is defined in terms of start-to-end conductivity reduction along with thresold limit is proposed as break stress
Gigos et al. (2015)	Revealed that under high number of cyclic loads, the behavior of GDL approaches a steady state after 5-6 cycles.
Radhakrishnan and Haridoss (2010)	The impact of cyclic compression on GDL results in irreversible changes in pore size and electrical resistance. Nevertheless, the article fails to explain the reversible behaviour of GDL in terms of electrical resistance.
Todd et al. (2016)	The through-plane resistivity decreases with cyclic compression while in-plane resistivity increases.

7.5 Closure

This chapter detailed the phenomenological constitutive model in predicting bulk electrical conductivity of GDL under different stress limits. The model reported here provides the main framework for examining the localised variations in GDL. The next chapter presents the conclusion of present research work combined with the scope for future work.

CHAPTER 8

CONCLUSIONS AND FUTURE WORK

8.1 Conclusions

The performance of the gas diffusion layer (GDL) significantly impacts the durability of a polymer electrolyte fuel cell (PEFC). The GDL in an assembled fuel cell is always under compression by the clamping force. Since the GDL is highly porous, its various mechanical and electrical properties strongly depend on its compressibility.

This thesis begins with a numerical investigation of clamping endplate configurations. The results demonstrated that selecting GDL material models is critical in assessing bulk and interface features. Furthermore, the influence of clamping endplate design can be readily misconstrued if nonlinear material models are not adopted. The isotropic elastic model is ineffective, whereas the nonlinear incompressible case provides a qualitative understanding of interface resistance, stress, and pressure distribution. **It is observed that the compressible GDL material model appears to offer a reasonable solution for differentiating clamping design on the interface and bulk properties.**

Consequently, the combined effect of inlet relative humidity (RH) and interfacial contact resistance (ICR) on the performance of single-channel PEFC with GDL flow/electrical heterogeneities is reported. The study investigated the homogeneous and heterogeneous GDL properties using a multiphase steady-state computational model. The performance of the cell, the distribution of reactants, the local current density, the water mass percentage, the temperature, and the cathodic overpotential are analysed for each study instance. **It is reported that the presence of electrical/flow heterogeneity in combination with full humidification at the anode and partial humidification at the cathode provided the highest performance.**

Further, a single-cell, multichannel, three-dimensional PEFC numerical model with a 25cm^2 active area is used to analyse transport characteristics and cell performance for the two clamping mechanisms outlined previously. The properties of GDL, including

ICR, porosity, and permeability, are retrieved from the earlier study and were further developed in this study. **Due to the efficient reaction of the reactants, results revealed that the proposed clamping configuration offers better cell performance with higher current and power density at low voltage compared to the conventional endplate configuration.**

Furthermore, the effect of hot-press conditions comprising of elevated pressure and temperature is studied on the cyclic behaviour of GDL with and without MPL. Investigation of cyclic mechanical response under pre- and post hotpress conditions for GDL materials is carried out. The study reported that the mechanical response of GDL with MPL varies significantly, with stress to strain ratio increasing by almost 120% in post-hotpress conditions. **It is proven that the GDL with MPL under post-hotpress conditions increases the compressive strength by about 600% while elastic resilience reduces by a similar amount.**

Finally, a constituent-dependent phenomenological model is proposed and developed to predict the cyclic electrical conductivity of GDL. The cyclic conductivity response is simulated to be the outcome of cumulative changes in constitutive phases such as the porous matrix and fiber network of GDL. The difference in conductivity between loading and unloading cycles is significantly large at the initial stages and continues to reduce with repeated cycles within the same stress limit. **Overall, the model considered in the present work sets out the general framework to obtain cyclic electrical conductivity and can be utilized to investigate the localized variations in GDL.**

8.2 Scope for future work

In order to further expand this work, future research in this area shall include:

- Structural analysis of the proposed endplate configuration with the full stack PEFC and check for its effectiveness.
- Investigation of transport characteristics and cell performance evaluation of the proposed endplate configuration with the full stack PEFC.
- Carrying experimental setup in evaluating cyclic electrical conductivity of GDL.

REFERENCES

Akiki, T., Accary, G., Charon, W., and Kouta, R. (2012). “Influence of local porosity, local permeability, and contact resistance between the gas diffusion layer and the bipolar plate, on the performances of a polymer electrolyte membrane fuel cell.” *2nd Int. Conf. Commun. Comput. Control Appl. CCCA 2012*, 1–6.

Alizadeh, E., Barzegari, M. M., Momenifar, M., Ghadimi, M., and Saadat, S. H. M. (2016). “Investigation of contact pressure distribution over the active area of PEM fuel cell stack.” *Int. J. Hydrogen Energy*, 41(4), 3062–3071.

Alizadeh, E., Ghadimi, M., Barzegari, M. M., Momenifar, M., and Saadat, S. H. M. (2017). “Development of contact pressure distribution of PEM fuel cell’s MEA using novel clamping mechanism.” *Energy*, 131, 92–97.

Asghari, S., Shahsamandi, M. H., and Ashraf Khorasani, M. R. (2010). “Design and manufacturing of end plates of a 5 kW PEM fuel cell.” *Int. J. Hydrogen Energy*, 35(17), 9291–9297.

Atifi, A., Bikri, K. El, and Ettouhami, M. (2019). “Numerical simulation of Effect of Contact Pressure on Gas Diffusion Layers deformation of a PEM Fuel Cell.” *MATEC Web Conf.*, 286, 09006.

Atyabi, S. A., Afshari, E., Wongwises, S., Yan, W. M., Hadjadj, A., and Shadloo, M. S. (2019). “Effects of assembly pressure on PEM fuel cell performance by taking into accounts electrical and thermal contact resistances.” *Energy*, 179, 490–501.

B. Liu, L.F. Liu, M.Y. Wei, C. W. W. (2016). “Vibration mode analysis of the proton exchange membrane fuel cell stack.” *J. Power Sources*, 331, 299–307.

Barton, R. H. (2013). “Fuel cell stack and compression system therefor.”

Barton, R. H., and Voss, H. H. (1997). “Electrochemical fuel cell assembly with complaint compression mechanism.”

Barzegari, M. M., Ghadimi, M., and Momenifar, M. (2020). “Investigation of contact pressure distribution on gas diffusion layer of fuel cell with pneumatic endplate.” *Appl.*

Energy, 263, 114663.

Bates, A., Mukherjee, S., Hwang, S., Lee, S. C., Kwon, O., Choi, G. H., and Park, S. (2013). “Simulation and experimental analysis of the clamping pressure distribution in a PEM fuel cell stack.” *Int. J. Hydrogen Energy*, 38(15), 6481–6493.

Bayrakçeken, A., Erkan, S., Türker, L., and Eroğlu, I. (2008). “Effects of membrane electrode assembly components on proton exchange membrane fuel cell performance.” *Int. J. Hydrogen Energy*, 33(1), 165–170.

Bhosale, A. C., and Rengaswamy, R. (2019). “Interfacial contact resistance in polymer electrolyte membrane fuel cells: Recent developments and challenges.” *Renew. Sustain. Energy Rev.*, Elsevier Ltd.

Bosomoiu, M., Tsotridis, G., and Bednarek, T. (2015). “Study of effective transport properties of fresh and aged gas diffusion layers.” *J. Power Sources*, 285, 568–579.

Bouziane, K., Khetabi, E. M., Lachat, R., Zamel, N., Meyer, Y., and Candusso, D. (2020). “Impact of cyclic mechanical compression on the electrical contact resistance between the gas diffusion layer and the bipolar plate of a polymer electrolyte membrane fuel cell.” *Renew. Energy*, 153, 349–361.

Carral, C., and Mele, P. (2022). “Modeling the original and cyclic compression behavior of non-woven gas diffusion layers for fuel cells.” *Int. J. Hydrogen Energy*, 47(55), 23348–23359.

Carral, C., and Mélé, P. (2014). “A numerical analysis of PEMFC stack assembly through a 3D finite element model.” *Int. J. Hydrogen Energy*, 39(9), 4516–4530.

Chang, W. R., Hwang, J. J., Weng, F. B., and Chan, S. H. (2007). “Effect of clamping pressure on the performance of a PEM fuel cell.” *J. Power Sources*, 166(1), 149–154.

Chen, G., Xu, Q., Xuan, J., Liu, J., Fu, Q., Shi, W., Su, H., and Xing, L. (2021). “Numerical study of inhomogeneous deformation of gas diffusion layers on proton exchange membrane fuel cells performance.” *J. Energy Storage*, 44, 103486.

Chen, Y. C., Karageorgiou, C., Eller, J., Schmidt, T. J., and Büchi, F. N. (2022). “Determination of the porosity and its heterogeneity of fuel cell microporous layers by

X-ray tomographic microscopy." *J. Power Sources*, 539, 231612.

Chien, C., Hu, Y., Su, T., Liu, H., Wang, C., Yang, P., and Lu, Y. (2016). "Effects of bolt pre-loading variations on performance of GDL in a bolted PEMFC by 3-D FEM analysis." *Energy*, 113, 1174–1187.

Chung, T. T., Lin, C. Te, and Shiu, H. R. (2016). "Mechanical design and analysis of a proton exchange membrane fuel cell stack." *J. Chinese Inst. Eng. Trans. Chinese Inst. Eng. A*, 39(3), 353–362.

Cindrella, L., Kannan, A. M., Lin, J. F., Saminathan, K., Ho, Y., Lin, C. W., and Wertz, J. (2009). "Gas diffusion layer for proton exchange membrane fuel cells—A review." *J. Power Sources*, 194(1), 146–160.

Cooper, N. J., Santamaria, A. D., Becton, M. K., and Park, J. W. (2017). "Neutron radiography measurements of in-situ PEMFC liquid water saturation in 2D & 3D morphology gas diffusion layers." *Int. J. Hydrogen Energy*, 42(25), 16269–16278.

Dey, T., Deshpande, J., Singdeo, D., and Ghosh, P. C. (2019). "Study of PEM Fuel Cell End Plate Design by Structural Analysis Based on Contact Pressure." *J. Energy*, 2019, 1–11.

El-Kharouf, A., Mason, T. J., Brett, D. J. L., and Pollet, B. G. (2012). "Ex-situ characterisation of gas diffusion layers for proton exchange membrane fuel cells." *J. Power Sources*, 218, 393–404.

Emmanuel, B. O., Barendse, P., and Chamier, J. (2018). *Effect of Anode and Cathode Reletive Humidity Variance and Pressure Gradient on Single Cell PEMFC Performance; Effect of Anode and Cathode Reletive Humidity Variance and Pressure Gradient on Single Cell PEMFC Performance*.

Escribano, S., Blachot, J. F., Ethève, J., Morin, A., and Mosdale, R. (2006). "Characterization of PEMFCs gas diffusion layers properties." *J. Power Sources*, 156(1 SPEC. ISS.), 8–13.

Espinoza, M., Andersson, M., Yuan, J., and Sundén, B. (2015). "Compress effects on porosity , gas-phase tortuosity , and gas permeability in a simulated PEM gas diffusion layer." *Int. J. Energy Res.*, 39(June), 1528–1536.

Fazeli, M., Hinebaugh, J., Fishman, Z., Tötzke, C., Lehnert, W., Manke, I., and Bazylak, A. (2016). "Pore network modeling to explore the effects of compression on multiphase transport in polymer electrolyte membrane fuel cell gas diffusion layers." *J. Power Sources*, 335, 162–171.

Feser, J. P., Prasad, A. K., and Advani, S. G. (2006). "Experimental characterization of in-plane permeability of gas diffusion layers." *J. Power Sources*, 162(2), 1226–1231.

Fly, A., Chen, R., and Wang, X. (2018). "Equivalent stiffness model of a proton exchange membrane fuel cell stack including hygrothermal effects and dimensional tolerances." *J. Electrochem. Energy Convers. Storage*, 15(3), 1–11.

Fly, A., Meyer, Q., Whiteley, M., Iacoviello, F., Neville, T., Shearing, P. R., Brett, D. J. L., Kim, C., and Chen, R. (2019). "X-ray tomography and modelling study on the mechanical behaviour and performance of metal foam flow-fields for polymer electrolyte fuel cells." *Int. J. Hydrogen Energy*, 44(14), 7583–7595.

Fu, Y., Hou, M., Yan, X., Hou, J., Luo, X., Shao, Z., and Yi, B. (2007). "Research progress of aluminium alloy endplates for PEMFCs." *J. Power Sources*, 166(2), 435–440.

Gaiselmann, G., Tötzke, C., Manke, I., Lehnert, W., and Schmidt, V. (2014). "3D microstructure modeling of compressed fiber-based materials." *J. Power Sources*, 257, 52–64.

Gandiglio, M., Lanzini, A., Santarelli, M., and Leone, P. (2014). "Design and optimization of a proton exchange membrane fuel cell CHP system for residential use." *Energy Build.*, 69, 381–393.

García-Salaberri, P. A., Vera, M., and Zaera, R. (2011). "Nonlinear orthotropic model of the inhomogeneous assembly compression of PEM fuel cell gas diffusion layers." *Int. J. Hydrogen Energy*, 36(18), 11856–11870.

García-Salaberri, P. A., Zenyuk, I. V., Hwang, G., Vera, M., Weber, A. Z., and Gostick, J. T. (2019). "Implications of inherent inhomogeneities in thin carbon fiber-based gas diffusion layers: A comparative modeling study." *Electrochim. Acta*, 295, 861–874.

Ge, J., Higier, A., and Liu, H. (2006). "Effect of gas diffusion layer compression on PEM fuel cell performance." *J. Power Sources*, 159(2), 922–927.

Gigos, P. A., Faydi, Y., and Meyer, Y. (2015). "Mechanical characterization and analytical modeling of gas diffusion layers under cyclic compression." *Int. J. Hydrogen Energy*, 40(17), 5958–5965.

Göbel, M., Godehardt, M., and Schladitz, K. (2017). "Multi-scale structural analysis of gas diffusion layers." *J. Power Sources*, 355, 8–17.

Gostick, J. T., Fowler, M. W., Pritzker, M. D., Ioannidis, M. A., and Behra, L. M. (2006). "In-plane and through-plane gas permeability of carbon fiber electrode backing layers." *J. Power Sources*, 162(1), 228–238.

Hamour, M., Grandidier, J. C., Ouibrahim, A., and Martemianov, S. (2015). "Electrical conductivity of PEMFC under loading." *J. Power Sources*, 289, 160–167.

Hebling, C., Heitzler, A., and Schmitz, A. (2005). "Fuel cell arrangement with tightening elements."

Hendricks, F., Chamier, J., and Tanaka, S. (2020). "Membrane electrode assembly performance of a standalone microporous layer on a metallic gas diffusion layer." *J. Power Sources*, 464, 228222.

Hottinen, T., Himanen, O., Karvonen, S., and Nitta, I. (2007). "Inhomogeneous compression of PEMFC gas diffusion layer. Part II. Modeling the effect." *J. Power Sources*, 171(1), 113–121.

Hu, G., Wu, X., Suo, Y., Xia, Y., Xu, Y., and Zhang, Z. (2018). "Finite element analysis of PEMFC assembling based on ANSYS." *Int. J. Electrochem. Sci.*, 13(2), 2080–2089.

Hung, C. H., Chiu, C. H., Wang, S. P., Chiang, I. L., and Yang, H. (2012). "Ultra thin gas diffusion layer development for PEMFC." *Int. J. Hydrogen Energy*, 37(17), 12805–12812.

Irmscher, P., Qui, D., Janßen, H., Lehnert, W., and Stolten, D. (2019). "Impact of gas diffusion layer mechanics on PEM fuel cell performance." *Int. J. Hydrogen Energy*, 44(41), 23406–23415.

Ismail, M. S., Hassanpour, A., Ingham, D. B., Ma, L., and Pourkashanian, M. (2012). “On the compressibility of gas diffusion layers in proton exchange membrane fuel cells.” *Fuel Cells*, 12(3), 391–397.

Jha, V., Hariharan, R., and Krishnamurthy, B. (2020). “A 3 dimensional numerical model to study the effect of GDL porosity on high temperature PEM fuel cells.” *Int. J. Heat Mass Transf.*, 161, 120311.

Jin, L., Chortos, A., Lian, F., Pop, E., Linder, C., Bao, Z., and Cai, W. (2018). “Microstructural origin of resistance-strain hysteresis in carbon nanotube thin film conductors.” *Proc. Natl. Acad. Sci. U. S. A.*, 115(9), 1986–1991.

Kahveci, E. E., and Taymaz, I. (2015). “Effect of Humidification of the Reactant Gases in the Proton Exchange Membrane Fuel Cell.” *J. Clean Energy Technol.*, 3(5), 356–359.

Kandlikar, S. G., Lu, Z., Lin, T. Y., Cooke, D., and Daino, M. (2009). “Uneven gas diffusion layer intrusion in gas channel arrays of proton exchange membrane fuel cell and its effects on flow distribution.” *J. Power Sources*, 194(1), 328–337.

Karvonen, S., Hottinen, T., Ihonen, J., and Uusalo, H. (2008). “Modeling of polymer electrolyte membrane fuel stack end plates.” *J. Fuel Cell Sci. Technol.*, 5(4), 1–9.

Khetabi, E. M., Bouziane, K., Zamel, N., François, X., Meyer, Y., and Candusso, D. (2019). “Effects of mechanical compression on the performance of polymer electrolyte fuel cells and analysis through in-situ characterisation techniques - A review.” *J. Power Sources*, Elsevier B.V.

Koorata, P. K., and Bhat, S. D. (2020). “Compressive cyclic response of PEM fuel cell gas diffusion media.” *Int. J. Hydrogen Energy*, 46(7), 5570–5579.

Koorata, P. K., and Bhat, S. D. (2021). “Thermomechanical stability and inelastic energy dissipation as durability criteria for fuel cell gas diffusion media with pre-assembly effects.” *Int. J. Hydrogen Energy*.

Kusoglu, A., Karlsson, A. M., Santare, M. H., Cleghorn, S., and Johnson, W. B. (2006).

“Mechanical response of fuel cell membranes subjected to a hygro-thermal cycle.” *J. Power Sources*, 161(2), 987–996.

Lee, T., and Yang, C. (2020). “A parametric study on the deformation of gas diffusion layer in PEM fuel cell.” *J. Mech. Sci. Technol.*, 34(1), 259–268.

Li, S., and Sundén, B. (2018). “Effects of gas diffusion layer deformation on the transport phenomena and performance of PEM fuel cells with interdigitated flow fields.” *Int. J. Hydrogen Energy*, 43(33), 16279–16292.

Li, S., Yuan, J., and Andersson, M. (2017a). “Influence of anisotropic gas diffusion layers on transport phenomena in a proton exchange membrane fuel cell.” *Int. J. Energy Res.*

Li, S., Yuan, J., Xie, G., and Sunden, B. (2017b). “Numerical investigation of transport phenomena in high temperature proton exchange membrane fuel cells with different flow field designs.” *Numer. Heat Transf. Part A Appl.*, 72(11), 807–820.

Li, W. Z., Yang, W. W., Zhang, W. Y., Qu, Z. G., and He, Y. L. (2019). “Three-dimensional modeling of a PEMFC with serpentine flow field incorporating the impacts of electrode inhomogeneous compression deformation.” *Int. J. Hydrogen Energy*, 44(39), 22194–22209.

Liang, P., Qiu, D., Peng, L., Yi, P., Lai, X., and Ni, J. (2018). “Contact resistance prediction of proton exchange membrane fuel cell considering fabrication characteristics of metallic bipolar plates.” *Energy Convers. Manag.*, 169(April), 334–344.

Lin, P., Zhou, P., and Wu, C. W. (2011). “Multi-objective topology optimization of end plates of proton exchange membrane fuel cell stacks.” *J. Power Sources*, 196(3), 1222–1228.

Lu, Z., Kim, C., Karlsson, A. M., Cross, J. C., and Santare, M. H. (2011). “Effect of gas diffusion layer modulus and land–groove geometry on membrane stresses in proton exchange membrane fuel cells.” *J. Power Sources*, 196(10), 4646–4654.

Mahmoudi, A. H., Ramiar, A., and Esmaili, Q. (2016). “Effect of inhomogeneous compression of gas diffusion layer on the performance of PEMFC with interdigitated flow field." *Energy Convers. Manag.*, 110, 78–89.

Majlan, E. H., Rohendi, D., Daud, W. R. W., Husaini, T., and Haque, M. A. (2018). "Electrode for proton exchange membrane fuel cells: A review." *Renew. Sustain. Energy Rev.*, 89(March), 117–134.

Mason, T. J., Millichamp, J., Neville, T. P., El-Kharouf, A., Pollet, B. G., and Brett, D. J. L. (2012). "Effect of clamping pressure on ohmic resistance and compression of gas diffusion layers for polymer electrolyte fuel cells." *J. Power Sources*, 219, 52–59.

Mathur, V. K., and Crawford, J. (2007). "Fundamentals of gas diffusion layers in PEM fuel cells." *Recent Trends Fuel Cell Sci. Technol.*, 400, 116–128.

Mauger, S. A., Wang, M., Cetinbas, F. C., Dzara, M. J., Park, J., Myers, D. J., Ahluwalia, R. K., Pylypenko, S., Hu, L., Litster, S., Neyerlin, K. C., and Ulsh, M. (2021). "Development of high-performance roll-to-roll-coated gas-diffusion-electrode-based fuel cells." *J. Power Sources*, 506, 230039.

Mikkola, M., Tingelöf, T., and Ihonen, J. K. (2009). "Modelling compression pressure distribution in fuel cell stacks." *J. Power Sources*, 193(1), 269–275.

Millichamp, J., Mason, T. J., Neville, T. P., Rajalakshmi, N., Jervis, R., Shearing, P. R., and Brett, D. J. L. (2015). "Mechanisms and effects of mechanical compression and dimensional change in polymer electrolyte fuel cells – A review." *J. Power Sources*, 284, 305–320.

Mishra, V., Yang, F., and Pitchumani, R. (2004). "Measurement and prediction of electrical contact resistance between gas diffusion layers and bipolar plate for applications to PEM fuel cells." *J. Fuel Cell Sci. Technol.*, 1(1), 2–9.

Montanini, R., Squadrito, G., and Giacoppo, G. (2009). "Experimental evaluation of the clamping pressure distribution in a pem fuel cell using matrix-based piezoresistive thin-film sensors." *19th IMEKO World Congr. 2009*, 2, 920–925.

Morgan, J. M., and Datta, R. (2014). "Understanding the gas diffusion layer in proton exchange membrane fuel cells. I. How its structural characteristics affect diffusion and performance.” *J. Power Sources*, 251, 269–278.

Movahedi, M., Ramiar, A., and Ranjber, A. A. (2018). “3D numerical investigation of clamping pressure effect on the performance of proton exchange membrane fuel cell with interdigitated flow field.” *Energy*, 142, 617–632.

Mukherjee, M., Bonnet, C., and Lapicque, F. (2020). “Estimation of through-plane and in-plane gas permeability across gas diffusion layers (GDLs): Comparison with equivalent permeability in bipolar plates and relation to fuel cell performance.” *Int. J. Hydrogen Energy*, 45(24), 13428–13440.

Murphy, O. J., Salinas, C., and Cisar, A. J. (2000). “Apparatus and method for compressing a stack of electrochemical cells.”

Nitta, I., Hottinen, T., Himanen, O., and Mikkola, M. (2007). “Inhomogeneous compression of PEMFC gas diffusion layer. Part I. Experimental.” *J. Power Sources*, 171(1), 26–36.

Norouzifard, V., and Bahrami, M. (2014a). “Deformation of PEM fuel cell gas diffusion layers under compressive loading: An analytical approach.” *J. Power Sources*, 264, 92–99.

Norouzifard, V., and Bahrami, M. (2014b). “Analytical Modeling of PEM Fuel Cell Gas Diffusion Layers Deformation under Compression: Part 1 - Linear Behaviour Region.” *ECS Trans.*, 61(11), 1–12.

O’Hayre, R., Cha, S.-W., Colella, W. G., and Prinz, F. B. (2016). *Fuel cell fundamentals*.

Omrani, R., and Shabani, B. (2019). “Gas diffusion layers in fuel cells and electrolysers: A novel semi-empirical model to predict electrical conductivity of sintered metal fibres.” *Energies*, 12(5), 1–17.

Ouaidat, G., Cherouat, A., Kouta, R., and Chamoret, D. (2020). “Numerical modeling of the mechanical behavior of proton exchange membrane fuel cell performance: Design of experiment study and optimization.” *Int. J. Hydrogen Energy*, 45(46), 25210–25226.

Oualid, S. El, Lachat, R., Candusso, D., and Meyer, Y. (2017). “Characterization process to measure the electrical contact resistance of Gas Diffusion Layers under mechanical static compressive loads.” *Int. J. Hydrogen Energy*, 42(37), 23920–23931.

Ozden, A., Shahgaldi, S., Li, X., and Hamdullahpur, F. (2019). “A review of gas diffusion layers for proton exchange membrane fuel cells—With a focus on characteristics, characterization techniques, materials and designs.” *Prog. Energy Combust. Sci.*, 74, 50–102.

Ozgur, K. (2009). “Compression apparatus for fuel cell stack.”

Padavu, P., Koorata, P. K., and Bhat, S. D. (2021). “Numerical investigation on the improved reactant mass transport with depth-dependent flow fields in polymer electrolyte fuel cell under inhomogeneous gas diffusion layer compression.” *Int. J. Heat Mass Transf.*, 180, 121796.

Patel, V., Battrell, L., Anderson, R., Zhu, N., and Zhang, L. (2019). “Investigating effect of different gas diffusion layers on water droplet characteristics for proton exchange membrane (PEM) fuel cells.” *Int. J. Hydrogen Energy*, 44(33), 18340–18350.

Patermarakis, G., and Papandreadis, N. (1993). “Effect of the structure of porous anodic Al2O3 films on the mechanism of their hydration and pore closure during hydrothermal treatment.” *Electrochim. Acta*, 38(10), 1413–1420.

Peng, L., Qiu, D., Yi, P., and Lai, X. (2016). “An analytical model for contact pressure prediction considering dimensional error of stamped bipolar plate and gas diffusion layer in proton exchange membrane fuel cell stack assembly.” *J. Electrochem. Energy Convers. Storage*, 13(2), 1–10.

Poornesh, K. K., and Cho, C. (2015). “Stability of polymer electrolyte membranes in fuel cells: Initial attempts to bridge physical and chemical degradation modes.” *Fuel Cells*, 15(1), 196–203.

Poornesh, K. K., Cho, C. D., Lee, G. B., and Tak, Y. S. (2010a). “Gradation of mechanical properties in gas-diffusion electrode. Part 2: Heterogeneous carbon fiber and damage evolution in cell layers.” *J. Power Sources*, 195(9), 2718–2730.

Poornesh, K. K., Cho, C. D., Lee, G. B., and Tak, Y. S. (2010b). “Gradation of mechanical properties in gas diffusion electrode. Part 1: Influence of nano-scale heterogeneity in catalyst layer on interfacial strength between catalyst layer and membrane.” *J. Power Sources*, 195(9), 2709–2717.

Poornesh, K. K., Cho, C., Kim, D. Y., and Tak, Y. (2010c). “Effect of gas-diffusion electrode material heterogeneity on the structural integrity of polymer electrolyte fuel cell.” *Energy*, 35(12), 5241–5249.

Poornesh, K. K., Lee, S. K., Cho, C., and Choi, K. W. (2010d). “Effect of bipolar plate materials on the stress distribution and interfacial contact resistance in PEM fuel cell.” *Int. J. Precis. Eng. Manuf.*, 11(4), 583–588.

“Powering up fuel cells.” (n.d.). <https://www.fuelcellstore.com/spec-sheets/sigracet-22-28-36-39-properties-sheet.pdf> (Sep. 22, 2022).

Qiu, D., Janßen, H., Peng, L., Irmscher, P., Lai, X., and Lehnert, W. (2018). “Electrical resistance and microstructure of typical gas diffusion layers for proton exchange membrane fuel cell under compression.” *Appl. Energy*, 231(January), 127–137.

Qiu, D., Peng, L., Yi, P., and Lai, X. (2017). “A micro contact model for electrical contact resistance prediction between roughness surface and carbon fiber paper.” *Int. J. Mech. Sci.*, 124–125(January), 37–47.

Qiu, D., Yi, P., Peng, L., and Lai, X. (2015). “Assembly design of proton exchange membrane fuel cell stack with stamped metallic bipolar plates.” *Int. J. Hydrogen Energy*, 40(35), 11559–11568.

Qiu, Y., Wu, P., Miao, T., Liang, J., Jiao, K., Li, T., Lin, J., and Zhang, J. (2020). “An intelligent approach for contact pressure optimization of PEM fuel cell gas diffusion layers.” *Appl. Sci.*, 10(12).

Radhakrishnan, V., and Haridoss, P. (2010). “Effect of cyclic compression on structure and properties of a Gas Diffusion Layer used in PEM fuel cells.” *Int. J. Hydrogen Energy*, 35(20), 11107–11118.

Radhakrishnan, V., and Haridoss, P. (2011). “Differences in structure and property of carbon paper and carbon cloth diffusion media and their impact on proton exchange membrane fuel cell flow field design." *Mater. Des.*

Rofaiel, A., Ellis, J. S., Challa, P. R., and Bazylak, A. (2012). "Heterogeneous through-plane distributions of polytetrafluoroethylene in polymer electrolyte membrane fuel cell gas diffusion layers." *J. Power Sources*, 201, 219–225.

Roy Chowdhury, P., Vikram, A., Phillips, R. K., and Hoorfar, M. (2016). "Measurement of effective bulk and contact resistance of gas diffusion layer under inhomogeneous compression - Part II: Thermal conductivity." *J. Power Sources*, 320, 222–230.

Sadeghi, E., Djilali, N., and Bahrami, M. (2010). "Effective thermal conductivity and thermal contact resistance of gas diffusion layers in proton exchange membrane fuel cells. Part 2: Hysteresis effect under cyclic compressive load." *J. Power Sources*, 195(24), 8104–8109.

Shahgaldi, S., Alaefour, I., and Li, X. (2018a). "Impact of manufacturing processes on proton exchange membrane fuel cell performance." *Appl. Energy*, 225, 1022–1032.

Shahgaldi, S., Ozden, A., Li, X., and Hamdullahpur, F. (2018b). "Cathode catalyst layer design with gradients of ionomer distribution for proton exchange membrane fuel cells." *Energy Convers. Manag.*, 171(June), 1476–1486.

Shimpalee, S., Lilavivat, V., Zee, J. W. Van, McCrabb, H., and Lozano-Morales, A. (2011). "Understanding the effect of channel tolerances on performance of PEMFCs." *Int. J. Hydrogen Energy*, 36(19), 12512–12523.

Shinde, U., and Koorata, P. K. (2021). "Numerical investigation on the sensitivity of endplate design and gas diffusion material models in quantifying localized interface and bulk electrical resistance." *Int. J. Hydrogen Energy*, 46(33), 17358–17373.

Silberstein, M. N., and Boyce, M. C. (2010). "Constitutive modeling of the rate, temperature, and hydration dependent deformation response of Nafion to monotonic and cyclic loading." *J. Power Sources*, 195(17), 5692–5706.

Silberstein, M. N., and Boyce, M. C. (2011). "Hygro-thermal mechanical behavior of

Nafion during constrained swelling." *J. Power Sources*, 196(7), 3452–3460.

Sinha, P. K., Mukherjee, P. P., and Wang, C. Y. (2007). "Impact of GDL structure and wettability on water management in polymer electrolyte fuel cells." *J. Mater. Chem.*, 17(30), 3089–3103.

Slobodian, P., Riha, P., Lengalova, A., and Saha, P. (2011). "Compressive stress-electrical conductivity characteristics of multiwall carbon nanotube networks." *J. Mater. Sci.*, 46(9), 3186–3190.

Slobodian, P., Riha, P., Olejnik, R., and Saha, P. (2013). "Deformation theory of an electro-conductive composite composed of entangled network of carbon nanotubes embedded in elastic polyurethane." *AIP Conf. Proc.*, 1526, 268–277.

Solasi, R., Zou, Y., Huang, X., Reifsnider, K., and Condit, D. (2007). "On mechanical behavior and in-plane modeling of constrained PEM fuel cell membranes subjected to hydration and temperature cycles." *J. Power Sources*, 167(2), 366–377.

Sow, P. K., Prass, S., Kalisvaart, P., and Mérida, W. (2015). "Deconvolution of electrical contact and bulk resistance of gas diffusion layers for fuel cell applications." *Int. J. Hydrogen Energy*, 40(6), 2850–2861.

Su, A., Chiu, Y. C., and Weng, F. B. (2005). "The impact of flow field pattern on concentration and performance in PEMFC." *Int. J. Energy Res.*, 29(5), 409–425.

Su, Z. Y., Liu, C. T., Chang, H. P., Li, C. H., Huang, K. J., and Sui, P. C. (2008). "A numerical investigation of the effects of compression force on PEM fuel cell performance." *J. Power Sources*, 183(1), 182–192.

Suvorov, A. P., Elter, J., Staudt, R., Hamm, R., Tudryn, G. J., Schadler, L., and Eisman, G. (2008). "Stress relaxation of PBI based membrane electrode assemblies." *Int. J. Solids Struct.*, 45(24), 5987–6000.

Tanaka, S., Bradfield, W. W., Legrand, C., and Malan, A. G. (2016). "Numerical and experimental study of the effects of the electrical resistance and diffusivity under clamping pressure on the performance of a metallic gas-diffusion layer in polymer electrolyte fuel cells." *J. Power Sources*, 330, 273–284.

Taymaz, I., and Benli, M. (2010). “Numerical study of assembly pressure effect on the performance of proton exchange membrane fuel cell.” *Energy*, 35(5), 2134–2140.

Thompson, G. . (1997). “Porous anodic alumina: fabrication, characterization and applications.” *Thin Solid Films*, 297(1–2), 192–201.

Todd, D., Bennett, S., and Mérida, W. (2016). “Anisotropic electrical resistance of proton exchange membrane fuel cell transport layers as a function of cyclic strain.” *Int. J. Hydrogen Energy*, 41(14), 6029–6035.

“Toray Carbon Paper TGP-H-060 |.” (n.d.). <https://www.fuelcellearth.com/fuel-cell-products/toray-paper-060/> (Sep. 22, 2022).

Tsushima, S., and Hirai, S. (2011). “In situ diagnostics for water transport in proton exchange membrane fuel cells.” *Prog. Energy Combust. Sci.*, 37(2), 204–220.

Uzundurukan, A., Bilgili, M., and Devrim, Y. (2020). “Examination of compression effects on PEMFC performance by numerical and experimental analyses.” *Int. J. Hydrogen Energy*, 45(60), 35085–35096.

Vikram, A., Chowdhury, P. R., Phillips, R. K., and Hoorfar, M. (2016). “Measurement of effective bulk and contact resistance of gas diffusion layer under inhomogeneous compression - Part I: Electrical conductivity.” *J. Power Sources*, 320, 274–285.

Wang, J., Yuan, J., and Sundén, B. (2016). “Modeling of inhomogeneous compression effects of porous GDL on transport phenomena and performance in PEM fuel cells.” *Int. J. Energy Res.*

Wang, J., Yuan, J., and Sundén, B. (2017a). “On electric resistance effects of non-homogeneous GDL deformation in a PEM fuel cell.” *Int. J. Hydrogen Energy*, 42(47), 28537–28548.

Wang, J., Yuan, J., Yu, J.-S., and Sundén, B. (2017b). “Investigation of effects of non-homogenous deformation of gas diffusion layer in a PEM fuel cell.” *Int. J. Energy Res.*, 41(14), 2121–2137.

Wang, X., Song, Y., and Zhang, B. (2008). “Experimental study on clamping pressure distribution in PEM fuel cells.” *J. Power Sources*, 179(1), 305–309.

Wang, Y., and Chen, K. S. (2011). “Effect of Spatially-Varying GDL Properties and Land Compression on Water Distribution in PEM Fuel Cells.” 158(11), 1292–1299.

Wang, Y., Chen, K. S., Mishler, J., Cho, S. C., and Adroher, X. C. (2011). “A review of polymer electrolyte membrane fuel cells: Technology, applications, and needs on fundamental research.” *Appl. Energy*, 88(4), 981–1007.

Wen, C.-Y., Lin, Y.-S., and Lu, C.-H. (2009). “Experimental study of clamping effects on the performances of a single proton exchange membrane fuel cell and a 10-cell stack.” *J. Power Sources*, 192(2), 475–485.

Wilkinson, D., and Vanderleeden, O. (2010). *Handbook of Fuel Cells - Fundamentals, Technology, and Application*.

Wozniczka, B., Fletcher, N. J., and Gibb, P. R. (1999). “Electrochemical fuel cell stack with compression bands.”

Xia, Z., Chen, H., Zhang, T., and Pei, P. (2022). “Effect of channel-rib width ratio and relative humidity on performance of a single serpentine PEMFC based on electrochemical impedance spectroscopy.” *Int. J. Hydrogen Energy*, 47(26), 13076–13086.

Xiao, L., Luo, M., Zhang, H., Zeis, R., and Sui, P.-C. (2019). “Solid Mechanics Simulation of Reconstructed Gas Diffusion Layers for PEMFCs.” *J. Electrochem. Soc.*, 166(6), F377–F385.

Xiao, Y., Gao, Z., Gao, F., Zhang, T., Zhang, W., Li, Z., Ma, X., and Qi, J. (2020). “Improved analytical modeling and mechanical characterization of gas diffusion layers under compression load.” *Energy Sci. Eng.*, 8(8), 2799–2807.

Xing, L., Cai, Q., Xu, C., Liu, C., Scott, K., and Yan, Y. (2016). “Numerical study of the effect of relative humidity and stoichiometric flow ratio on PEM (proton exchange membrane) fuel cell performance with various channel lengths: An anode partial flooding modelling.” *Energy*, 106, 631–645.

Yan, X., Lin, C., Zheng, Z., Chen, J., Wei, G., and Zhang, J. (2020). “Effect of clamping pressure on liquid-cooled PEMFC stack performance considering inhomogeneous gas diffusion layer compression." *Appl. Energy*, 258, 114073.

Yarar Kaplan, B., Is, L., and Alkan Gü rsel, S. (n.d.). "Flexible carbon-cellulose fiber-based composite gas diffusion layer for polymer electrolyte membrane fuel cells."

Ye, D., Gauthier, E., Benziger, J. B., and Pan, M. (2014). "Bulk and contact resistances of gas diffusion layers in proton exchange membrane fuel cells." *J. Power Sources*, 256, 449–456.

Yim, S. D., Kim, B. J., Sohn, Y. J., Yoon, Y. G., Park, G. G., Lee, W. Y., Kim, C. S., and Kim, Y. C. (2010). "The influence of stack clamping pressure on the performance of PEM fuel cell stack." *Curr. Appl. Phys.*, 10(2 SUPPL.), 2009–2011.

Yinqi Shen. (2017). "Mechanical Degradation of Membrane Electrode Assemblies in Proton Exchange Membrane Fuel Cells." Waterloo University, Ontario, Canada.

Yu, H. N., Kim, S. S., Suh, J. Do, and Lee, D. G. (2010). "Axiomatic design of the sandwich composite endplate for PEMFC in fuel cell vehicles." *Compos. Struct.*, 92(6), 1504–1511.

Zamel, N., Li, X., and Shen, J. (2012). "Numerical estimation of the effective electrical conductivity in carbon paper diffusion media." *Appl. Energy*, 93, 39–44.

Zamel, N., Litovsky, E., Shakhshir, S., Li, X., and Kleiman, J. (2011). "Measurement of in-plane thermal conductivity of carbon paper diffusion media in the temperature range of -20°C to +120°C." *Appl. Energy*.

Zhang, J., Tang, Y., Song, C., Xia, Z., Li, H., Wang, H., and Zhang, J. (2008). "PEM fuel cell relative humidity (RH) and its effect on performance at high temperatures." *Electrochim. Acta*, 53(16), 5315–5321.

Zhang, J., Zhang, H., Wu, J., and Zhang, J. (2013). *PEM Fuel Cell Testing and Diagnosis*.

Zhang, L., Liu, Y., Song, H., Wang, S., Zhou, Y., and Hu, S. J. (2006). "Estimation of contact resistance in proton exchange membrane fuel cells." *J. Power Sources*, 162(2), 1165–1171.

Zhang, X., Yang, J., Ma, X., Zhuge, W., and Shuai, S. (2022a). "Modelling and analysis on effects of penetration of microporous layer into gas diffusion layer in PEM fuel cells: Focusing on mass transport." *Energy*, 254, 124103.

Zhang, Y., Tao, Y., Ren, H., Wu, M., Li, G., Wan, Z., and Shao, J. (2022b). "A metallic gas diffusion layer and porous media flow field for proton exchange membrane fuel cells." *J. Power Sources*, 543, 231847.

Zhang, Z., He, P., Dai, Y. J., Jin, P. H., and Tao, W. Q. (2020). "Study of the mechanical behavior of paper-type GDL in PEMFC based on microstructure morphology." *Int. J. Hydrogen Energy*, (xxxx).

Zhao, J., Ozden, A., Shahgaldi, S., Alaefour, I. E., Li, X., and Hamdullahpur, F. (2018). "Effect of Pt loading and catalyst type on the pore structure of porous electrodes in polymer electrolyte membrane (PEM) fuel cells." *Energy*, 150, 69–76.

Zhou, P., Lin, P., Wu, C. W., and Li, Z. (2011). "Effect of nonuniformity of the contact pressure distribution on the electrical contact resistance in proton exchange membrane fuel cells." *Int. J. Hydrogen Energy*, 36(10), 6039–6044.

Zhou, P., and Wu, C. W. (2007). "Numerical study on the compression effect of gas diffusion layer on PEMFC performance." *J. Power Sources*, 170(1), 93–100.

Zhou, P., Wu, C. W., and Ma, G. J. (2006). "Contact resistance prediction and structure optimization of bipolar plates." *J. Power Sources*, 159(2), 1115–1122.

Zhou, Y., Lin, G., Shih, A. J., and Hu, S. J. (2009). "Assembly pressure and membrane swelling in PEM fuel cells." *J. Power Sources*.

Zhou, Z., Qiu, D., Zhai, S., Peng, L., and Lai, X. (2020). "Investigation of the assembly for high-power proton exchange membrane fuel cell stacks through an efficient equivalent model." *Appl. Energy*, 277(June), 115532.

PUBLICATIONS

International Journals

1. **Umesh Shinde,** Poornesh Kumar Koorata, Pranav Padavu (2022). “Electrical/flow heterogeneity of gas diffusion layer and inlet humidity induced performance variation in polymer electrolyte fuel cells.” International Journal of Hydrogen Energy, 48 (34), 12877-12892 **(IF: 7.139)**
2. **Umesh Shinde,** Poornesh Kumar Koorata (2022). "A phase-dependent constitutive model to predict cyclic electrical conductivity in fuel cell gas diffusion media." Journal of Power Sources, 527, 231179 **(IF: 9.794)**
3. **Umesh Shinde,** Poornesh Kumar Koorata (2021). "Numerical investigation on the sensitivity of endplate design and gas diffusion material models in quantifying localized interface and bulk electrical resistance." International Journal of Hydrogen Energy, 46 (33), 17358-17373 **(IF: 7.139)**

International/National Conferences

1. **Umesh Shinde**, Pranav Padavu, Poornesh Kumar Koorata (2022). "Numerical investigation on the effects of inhomogeneous gas diffusion layer and impact of interfacial contact resistance on performance of polymer electrolyte fuel cells." 23rd World Hydrogen Energy Conference, Istanbul Congress Center, Istanbul, Turkey.
2. **Umesh Shinde**, Pranav Padavu, Poornesh Kumar Koorata (2022). "Influence of inlet humidity, interfacial contact resistance and gas diffusion layer inhomogeneity on the performance of PEMFC." 20th ISME Conference on Advances in Mechanical Engineering, IIT Ropar, Punjab
3. **Umesh Shinde,** Poornesh Kumar Koorata (2021). "Influence of clamping configurations on contact pressure and bulk permeability distribution in fuel cell gas diffusion layer." International Online Conference on Energy Sciences (ICES 2021), MGU University, Kerala.

BIODATA

Name:	Umesh Shinde
Date of Birth:	25/10/1991
Mobile:	+91 89719 49434
Email:	umeshrshinde@yahoo.com
Address:	H.No. 1824 Pl.No. 9 (66/4), Shivaji Road, Ganeshpur, Belgaum, Karnataka, India – 591108

Qualification:

Degree	University/Institute	Subject	Year	Performance
Ph.D	National Institute of Technology Karnataka, Surathkal	Fuel Cells, Design Engineering	2018 to present	9.0 CGPA (course work)
M.Tech	K.L.E College of Engineering and Technology, Belgaum, Karnataka	Design Engineering	2014 - 2016	75.67%
B.E	Maratha Mandal Engineering College, Belgaum, Karnataka	Mechanical Engineering	2010 - 2014	65.35%

Work Experience:

Post	Name of the Institute	Duration
Lecturer	Motichand Lengade Bharatesh Polytechnic, Belgaum, Karnataka	July, 2017- June, 2018

UMESH SHINDE